Probing Primordial Magnetic Fields with the Cosmic Microwave Background

by

Yun Li

M.Sc., The University of Manchester, 2011
B.Sc., Lanzhou University, 2010

Thesis Submitted in Partial Fulfillment of the
Requirements for the Degree of
Doctor of Philosophy

in the
Department of Physics
Faculty of Science

SIMON FRASER UNIVERSITY
Spring 2020

Approval

Name:	**Yun Li**
Degree:	**Doctor of Philosophy (Physics)**
Title:	**Probing Primordial Magnetic Fields with the Cosmic Microwave Background**
Examining Committee:	**Chair:** Malcolm Kennett Associate Professor
	Levon Pogosian Senior Supervisor Professor
	Andrei Frolov Supervisor Associate Professor
	Howard Trottier Supervisor Professor
	Bernd Stelzer Internal Examiner Associate Professor
	Francesc Ferrer External Examiner Associate Professor Department of Physics Washington University in St. Louis
Date Defended:	**January 21, 2020**

Abstract

A primordial magnetic field (PMF) present before recombination can leave specific signatures in the cosmic microwave background (CMB) fluctuations. Of particular importance is its contribution to the B-mode polarization power spectrum. Indeed, vortical modes sourced by the PMF can dominate the B-mode power spectrum on small scales, as they survive damping up to a small fraction of the Silk length. Therefore, measurements of the B-mode polarization at high-ℓ, such as the one recently performed by the South Pole Telescope (SPT), have the potential to provide stringent constraints on the PMF. We use the publicly released SPT B-mode polarization spectrum (2015 and 2019), along with the temperature and polarization data from the Planck satellite, to derive constraints on the magnitude $B_{1\,\mathrm{Mpc}}$, the spectral index n_B and the energy scale at which the PMF was generated. We find that after marginalizing n_B, Planck data constrains the magnetic amplitude to $B_{1\,\mathrm{Mpc}} < 3.3$ nG at 95% confidence level (CL), the SPT measurement improves the constraint to $B_{1\,\mathrm{Mpc}} < 1.5$ nG. The magnetic spectral index, n_B, and the time of the generation of the PMF are unconstrained. For a nearly scale-invariant PMF, predicted by the simplest inflationary magnetogenesis models, the bound from Planck+SPT is $B_{1\,\mathrm{Mpc}} < 1.2$ nG at 95% CL for a non-helical PMF and $B_{1\,\mathrm{Mpc}} < 1.1$ nG for a maximally helical PMF. The bound from Planck data alone is $B_{1\,\mathrm{Mpc}} < 1.7$ nG at 95% CL when considering a maximally helical field. For a non-helical PMF with a spectral index of $n_B = 2$, expected for fields generated in post-inflationary phase transitions, the 95% CL bound is $B_{1\,\mathrm{Mpc}} < 0.002$ nG, corresponding to the magnetic fraction of the radiation density $\Omega_{B\gamma} < 10^{-3}$ or the effective field $B_{\mathrm{eff}} < 100$ nG. We find that accounting for the helicity weakens the CMB constraints on PMF, allowing to have more magnetic power available on the 1Mpc comoving scale relevant to the formation of galactic magnetic fields. The patches for the Boltzmann code CAMB and the Markov Chain Monte Carlo engine CosmoMC, incorporating the PMF effects on CMB, are made publicly available.

Keywords: Primordial Magnetic Fields; Cosmic Microwave Background; Helicity.

Acknowledgements

I would like to acknowledge the support provided by my family, my mother, Yin Chundi, my father, Li Jinhua. Especially for my mother, she gave me strength although she suffered a lot from disease; I would like to express my sincere gratitude to Professor Levon Pogosian, Professor Andrei Frolov, and Professor Howard Trottier, my research supervisors, for their patient guidance, enthusiastic encouragement, and useful critiques of this research work. I would also like to thank my colleague Dr. Alex Zucca, who helped me a lot in finalizing this project and kept my progress on schedule, and thank you for his help in doing data analysis. I am grateful to Richard Shaw for sharing with us the updated version of his magnetic CAMB patch. We benefited from communications and discussion with Camille Bonvin, Fabio Finelli, Alireza Hojjati, Antony Lewis, Tina Kahniashvili, Daniela Paoletti, Richard Shaw and Tanmay Vachaspati. My grateful thanks are also extended to the staff of the physics department for their help throughout my study at SFU. Finally, I wish to thank my senior supervisor Professor Levon Pogosian again, who gave me the golden opportunity to do this wonderful project. Levon helped me a lot in doing research and reading early drafts to provide me with advice so I could edit.

Table of Contents

List of Tables

List of Figures

Chapter 1

Introduction

According to the widely accepted model, the universe experienced a period of inflation, or accelerated expansion, during which quantum fluctuations of the metric were stretched beyond the horizon and resulted in the primordial density fluctuations that later seeded the structures we see around us today. After the inflationary epoch, the universe went through a period of radiation domination. When the temperature dropped to around $0.3\,eV$, protons and electrons started to combine to form hydrogen atoms. This process is called recombination or decoupling epoch. Prior to decoupling, photons are tightly coupled to protons and electrons through Coulomb scattering, making the plasma opaque to electromagnetic radiation. After the decoupling, photons begin to free stream and persist until the present epoch in the form of the cosmic microwave background radiation (CMBR). The fact that the CMBR is measured to have a nearly perfect black body spectrum [2, 3] provides strong evidence for the standard cosmology model.

The CMBR is nearly isotropic, with an averaged temperature of 2.725 K, with anisotropies of the order $\mathcal{O}(10^{-5})$ K first detected by the COBE-DMR experiment in 1992 [4]. Studying the anisotropies in the CMBR intensity and polarization can help us to study the initial conditions for the universe, including the primordial fluctuations set by inflation and other potential contributions, such as the primordial magnetic fields that are the subject of this thesis. In addition to the primary CMBR anisotropy generated when the photons last interacted with the matter at the time of recombination, secondary anisotropies are produced as the photons travel to us. This includes the gravitational lensing by the gravitational potentials [5] along the line of sight. The CMB anisotropy also generates a polarized component, which can be decomposed into even parity (E-mode) and odd parity (B-mode) polarization. Density perturbations at the last scattering surface generate temperature anisotropies and E-mode polarization. However, primordial B-mode polarization can only be produced by parity-odd sources, such as gravitational waves or primordial magnetic fields. After recombination, gravitational lensing produces a secondary B-mode by converting some of the E-mode polarization into B-modes. The precision measurements of the CMB B-mode pro-

vides a window into parity-violating physics and, as this thesis shows, can help to constrain the primordial magnetic field.

1.1 Cosmic magnetic fields

Multiple observations have confirmed the existence of magnetic fields in the universe over a broad range of scales. Micro-Gauss (μG) strength coherent magnetic fields exist in all types of galaxies, including the Milky Way, and in galaxy clusters and superclusters [6, 7, 8, 9]. Moreover, strong magnetic fields are seen in normal galaxies [10] at higher redshifts, close to $z \approx 1.3$, which indicates that the galactic fields were generated early. Such observations of magnetic fields in intermediate and high redshift galaxies imply that the time spent by the galactic dynamo to develop a coherent B-field is relatively short, landing support to the idea that primordial magnetic fields existed before recombination. The initial seeds would be amplified by structure formation, adiabatic compression, or magnetohydrodynamic (MHD) turbulent dynamo instabilities [11, 12, 13]. In order for a successful operation by the galactic dynamo, the initial seed fields need to have an appropriate coherence scale and strength [13]. The (comoving) coherence length of the initial B-field must be greater than 10 Kpc. With different efficiencies of the dynamo amplification, the strength of the required B-field seed varies between 10^{-12}G and 10^{-22} G.

Observations show that magnetic fields are common at high redshifts, which favors the idea that the initial seed fields were generated at early times. There is also evidence of magnetic fields being present even on truly cosmological scales[14, 15]. A lower limit 10^{-18}-10^{-15} Gauss on the strength of the intergalactic field, based on cosmic ray data, was reported in [14, 16, 17]. The evidence and the possible origin of the large scale magnetic field is still debated. A possible explanation is that of a primordial magnetic field (PMF).

There are various mechanisms of early magnetogenesis with their advantages and shortcomings. Existing proposals include both classical and quantum scenarios[13, 18, 19] within as well as outside the standard model. The PMF could have been be generated during inflation[20, 21, 22] or during phase transitions, such as the electroweak or quantum chromodynamics (QCD) phase transitions, in which case the magnetic field would likely be helical [23, 24, 25, 26, 27, 28, 29].

1.2 An overview of CMB bounds on primordial magnetic fields

Cosmological magnetic fields would leave imprints in CMB temperature and polarization. Therefore, the CMB is an invaluable source of information for investigating and constraining the physical properties of PMFs, helping us answer questions about their origin. The anisotropic stress of the magnetic field can source all types of cosmological perturbations

(scalar, vector, and tensor perturbations), which have some noticeable differences when comparing them with the primary perturbations. For example, the PMF induces vector (vorticity) perturbations sourced by the Lorentz force, which are not expected in the standard model [30]. The impact of the PMF on the CMB temperature power spectrum is mostly evident on small angular scales, where the primary CMB is suppressed by Silk damping[21]. Thus, the high-resolution CMB data helps to constrain the PMF.

The PMF is expected to be helical if produced in phase transitions or via parity-violating processes[23, 26]. The helicity of a magnetic field is a measure of twist and linkage of magnetic field lines. A helical PMF can lead to parity-violating correlations in CMB, such as TB and EB, which are predicted to vanish in the standard model. The current bounds on TB and EB are very weak, although future CMB polarization experiments will produce much better constraints. Fortunately, helical PMFs also affect the parity even CMB spectra, measured by current experiments, such as Planck and SPT.

Multiple groups have studied the impact of PMFs on the CMB and derived constraints from the data. The Planck team derived constraints on the amplitude and the spectral index of the PMF using their 2015 data [31]. They found that the magnetic field strength smoothed over 1 Mpc is constrained to be $B_{1\mathrm{Mpc}} < 4.4$ nG at the 95% confidence level (CL), with the bound being stronger if assuming a particular PMF spectrum. The combination of the 7-year WMAP data[32] and the high ℓ temperature anisotropy spectrum from the South Pole Telescope (SPT)[33] put a bound on the magnetic field, $B_{1\mathrm{Mpc}} < 3.5$ nG at the 95% confidence level (CL)[34]. The Polarbear collaboration[35] with their measurement of the B-mode polarization spectrum has a comparable bound of $B_{1\mathrm{Mpc}} < 3.9$ nG.

1.3 The overview of the thesis

In this thesis I present a detailed analysis of the PMF contributions to the CMB power spectra, including the effects of magnetic helicity on the scalar, vector, and tensor modes. I use the currently available CMB data from Planck and SPT to constrain the amplitude and the spectral shape of the PMF. Some parts of this thesis are based on my work published in [35, 36]. The organization of this thesis is as follows. In Chapter 2, I review the basic properties of magnetic fields in the expanding universe. In Chapter. 3, I review the theory of cosmological perturbations relevant for the calculation of the CMB spectra. In Chapter. 4, I present the widely used model of the PMF, and present a calculation of the cosmological perturbations sourced by the PMF stress-energy. I also develop all the steps required for calculating the CMB temperature and polarization spectra. I consider both non-helical and helical PMF and derive the full set of equations for the scalar, vector, and tensor modes. In Chapter 5, I present my numerical calculation of the PMF sourced CMB power spectra for both helical and non-helical PMFs. In Chapter 6, I derive constraints on non-helical PMFs from a combination of Planck and the 2015 SPT data. In Chapter 7, I use Planck and

the 2019 SPT data to derive constraints on the non-helical and maximally helical PMFs. Finally, I conclude with a summary and discussion in Chapter 8. In addition, some of the mathematical tools and the detailed calculations are presented in the Appendix A.

We employ natural units ($\hbar = c = k_B = 1$). Greek indices, such as $\alpha, \beta, \mu, \nu...$ run from 0 to 3. Latin indices, such as $a, b, i, j...$ run from 1 to 3. Spatial 3 dimensional vectors are written in either $\vec{v}$ or $\mathbf{v}$, or $\hat{v}$, and $\hat{v}$ means unit vector.

Chapter 2

Magnetic fields in the expanding universe

2.1 The Expanding Universe

On large scales, our universe appears to be isotropic (no preferred direction) and homogeneous (the same everywhere). There is also overwhelming evidence that the universe is expanding. Distant galaxies are moving away from each other and we can introduce the scale factor a as a quantity that is proportional to the increasing distance between them. It is conventional to take $a = 1$ at present and we assume a flat universe, in which case it is related to the redshift (z) as

$$1 + z \equiv \frac{\lambda_{obs}}{\lambda_{emit}} = \frac{1}{a}, \tag{2.1}$$

where λ_{obs} is the observed wavelength that is larger than the emitted wavelength λ_{emit} due to the expansion of the Universe.

Because of the cosmic expansion, it is useful to measure cosmological distances in comoving coordinates. The comoving distance that light travels during time t is

$$\eta = \int_0^t \frac{dt'}{a(t')}, \tag{2.2}$$

where η is referred to as the conformal time. The longest distance the light can travel to us is from $t = 0$ (at the Big Bang) until today, and that distance, η_0, is the comoving horizon, equal to the conformal time today. The comoving distance between us and a distant object at a scale factor a is

$$\chi(a) = \int_{t(a)}^{t_0} \frac{dt'}{a(t')} = \int_a^1 \frac{da'}{a'^2 H(a')}, \tag{2.3}$$

where the Hubble rate is used to measure how fast the scale factor changes $H(t) \equiv \frac{da/dt}{a}$. The present value of the Hubble parameter is often quantified in terms of h, defined as

$$H_0 = 100\,\mathrm{h\,km\,s^{-1}Mpc^{-1}} = \frac{h}{0.98 \times 10^{10}\mathrm{years}}, \tag{2.4}$$

where 1Mpc $= 3.0856 \times 10^{22}$ m is the commonly used astronomical length scale of a megaparsec and h is measured to be ≈ 0.7.

The Friedmann equation describes the evolution of the scale factor

$$\begin{aligned} H^2(t) &= \frac{8\pi G}{3}\rho(t) - \frac{K}{a^2(t)}, \\ 1 &= \frac{8\pi G}{3H^2(t)}\rho(t) - \frac{K}{a^2(t)H^2(t)}, \end{aligned} \tag{2.5}$$

where $\rho(t)$ is the sum of energy densities of all components of the universe, '0' denotes the present value, $\rho_{cr} \equiv \frac{3H^2}{8\pi G}$ is the critical density and G is the Newton's constant. We can define the fractional energy density for the species i as

$$\Omega_i(a) \equiv \frac{\rho_i(a)}{\rho_{cr}(a)}, \tag{2.6}$$

to write the Friedmann equation as

$$\sum_i \Omega_i(a) + \Omega_K(a) = 1, \tag{2.7}$$

where $\Omega_K = -K/(aH)^2$ is the curvature parameter. $K = 8\pi G(\rho_0 - \rho_{cr0})/3a_0$. For a spatially flat universe, the density of the universe is exactly equal to the critical density and $K = 0$, $\Omega_K = 0$. The density of non-relativistic matter scales as a^{-3}, while that of radiation scales as a^{-4}. The total density of the universe at scale factor a can be written as

$$\rho = \rho_\Lambda + \frac{\rho_{m0}}{a^3} + \frac{\rho_{r0}}{a^4} = \rho_{cr0}(\Omega_\Lambda + \frac{\Omega_{m0}}{a^3} + \frac{\Omega_{r0}}{a^4}), \tag{2.8}$$

where ρ_Λ is the constant vacuum energy density responsible for the observed acceleration of the cosmic expansion. Since the current data is consistent with a spatially flat universe, we will assume $\Omega_K = 0$ in our analysis.

2.2 The Thermal History of the Early Universe

Below we will briefly describe the most remarkable events in the history of the universe:

Inflation. Universe underwent a period of exponentially fast expansion at about 10^{-35} seconds old. Inflation solves the horizon problem and the flatness problem, and provides the primordial seeds for structure formation.

Electroweak phase transition. At $T \sim 100$ GeV, $z \sim 10^{15}$, the electroweak $SU(2)$ symmetry was spontaneously broken and elementary particles (quarks, leptons and gauge

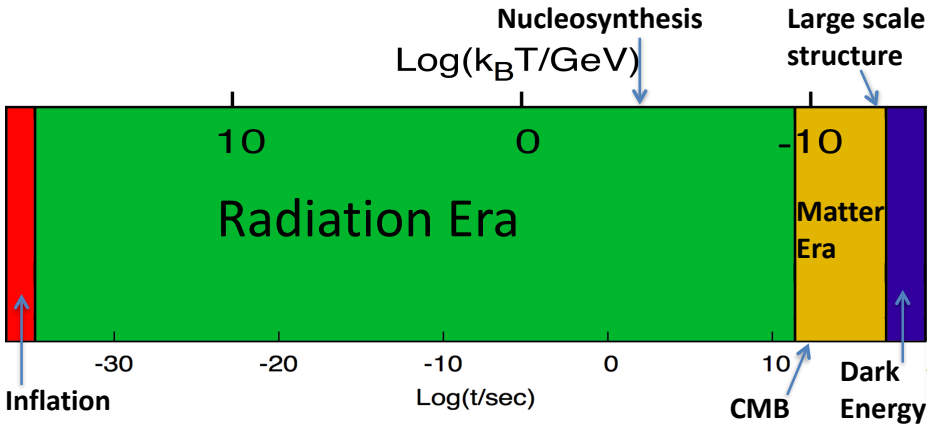

Figure 2.1: The Thermal History of the Universe

bosons) received their masses via the Higgs mechanism.

QCD phase transition. When temperature cools below 150 MeV ($z \sim 10^{12}$), the quantum chromodynamics (QCD) phase transition took place in which the chiral symmetry was broken and quarks were confined into hadrons due to the strong interactions between the quarks and the gluons.

Neutrino decoupling. Neutrinos are kept in thermal equilibrium at early times by interacting with the rest of the primordial plasma through the weak interactions:

$$\begin{aligned} \nu_e + \bar{\nu_e} &\leftrightarrow e^+ + e^- \\ e^- + \bar{\nu_e} &\leftrightarrow e^- + \bar{\nu_e}. \end{aligned} \tag{2.9}$$

Neutrino decoupling happened at $T \sim 1$ MeV, $z \sim 6 \times 10^9$, when weak interaction rates become negligible.

Electron – positron annihilation. Electrons and positrons annihilate shortly after neutrino decoupling ($T \sim 500$ KeV, $z \sim 2 \times 10^9$):

$$e^+ + e^- \rightarrow \gamma + \gamma. \tag{2.10}$$

The energy of the electron-positron plasma was transferred to the photons, making the temperature of the photons slightly greater than the neutrino temperature. The ratio of the two temperatures is $\frac{T_\nu}{T_\gamma} = (\frac{4}{11})^{1/3}$.

Big Bang nucleosynthesis. Around 3 minutes after the Big Bang, the universe consists of relativistic particles (photons, electron and positron) in equilibrium, decoupled relativistic particles (neutrinos) and nonrelativistic particles (baryons). Light elements were formed via

the process of Big Bang nucleosynthesis (BBN) at $T \sim 100$ KeV, $z \sim 4 \times 10^8$.

Matter − radiation equality. At this epoch, the energy density of radiation becomes the same as the density of matter. The density in radiation is

$$\frac{\rho_r}{\rho_{cr}} \equiv \frac{\Omega_R}{a^4} = \frac{4.15 \times 10^{-5}}{h^2 a^4}. \tag{2.11}$$

the total energy density of matter (both baryons and dark matter) is

$$\frac{\rho_m}{\rho_{cr}} \equiv \frac{\Omega_m}{a^3}. \tag{2.12}$$

The scale factor at equality is,

$$a_{\text{eq}} = \frac{4.15 \times 10^{-5}}{\Omega_m h^2} \tag{2.13}$$

The redshift of equality is,

$$1 + z_{\text{eq}} = 2.1 \times 10^4 \Omega_m h^2. \tag{2.14}$$

Thus, $z_{\text{eq}} \sim 3400, T \sim 0.75$ eV at equality.

Recombination. At temperature $T \gg 1$ eV, the atoms in the universe are ionized, and photons are tightly coupled to the baryon fluid through rapid Thompson scattering from the free electrons $e^- + \gamma \leftrightarrow e^- + \gamma$. Electrons are tightly coupled to protons through Coulomb scattering. As the temperature drops below 1 eV, electrons and protons combine to form hydrogen atoms $e^- + p \leftrightarrow H + \gamma$. With no electrons to scatter from, photons decouple and stream freely through the universe starting at $z \sim 1000, T \sim 0.3$ eV. These are the cosmic microwave background (CMB) photons we observe today. CMB can help us understand the early universe, since these photons last scattered off electrons at redshift 1100, then travel almost freely through the space. Before the last scattering, photons interact with electrons and stay in equilibrium, and they have a nearly perfect blackbody spectrum.

Dark Ages. $t \sim$ millions of years, $z = 1100 \sim 20$. During this time, there were no visible light photons and the universe was genuinely dark. Nevertheless, it is possible to study Dark Ages with radio wave photons from the 21 cm spin flip transition line of neutral hydrogen.

Star and galaxy formation and evolution. $z \sim 20$. The first star and (small) galaxies begin to form $100 \sim 200$ million years after the Big Bang.

Reionization. $z \sim 20 \sim 6$. The Epoch of Reionization is the process by which, due to the emergence of the first luminous sources, the pre-dominantly neutral intergalactic medium was ionized. Stars, galaxies, quasars, or some combination of them would be the sources of

ionizing radiation.

Today. $T = 2.725$ K, $t \sim 13.7$ Gyr, baryons and the CMB are entirely decoupled, stars and galaxies have been around a long time, and clusters of galaxies (gravitationally bound systems of ~ 1000s of galaxies) are becoming common.

2.3 The Friedmann-Robertson-Walker universe

The Friedmann-Robertson-Walker (FRW) metric describes an expanding homogeneous and isotropic universe, where the line element can be written as

$$ds^2 = g_{\mu\nu}dx^\mu dx^\nu = a^2(-d\eta^2 + \frac{dr^2}{1-Kr^2} + r^2 d\Omega^2)\,, \tag{2.15}$$

where

$$\begin{aligned} K = 0 &\quad \text{Zero curvature, flat geometry,} \\ K = 1 &\quad \text{Positive curvature, closed geometry,} \\ K = -1 &\quad \text{Negative curvature, open geometry.} \end{aligned}$$

In the following discussion we will assume the geometry of the universe to be flat. In what follows, we will use the geodesic equation,

$$\frac{d^2x^\mu}{d\lambda^2} = -\Gamma^\mu_{\alpha\beta}\frac{dx^\alpha}{d\lambda}\frac{dx^\beta}{d\lambda}, \tag{2.16}$$

describing how a free particle travels through space-time, where λ is a affine parameter along the particle's trajectory and $\Gamma^\mu_{\alpha\beta}$ are the Christoffel symbols defined as

$$\Gamma^\mu_{\alpha\beta} = \frac{g^{\mu\nu}}{2}[\frac{\partial g_{\alpha\nu}}{\partial x^\beta} + \frac{\partial g_{\beta\nu}}{\partial x^\alpha} - \frac{\partial g_{\alpha\beta}}{\partial x^\nu}]. \tag{2.17}$$

The Einstein field equations (EFE) connect the geometry described by Einstein tensor and the energy described by the energy-momentum tensor

$$G_{\mu\nu} + \Lambda g_{\mu\nu} = R_{\mu\nu} - \frac{1}{2}g_{\mu\nu}\mathcal{R} + \Lambda g_{\mu\nu} = 8\pi G T_{\mu\nu}. \tag{2.18}$$

where $G_{\mu\nu} \equiv R_{\mu\nu} - \frac{1}{2}g_{\mu\nu}\mathcal{R}$ is the Einstein tensor; $R_{\mu\nu} = \Gamma^\alpha_{\mu\nu,\alpha} - \Gamma^\alpha_{\mu\alpha,\nu} + \Gamma^\alpha_{\beta\alpha}\Gamma^\beta_{\mu\nu} - \Gamma^\alpha_{\beta\nu}\Gamma^\beta_{\mu\alpha}$ is the Ricci curvature tensor, where $\Gamma^\alpha_{\mu\nu,\alpha} \equiv \frac{\partial\Gamma^\alpha_{\mu\nu}}{\partial x^\alpha}$; $\mathcal{R} \equiv g^{\mu\nu}R_{\mu\nu}$ is the scalar curvature, Λ is the cosmological constant; and $T_{\mu\nu}$ is the energy-momentum tensor.

The physical meaning of the components of $T_{\mu\nu}$ is very important. Components of $T_{\beta\alpha}$ can be regarded as the flux of the β-th component of four-momentum across a surface of constant x^α. T^{00} is the time-time component which describes the density of relativistic mass, equivalently energy density. $T^{0i} = T^{i0}$ is the energy flux of relativistic mass across

the x^j surface; T^{ij} is the flux of i-th momentum across the x^j surface, T^{ii} (not summed) is the normal stress, T^{ij} ($i \neq j$) is the shear stress.

$$T^{\mu}_{\nu} = \begin{pmatrix} -\rho & 0 & 0 & 0 \\ 0 & P & 0 & 0 \\ 0 & 0 & P & 0 \\ 0 & 0 & 0 & P \end{pmatrix}.$$

The Bianchi identity, $\nabla_\mu G^{\mu\nu} = 0$, leads to the covariant conservation of the total energy-momentum tensor $\nabla_\mu T^{\mu\nu} = 0$. Here, the covariant equation means that the equation takes the same form in all coordinate systems. The vanishing of the covariant derivative can be written as

$$T^{\mu}{}_{\nu;\mu} = \nabla_\mu T^{\mu}{}_{\nu} = \frac{\partial T^{\mu}{}_{\nu}}{\partial x^\mu} + \Gamma^{\mu}{}_{\alpha\mu} T^{\alpha}{}_{\nu} - \Gamma^{\alpha}{}_{\nu\mu} T^{\mu}{}_{\alpha}, \tag{2.19}$$

Taking the $\nu = 0$ component of Eq.(2.19) and considering a perfect fluid, we get the fluid continuity equation in an expanding universe

$$\frac{\partial \rho}{\partial t} + 3H(1+w)\rho = 0, \tag{2.20}$$

where $w = \frac{P}{\rho}$ is the equation of state parameter. The solution of Eq (2.20) is $\rho = \rho_0 a^{-3(1+w)}$, where ρ_0 is the density at $a = 1$. For the cosmological constant $w_\Lambda = -1$ and the energy density $\rho = \Lambda/(8\pi G)$ remains constant as the universe expands. For non-relativistic matter with no pressure, $w_M = 0$, and the total mass $\rho V \propto \rho a^3$ is conserved, while for radiation $w_R = -1/3$ and $\rho \propto a^{-4}$.

2.3.1 Magnetic fields in a highly conducting plasma

In magnetohydrodynamics (MHD) of a resistive medium, Ohm's law provides a simple relation between the current density and the electric field

$$\mathcal{J}_a = \varsigma E_a \,, \tag{2.21}$$

where ς denotes the electric conductivity of the matter. In highly conducting environments, the conductivity of the medium is almost infinite $\varsigma \to \infty$, and spatial currents can be non-zero even when the electric field vanishes, in which case the electric currents keep the magnetic field frozen in the charged fluid. This is the well known ideal MHD approximation. On the other hand, if the electrical conductivity is zero $\varsigma \to 0$, the spatial currents always vanish even the electric field is non-zero.

To show that magnetic fields can become frozen in, let us consider Maxwell's equations with $c = 1$:

$$\boldsymbol{\nabla} \cdot \mathbf{B} = 0 \tag{2.22}$$

$$\boldsymbol{\nabla} \times \mathbf{E} + \frac{\partial \mathbf{B}}{\partial t} = 0 \tag{2.23}$$

$$\boldsymbol{\nabla} \times \mathbf{B} = 4\pi \mathbf{J}. \tag{2.24}$$

Ohm's law (2.21) in the rest frame is $\mathbf{J}' = \varsigma \mathbf{E}'$, and $\mathbf{E}' = \mathbf{E} + \mathbf{v} \times \mathbf{B}$ in the frame of moving plasma, where $\mathbf{v}$ is the velocity field of plasma, and we get

$$\mathbf{J} = \varsigma(\mathbf{E} + \mathbf{v} \times \mathbf{B}). \tag{2.25}$$

Combining this with Eqs. (2.23) and (2.24), we obtain the induction equation:

$$\begin{aligned} \frac{\partial \mathbf{B}}{\partial t} &= -\boldsymbol{\nabla} \times \mathbf{E} \\ &= \boldsymbol{\nabla} \times \left(\mathbf{v} \times \mathbf{B} - \frac{\boldsymbol{\nabla} \times \mathbf{B}}{4\pi\varsigma} \right) \\ &= \boldsymbol{\nabla} \times (\mathbf{v} \times \mathbf{B}) + \frac{\nabla^2 \mathbf{B}}{4\pi\varsigma} \ , \end{aligned} \tag{2.26}$$

where $\mathbf{v} \times \mathbf{B}$ is the induction term. We used the relationship $\boldsymbol{\nabla} \times (\boldsymbol{\nabla} \times \mathbf{B}) = \boldsymbol{\nabla}(\boldsymbol{\nabla} \cdot \mathbf{B}) - \nabla^2 \mathbf{B} = -\nabla^2 \mathbf{B}$. To show that the magnetic flux remains frozen in the high-conductivity limit, consider a comoving surface S, bounded by a curve C, moving with the fluid. The magnetic flux through this surface is $\Phi = \int_S \mathbf{B} \cdot d\mathbf{S}$. After a time dt, the surface would move to a new surface S'. Thus, the change in flux is given by

$$\Delta\Phi = \int_{S'} \mathbf{B}(t + dt) \cdot d\mathbf{S} - \int_S \mathbf{B}(t) \cdot d\mathbf{S}. \tag{2.27}$$

A 'tube'-like volume swept up by the moving surface S can be written as

$$\oint_S \mathbf{B} \cdot d\mathbf{S} = \int_{S'} \mathbf{B}(t + dt) \cdot d\mathbf{S} - \int_S \mathbf{B}(t + dt) \cdot d\mathbf{S} + \oint_C \mathbf{B}(t + dt) \cdot (d\mathbf{l} \times \mathbf{v}) dt, \tag{2.28}$$

where $d\mathbf{l}$ is the line element along C. Due to the divergence theorem, $\int_V \nabla \cdot \mathbf{B} dV = \oint_S \mathbf{B} \cdot d\mathbf{S}$, and $\nabla \cdot \mathbf{B} = 0$, we obtain

$$\int_{S'} \mathbf{B}(t + dt) \cdot d\mathbf{S} = \int_S \mathbf{B}(t + dt) \cdot d\mathbf{S} - \oint_C \mathbf{B}(t + dt) \cdot (d\mathbf{l} \times \mathbf{v}) dt. \tag{2.29}$$

Applying this in Eq. (2.27), we have

$$\Delta\Phi = \int_S [\mathbf{B}(t + dt) - \mathbf{B}(t)] \cdot d\mathbf{S} - \oint_C \mathbf{B}(t + dt) \cdot (d\mathbf{l} \times \mathbf{v}) dt. \tag{2.30}$$

Applying the limit of $dt \to 0$, and using the relationship $\mathbf{B} \cdot (d\mathbf{l} \times \mathbf{v}) = (\mathbf{v} \times \mathbf{B}) \cdot d\mathbf{l}$, we obtain

$$\frac{d\Phi}{dt} = \int_S \frac{\partial \mathbf{B}}{\partial t} \cdot d\mathbf{S} - \oint_C (\mathbf{v} \times \mathbf{B}) \cdot d\mathbf{l} \tag{2.31}$$

Using the Stoke's theorem $\oint_C (\mathbf{v}\times\mathbf{B})\cdot d\mathbf{l} = \int_S \nabla\times(\mathbf{v}\times\mathbf{B})\cdot d\mathbf{S}$ and the induction equation (2.27), we have

$$\frac{d\Phi}{dt} = \int_S \frac{\nabla^2\mathbf{B}}{4\pi\varsigma}\cdot d\mathbf{S}. \tag{2.32}$$

In the limit of infinite conductivity $\varsigma\to\infty$ (magnetic resistivity is small enough), $\frac{d\Phi}{dt}\to 0$ and so the flux Φ is constant, which proves that the magnetic flux through any loop moving with the fluid is constant, magnetic field lines are frozen into the fluid. Any magnetic field is moving together with the fluid. And, in the limit of infinite conductivity equation (2.27) becomes

$$\frac{\partial\mathbf{B}}{\partial t} = \boldsymbol{\nabla}\times(\mathbf{v}\times\mathbf{B}). \tag{2.33}$$

Also we can see that, when the peculiar velocities vanish ($\mathbf{v}=0$), $\mathbf{B}$ is constant. As we will show in the following section, in an expanding universe, the magnetic field strength decays with the scale factor as $B\propto 1/a^2$.

2.3.2 Magnetic fields from Inflation

Inflationary magnetogenesis [20, 21, 37, 38] is very popular because it solves the coherence scale problem by generating the correlations on superhorizon lengths. However, this model is not perfect if we apply the classical electromagnetic theory and conventional Friedmann models, the primordial magnetic fields generated during de Sitter inflation is too weak to sustain the dynamo amplification [21].

During inflation, the exponential expansion of the de Sitter phase is driven by an approximately constant energy density of the universe. The energy density should scale as a^{-4} in relativistic fluctuation and is diluted by any massive effects. However, the energy density scales as a^{-2} in density perturbations with a coherence length more significant than the Hubble radius. Therefore, the ratio, $\frac{\rho_B}{\rho_\gamma}$ of the magnetic field energy density in the fluctuation relative to the background density decreases as a^{-2} during inflation but grows as a^2 or a during the subsequent radiation dominated era and matter dominated era. The magnetic fields are a relic of inflation. The vacuum fluctuations of the electromagnetic field get amplified during the era of inflation, and subsequently become classical fluctuations in the later phases of the evolution of the universe. However, the electromagnetic Lagrangian is conformally invariant, which means that the equations of motion for the fields are not modified by curvature induced due to a metric that is conformally related to the Minkowski metric. And FRW metric is conformally related to the Minkowski metric, hence no amplification of vacuum fluctuations can happen in this situation. Thus, if we want any amplification, we need to break the conformal invariance of electromagnetism. Ratra [37] proposed a coupling of the form $\sqrt{-g}e^{2\alpha\phi}F^{\mu\nu}F_{\mu\nu}$ between the inflation scalar field ϕ and electromagnetic field

$F_{\mu\nu}$ with α as a free parameter. Ratra showed that under slow roll inflation conditions, this breaking of conformal invariance can cause the amplification of fields.

2.3.3 Magnetic fields from early universe phase transitions

Causal processes could generate the seed primordial magnetic field during a series of phase transitions [23, 26, 39]. For example, during the electroweak phase transition (EWFT) (temperature $\sim$ 100 GeV) and quantum chromodynamic (QCD) phase transition (temperature $\sim$ 150 MeV). The useful parameters are temperature $T_\star$ and the number of relativistic degrees of freedom $g_\star$ when the PMF is generated. To preserve the approximate spatial isotropy, the PMF should be small enough that the energy density can be treated as a first order term in perturbation theory. The PMF should be lower than the magnetic field observed in galaxies because the structure formation will amplify the PMF. The PMF should meet the Big Bang Nucleosynthesis (BBN) bound [40] since the energy density of the PMF contributes to the radiation field.

During the two cosmological phase transitions, there is always a parity violating source, which generates the non-vanishing helicity in magnetic fields. In other words, if we can detect the helicity in the PMF, it will be direct evidence of these parity violations in the early universe. The average energy density and helicity density of the PMF can be related by the realizability condition. We can constrain the helicity of the PMF by using the parity odd CMB power spectra (cross correlations), which should be zero in the standard cosmological scenario without helical magnetic fields or other parity violating sources.

2.3.4 Magnetic helicity

Magnetic helicity [41, 42] provides an essential measure of the topological structure of the magnetic field in terms of twist and linkage of magnetic field lines. Magnetic helicity is defined as a volume integral of the dot product of the vector potential and magnetic field,

$$\mathcal{H} = \int dV\, \mathbf{A} \cdot \mathbf{B}, \tag{2.34}$$

where $\mathbf{A}$ is the gauge potential and $\mathbf{B} = \nabla \times \mathbf{A}(\mathbf{x})$. $\mathbf{A}$ can be redefined by a gauge transformation. Apply a gauge transformation $\mathbf{A} \rightarrow \mathbf{A} + \nabla\chi$, change in magnetic helicity is $\Delta\mathcal{H} = \int \mathbf{B} \cdot \nabla\chi dV = \oint_S \chi \mathbf{B} \cdot d\mathbf{S}$. If $\oint_S \mathbf{B} \cdot d\mathbf{S} = 0$, $\Delta\mathcal{H} = 0$, the definition for the magnetic helicity in Eq.(2.34) is gauge independent.

Since $\frac{\partial \mathbf{B}}{\partial t} = \nabla \times \frac{\partial \mathbf{A}}{\partial t}$ and $\frac{\partial \mathbf{B}}{\partial t} = -\boldsymbol{\nabla} \times \mathbf{E}$, time derivative of vector potential can be written as $\frac{\partial \mathbf{A}}{\partial t} = -\mathbf{E} + \nabla\chi$. We can obtain the evolution of the magnetic helicity

$$
\begin{aligned}
\frac{\partial \mathcal{H}}{\partial t} &= \int dV \, \frac{\partial \mathbf{A}}{\partial t} \cdot \mathbf{B} + \int dV \, \mathbf{A} \cdot \frac{\partial \mathbf{B}}{\partial t} \\
&= \int dV \, (-\mathbf{E} + \nabla\chi) \cdot \mathbf{B} + \int dV \, \mathbf{A} \cdot (-\boldsymbol{\nabla} \times \mathbf{E}) \\
&= \int dV \, (-2\mathbf{E} \cdot \mathbf{B}) + \int dV \, \boldsymbol{\nabla} \cdot (\chi \mathbf{B} + \mathbf{A} \times \mathbf{E}) \\
&= \int dV \, 2 \left(\mathbf{v} \times \mathbf{B} - \frac{\boldsymbol{\nabla} \times \mathbf{B}}{4\pi\varsigma} \right) \cdot \mathbf{B} + \int dV \, \boldsymbol{\nabla} \cdot (\chi \mathbf{B} + \mathbf{A} \times \mathbf{E}) \\
&= -\int dV \, \left(\frac{\boldsymbol{\nabla} \times \mathbf{B}}{2\pi\varsigma} \right) \cdot \mathbf{B} + \int dV \, \boldsymbol{\nabla} \cdot (\chi \mathbf{B} + \mathbf{A} \times \mathbf{E}) \\
&= -\int dV \, \left(\frac{\boldsymbol{\nabla} \times \mathbf{B}}{2\pi\varsigma} \right) \cdot \mathbf{B} + \oint_S (\chi \mathbf{B} + \mathbf{A} \times \mathbf{E}) \cdot d\mathbf{S} \; .
\end{aligned}
\tag{2.35}
$$

During the derivation, we used relationships $\mathbf{A} \cdot (-\boldsymbol{\nabla} \times \mathbf{E}) = \boldsymbol{\nabla} \cdot (\mathbf{A} \times \mathbf{E}) - \mathbf{E} \cdot (\boldsymbol{\nabla} \times \mathbf{A}) = \boldsymbol{\nabla} \cdot (\mathbf{A} \times \mathbf{E}) - \mathbf{E} \cdot \mathbf{B}$, and $\nabla\chi \cdot \mathbf{B} = \boldsymbol{\nabla} \cdot (\chi \mathbf{B}) - \chi \boldsymbol{\nabla} \cdot \mathbf{B} = \boldsymbol{\nabla} \cdot (\chi \mathbf{B})$, and divergence theorem $\int_V \nabla \cdot \mathbf{B} dV = \oint_S \mathbf{B} \cdot d\mathbf{S}$. In the limit of infinite conductivity, the first term is zero. In the case of no boundary terms, the last terms would not contribute, and we obtain that magnetic helicity is a conserved quantity.

Consider two simple cases: When the magnetic field lines are all closed curves, the helicity measures the net linking between all pairs of field lines. We can factor the volume integral into products of line and surface integral $\int dV = \int dl \int dS$, the magnetic flux through surface S is $\Phi = \int_S \mathbf{B} \cdot d\mathbf{S}$. If there are two linked closed curves, the helicity would be $H = 2L\Phi_1\Phi_2 + T_1\Phi_1^2 + T_2\Phi_2^2$ [42], where Φ_1 and Φ_2 are net axial fluxes of the magnetic flux tubes, T_1 and T_2 measure the net twisting of field lines within the tubes about their axes, L is the linking number. When the magnetic field lines extend between parallel planes, the helicity measures the net twist between all pairs of field lines. If there are two tubes stretched between parallel planes, the helicity would be $H = 2w\Phi_1\Phi_2 + T_1\Phi_1^2 + T_2\Phi_2^2$ [42], where w is the winding number.

Chapter 3

Cosmological perturbations and the Cosmic Microwave Background

3.1 Cosmological perturbations

The FRW metric describes an isotropic and homogeneous universe. However, we know that the universe is not perfectly FRW even on cosmological scales and one needs to take into account perturbations around the FRW metric. The contravariant components of a perturbed FRW metric can be written as

$$\begin{aligned} g^{00} &= -a^{-2}(\eta)\,\{1-2A(\vec{x},\eta)\}\,, \\ g^{0i} &= -a^{-2}(\eta)\,B^i(\vec{x},\eta)\,, \\ g^{ij} &= a^{-2}(\eta)\,\left\{(1-2H_L(\vec{x},\eta))\delta^{ij}-2H_T^{ij}(\vec{x},\eta)\right\}, \end{aligned} \tag{3.1}$$

with the covariant counterparts given by

$$\begin{aligned} g_{00} &= -a^{2}(\eta)\,\{1+2A(\vec{x},\eta)\}\,, \\ g_{0i} &= -a^{2}(\eta)\,B_i(\vec{x},\eta)\,, \\ g_{ij} &= a^{2}(\eta)\,\{(1+2H_L(\vec{x},\eta))\delta_{ij}+2H_{Tij}(\vec{x},\eta)\}\,, \end{aligned} \tag{3.2}$$

where A is a scalar potential, B_i is a vector shift, H_L is the scalar perturbation of the spatial curvature, and H_{Tij} is a trace-free distortion of the spatial metric. A, B_i, H_L and H_{Tij} provide the 10 functions required to specify the $4(4+1)/2 = 10$ components of the symmetric 4×4 tensor $g_{\mu\nu}$.

Note that not all of the above 10 functions can independently contribute to physical (*i.e. observable*) manifestations of the metric, since their definition depends on how one defines the slices of uniform scale factor. For example, one could choose to work in a coordinate system in which the scalar potential A vanishes, or with respect to which the dark matter density fluctuations vanish. This freedom in the choice of coordinates (3 spatial + 1 time),

known as the "gauge-freedom", allows one to set 4 out of the 10 metric functions to zero. We will use the synchronous gauge, defined in Sec. 3.3.1.

The energy-momentum tensor $T_{\mu\nu}$ can be divided into fluid (f) contributions and seed (s) contributions. The fluid part includes the equilibrated particles and radiation, while the latter describes the out-of-equilibrium configurations, such as the frozen-in PMF or topological defects like cosmic strings. The background energy-momentum is assumed to have a negligible contribution from the seeds,

$$T^0{}_0 = -\rho_f, \qquad T^0{}_i = T_0{}^i = 0, \qquad T^i{}_j = p_f \delta^i{}_j \,, \tag{3.3}$$

while the perturbations of $T_{\mu\nu}$ can be written as

$$\begin{aligned}
\delta T^0{}_0 &= -\rho_s - \delta\rho_f \,, \\
\delta T^0{}_i &= (\rho_f + p_f)(v_i - B_i) + v_{si} \,, \\
\delta T_0{}^i &= -(\rho_f + p_f)v^i + v_s^i \,, \\
\delta T^i{}_j &= (p_s + \delta p_s)\delta^i{}_j + \delta p_f \delta^i{}_j + p_f \Pi^i{}_j \,,
\end{aligned} \tag{3.4}$$

where $\delta\rho$ is a scalar density perturbation, δp is a scalar pressure perturbation, v_i is a vector velocity, and $\Pi^i{}_j$ is a tensor anisotropic stress perturbation. Just like in the case of the $g_{\mu\nu}$, there is a total of 10 different components of the stress-energy tensor. With the covariant conservation of energy-momentum, $\nabla^\mu T_{\mu\nu} = 0$, providing 4 equations relating them, only 6 out of the 10 components are independent. We will work to linear order in perturbation theory, which means dropping terms of higher orders, such as $\delta p \delta\rho$.

It is convenient to work in Fourier space, with the transformation given as

$$\delta\rho(\vec{k}, \eta) = \int \delta\rho(\vec{x}, \eta) e^{-i\vec{k}\cdot\vec{x}} d^3\vec{x} \tag{3.5}$$

Each linear perturbation Fourier mode evolves independently within first order perturbation, allowing us to work with a set a of ordinary differential equations in instead of partial differential equations. Vectors and tensors can be decomposed into appropriately defined normal modes. The scalar, vector and tensor mode eigenfunctions of the Laplacian operator form a complete set of basis functions, *i.e.*

$$\begin{aligned}
\nabla^2 Q^{(0)} &= -k^2 Q^{(0)} \,, \\
\nabla^2 Q^{(\pm 1)} &= -k^2 Q^{(\pm 1)} \,, \\
\nabla^2 Q^{(\pm 2)} &= -k^2 Q^{(\pm 2)} .
\end{aligned} \tag{3.6}$$

Since we consider a flat universe, the eigenmodes are plane waves and can be written as

$$\begin{aligned} Q^{(0)} &= e^{i\vec{k}\cdot\vec{x}}\,, \\ Q_i^{(\pm 1)} &= \frac{-i}{\sqrt{2}}(\hat{\mathbf{e}}^1 \pm i\hat{\mathbf{e}}^2)_i e^{i\vec{k}\cdot\vec{x}}\,, \\ Q_{ij}^{(\pm 2)} &= -\sqrt{\frac{3}{8}}(\hat{\mathbf{e}}^1 \pm i\hat{\mathbf{e}}^2)_i(\hat{\mathbf{e}}^1 \pm i\hat{\mathbf{e}}^2)_j e^{i\vec{k}\cdot\vec{x}}, \end{aligned} \tag{3.7}$$

where $\hat{\mathbf{e}}^1$ and $\hat{\mathbf{e}}^2$ are unit vectors and orthogonal to $\mathbf{k}$. The vector modes are divergence-less and represent vorticity, the tensor modes are transverse and traceless and represent the gravitational waves.

$$\nabla^i Q_i^{(\pm 1)} = 0, \qquad \nabla^i Q_{ij}^{(\pm 2)} = 0, \qquad .\delta^{ij} Q_{ij}^{(\pm 2)} = 0\,. \tag{3.8}$$

The scalar mode vector and tensor functions are obtained by taking derivatives of Q^0:

$$Q_i^{(0)} = -k^{-1}\nabla^i Q^{(0)}\,, \tag{3.9}$$

$$Q_{ij}^{(0)} = (-k^{-2}\nabla_i\nabla_j + \frac{1}{3}\delta_{ij})Q^{(0)}\,, \tag{3.10}$$

$$Q_{ij}^{(\pm 1)} = -\frac{\nabla_i Q_j^{(\pm 1)} + \nabla_j Q_i^{(\pm 1)}}{2k}\,. \tag{3.11}$$

The basis functions have the following properties that will be used later;

$$Q_{ij}^{(\pm 1)} Q_{ij}^{(\mp 1)} = \frac{1}{2}, \qquad Q_{ij}^{(\pm 2)} Q_{ij}^{(\mp 2)} = \frac{3}{2}, \qquad \delta_{ij} Q_{ij}^{(\pm 2)} = 0, \qquad \widehat{k}_i Q_{ij}^{(\pm 2)} = 0. \tag{3.12}$$

The scalar metric and energy-momentum variables can be expressed in terms of the normal modes as

$$\begin{aligned} A(\vec{x}) &= A(k)Q^{(0)}, \qquad H_L(\vec{x}) = H_L(k)Q^{(0)} \\ \delta\rho(\vec{x}) &= \delta\rho(k)Q^{(0)}, \qquad \delta p(\vec{x}) = \delta p(k)Q^{(0)} \end{aligned} \tag{3.13}$$

and similarly for other quantities. For vector modes, we have

$$B_i(\vec{x}) = \sum_{m=-1}^{1} B^{(m)}(k)Q_i^{(m)}, \qquad v_i(\vec{x}) = \sum_{m=-1}^{1} v^{(m)}(k)Q_i^{(m)}. \tag{3.14}$$

and for tensor modes,

$$H_{Tij}(\vec{x}) = \sum_{m=-2}^{2} H_T^{(m)}(k)Q_{ij}^{(m)}, \qquad \Pi_{ij}(\vec{x}) = \sum_{m=-2}^{2} \Pi^{(m)}(k)Q_{ij}^{(m)}. \tag{3.15}$$

3.2 The Boltzmann Equation

The different components of the universe interact with each other and it is generally quite complicated to solve for their evolution exactly. During the times before recombination, photons are tightly coupled with electrons and proton by Coulomb interactions. In addition, both relativistic (photons and neutrinos)and non-relativistic (dark matter and baryons) particles are affected by gravity (the metric). We will use a system of coupled Boltzmann and Einstein equations to study evolution of the anisotropies in relativistic components and inhomogeneities in the matter.

The energy density of species i with a distribution function $f_i(\vec{x}, \vec{p})$ and energy $E(p)$ is

$$\rho_i = g_i \int \frac{d^3p}{(2\pi)^3} f_i(\vec{x}, \vec{p}) E(p), \tag{3.16}$$

where g_i is the degeneracy of the species. When particles are in equilibrium at temperature T, the Bose-Einstein distribution describes the integer spin particles (such as photons)

$$f_{BE} = \frac{1}{e^{(E-\mu)/T} - 1}, \tag{3.17}$$

while the Fermi-Dirac distribution describes fermions such as electrons,

$$f_{FD} = \frac{1}{e^{(E-\mu)/T} + 1} \tag{3.18}$$

where μ is the chemical potential. As the universe is homogeneous and isotropic, the distribution function depends only on the magnitude of the momentum p, and is in independent on $\vec{x}$. Applying the Bose-Einstein distribution to photons and there is no chemical potential, the photon energy density is

$$\rho_\gamma = \frac{\pi^2}{15} T^4. \tag{3.19}$$

The energy density of radiation scales as a^{-4} and the temperature of CMB photons observed today is $T = 2.725$. Thus,

$$\Omega_\gamma(a) = \frac{\rho_\gamma}{\rho_{cr}} = \frac{\pi^2}{15} (\frac{2.725K}{a})^4 \frac{1}{8.098 \times 10^{-11}\,\mathrm{eV}^4} \frac{1}{h^2} = \frac{2.47 \times 10^{-5}}{h^2 a^4}. \tag{3.20}$$

The Boltzmann equation can be written as

$$\frac{df}{dt} = C[f] \tag{3.21}$$

where $C[f]$ denotes all the collision terms due to interaction of photons with baryons and electrons.

In the absence of collisions, the phase space density of particles is conserved along a trajectory, and after applying linear perturbation theory in the unperturbed universe, we

can simplify Eq.(3.21) to the Liouville equation

$$\frac{df}{d\eta} = \frac{\partial f}{\partial \eta} + \frac{\partial f}{\partial x^i} \cdot \frac{dx^i}{d\eta} + \frac{\partial f}{\partial p}\frac{dp}{d\eta} + \frac{\partial f}{\partial \hat{p}^i} \cdot \frac{d\hat{p}^i}{d\eta} = 0, \tag{3.22}$$

where $\hat{\vec{p}}$ is a unit vector of $\vec{p}$. The term $\frac{\partial f}{\partial p}\frac{dp}{d\eta}$ represents the gravitational red-shifting (or the Sachs-Wolfe effect) of the photons. We will work in Fourier, since each Fourier mode evolves independently in linear perturbation theory, and use the conformal time η instead of t as our basic time variable so that, from now on, the overdot represents $\partial/\partial\eta$. And to do the linear perturbation theory, we only need the first-order equations, so we will drop all high order terms. In the unperturbed universe, $\dot{\hat{p}}^i = 0$ (the universe is isotropic), so $\dot{\hat{p}}^i$ is a first order in perturbation theory. But $\frac{\partial f}{\partial \hat{p}^i}$ is also a first order, so their product is a second order. The last term can be dropped. Rearranging them, we obtain for $\dot{f}$:

$$\dot{f} = -\hat{p}^i \frac{\partial f}{\partial x^i} - \dot{p}\frac{\partial f}{\partial p}. \tag{3.23}$$

Using the metric (3.2) and applying the geodesic equation, we can express the momentum evolution of a massless particle as

$$\dot{p} = -(aH + \hat{p}^i \frac{\partial A}{\partial x^i} + \hat{p}^i\hat{p}^j \frac{\partial B_i}{2\partial x^j} + \dot{H}_L + \hat{p}^i\hat{p}^j \dot{H}_{Tij})p. \tag{3.24}$$

Eq. (3.23) can then be written as

$$\dot{f}(x^i, p, \hat{p}^i; \eta) = -\hat{p}^i \frac{\partial f}{\partial x^i} + p\frac{\partial f}{\partial p}(aH + \hat{p}^i \frac{\partial A}{\partial x^i} + \hat{p}^i\hat{p}^j \frac{\partial B_i}{2\partial x^j} + \dot{H}_L + \hat{p}^i\hat{p}^j \dot{H}_{Tij}). \tag{3.25}$$

The zeroth-order photon distribution is simply the Bose-Einstein distribution $f^{(0)} = \frac{1}{e^{p/T}-1}$. It is convenient to write the perturbed distribution as

$$f(x^i, p, \hat{p}^i; \eta) = \{\exp\frac{p}{T(\eta)[1 + \Theta(x^i, \hat{p}^i, \eta)]} - 1\}^{-1}, \tag{3.26}$$

where the photon perturbation variable is defined as $\Theta = \delta T/T$. The zeroth-order temperature $T(\eta)$ scales as a^{-1}, which is independent of space (homogeneous: not depend on $\vec{x}$; isotropy: not depend on $\hat{p}$). And we can define the analogous variable for neutrinos, $\mathcal{N}(x^i, \hat{p}^i, \eta)$. For non-relativistic components such as dark matter and baryons, we need to consider the overdensity $\delta(x^i, \eta)$ and velocity $v(x^i, \eta)$.

Considering the perturbed Boltzmann equation, we write f as a homogeneous solution plus a perturbation.

$$\dot{f} = \dot{f}^{(0)} + \delta\dot{f} = \dot{f}^{(0)} - \Theta\dot{T}\frac{\partial}{\partial T}(\frac{\partial f^{(0)}}{\partial p}p) - \frac{\partial f^{(0)}}{\partial p}p\dot{\Theta}. \tag{3.27}$$

Using Eqs. (3.25) and (3.27) we can get the full evolution equation for the temperature perturbation:

$$\dot{\Theta} = -\hat{p}^i \frac{\partial \Theta}{\partial x^i} + aHp\frac{\partial \Theta}{\partial p} - \hat{p}^i \frac{\partial A}{\partial x^i} - \hat{p}^i \hat{p}^j \frac{\partial B_i}{2\partial x^j} - \dot{H}_L - \hat{p}^i \hat{p}^j \dot{H}_{Tij}. \tag{3.28}$$

The full Boltzmann Equation has a collision term on the right hand side, which cannot be ignored since photons were scattered off the free electrons. Following the common approach (*e.g* see [43]), we will treat polarization perturbations in units of temperature, rather than intensity. We will also ignore the circular polarization Stokes parameter V since the Thomson scattering alone cannot lead to circular polarization. Thus, it is sufficient to consider the three Stokes parameters I, Q and V, combined into a vector

$$\vec{T} = \Big(\Theta, Q + iU, Q - iU\Big). \tag{3.29}$$

The Boltzmann equation gives the evolution of the vector $\vec{T}$ as

$$\frac{d}{d\eta}\vec{T}(\eta, \vec{x}, \hat{n}) = \frac{\partial}{\partial \eta}\vec{T} + n^i \nabla_i \vec{T} = \vec{C}[\vec{T}] + G[h_{\mu\upsilon}], \tag{3.30}$$

where $C[\vec{T}]$ is the Thomson collision term and $G[h_{\mu\upsilon}]$ describes the gravitational redshift in a perturbed metric.

In the total angular momentum representation of [43], the temperature and polarization fluctuations can be decomposed into normal modes of the spatial and angular distributions as

$$\Theta(\eta, \vec{x}, \hat{n}) = \int \frac{d^3k}{(2\pi)^3} \sum_l \sum_m \Theta_l^{(m)} G_l^m \tag{3.31}$$

and

$$(Q \pm iU)(\eta, \vec{x}, \hat{n}) = \int \frac{d^3k}{(2\pi)^3} \sum_l \sum_m (E_l^{(m)} \pm iB_l^{(m)})_{\pm 2} G_l^m, \tag{3.32}$$

where

$${}_{\pm s}G_l^m = (-i)^l \sqrt{\frac{4\pi}{2l+1}} {}_{\pm s}Y_l^m(\hat{n}) e^{(i\vec{k}\cdot\vec{x})}, \tag{3.33}$$

${}_0Y_l^m$ are the ordinary spherical harmonics and ${}_{\pm 2}Y_l^m$ are the spin-2 spherical harmonics, which are related to the ordinary spherical harmonics as

$${}_{\pm 2}Y_l^m = \left[\tfrac{(l-2)!}{(l+2)!}\right]^2 \left[\partial_\theta^2 - \cot\theta\partial_\theta \pm \tfrac{2i}{\sin\theta}(\partial_\theta - \cot\theta)\partial_\phi - \tfrac{1}{\sin^2\theta}\partial_\phi^2\right] Y_l^m. \tag{3.34}$$

In particular, spins $s = 0$ and $s = \pm 2$ correspond to the temperature fluctuations and polarization anisotropies, respectively. The $m = 0, m = \pm 1, m = \pm 2$ modes describe the scalar, vector and tensor perturbations, respectively. Coefficients $E_l^{(m)}$ have parity $(-1)^l$ and represent the 'electric' polarization called the E-mode. The $B_l^{(m)}$'s have parity $(-1)^{l+1}$

and represent the 'magnetic' polarization called the B-mode. In general, the angular power spectra of the correlation functions can be calculated as

$$C_l^{X\tilde{X}} = \frac{2}{\pi}\frac{1}{(2l+1)^2}\int k^2 dk \sum_m X_l^{(m)*}(\eta_0,k)\tilde{X}_l^{(m)}(\eta_0,k) \tag{3.35}$$

where X can be either Θ, E or B.

3.2.1 The temperature-polarization Boltzmann hierarchy and the integral solution

To put the Boltzmann equation into a form suitable for solving it numerically, we write it in terms of the normal modes defined in the previous subsection

$$\dot{\Theta}_l^{(m)} = k\left[\tfrac{\sqrt{l^2-m^2}}{2l-1}\Theta_{l-1}^{(m)} - \tfrac{\sqrt{(l+1)^2-m^2}}{2l+3}\Theta_{l+1}^{(m)}\right] - \dot{\tau}\Theta_l^{(m)} + S_l^{(m)}, \tag{3.36}$$

where the gravitational and scattering sources are

$$S_l^{(m)} = \begin{pmatrix} \dot{\tau}\Theta_0^{(0)} - \dot{H}_L^{(0)} & \dot{\tau}v_b^{(0)} + \dot{B}^{(0)} & \dot{\tau}P^{(0)} - \frac{2}{3}\sqrt{1-3K/k^2}\dot{H}_T^{(0)} \\ 0 & \dot{\tau}v_b^{(\pm1)} + \dot{B}^{(\pm1)} & \dot{\tau}P^{(\pm1)} - \frac{\sqrt{3}}{3}\sqrt{1-2K/k^2}\dot{H}_T^{(\pm1)} \\ 0 & 0 & \dot{\tau}P^{(\pm2)} - \dot{H}_T^{(\pm2)} \end{pmatrix}, \tag{3.37}$$

$v_B^{(m)}$ is the baryon velocity, and the term $P^{(m)}$ is defined as

$$P^{(m)} = \frac{1}{10}\left[\Theta_2^{(m)} - \sqrt{6}E_2^{(m)}\right]. \tag{3.38}$$

The analogous equations for the polarization are

$$\begin{aligned}\dot{E}_l^{(m)} = k\left[\tfrac{1}{2l-1}\sqrt{\tfrac{(l^2-m^2)(l^2-4)}{l^2}}E_{l-1}^{(m)} - \tfrac{2m}{l(l+1)}B_l^{(m)} - \tfrac{1}{2l+3}\sqrt{\tfrac{[(l+1)^2-m^2](l+3)(l-1)}{(l+1)^2}}E_{l+1}^{(m)}\right] \\ -\dot{\tau}\left[E_l^{(m)} + \sqrt{6}P^{(m)}\delta_{l2}\right],\end{aligned} \tag{3.39}$$

$$\begin{aligned}\dot{B}_l^{(m)} = k\left[\tfrac{1}{2l-1}\sqrt{\tfrac{(l^2-m^2)(l^2-4)}{l^2}}B_{l-1}^{(m)} + \tfrac{2m}{l(l+1)}E_l^{(m)} - \tfrac{1}{2l+3}\sqrt{\tfrac{[(l+1)^2-m^2](l+3)(l-1)}{(l+1)^2}}B_{l+1}^{(m)}\right] \\ -\dot{\tau}B_l^{(m)}.\end{aligned} \tag{3.40}$$

The analytical solutions to the above Boltzmann equations can be written as

$$\begin{aligned}\Theta_l^{(m)}(\eta_0,k) &= (2l+1)\int_0^{\eta_0} d\eta e^{-\tau}\sum_{l'} S_{l'}^{(m)}(\eta) j_l^{(l'm)}(\chi), \\ E_l^{(m)}(\eta_0,k) &= -\sqrt{6}(2l+1)\int_0^{\eta_0} d\eta e^{-\tau}\dot{\tau}\epsilon_l^{(m)}(\chi)P^{(m)}(\eta), \\ B_l^{(m)}(\eta_0,k) &= -\sqrt{6}(2l+1)\int_0^{\eta_0} d\eta e^{-\tau}\dot{\tau}\beta_l^{(m)}(\chi)P^{(m)}(\eta),\end{aligned} \tag{3.41}$$

where the radial functions $j_l^{(l'm)}$ are related to $G_{l'}^m$ via

$$G_{l'}^m = \sum_l (-i)^l \sqrt{4\pi(2l+1)} j_l^{(l'm)}(x) Y_l^m(\hat{n}), \tag{3.42}$$

where the lowest (l', m) radial functions $j_l^{(l'm)}$ are

$$\begin{aligned} j_l^{(00)}(x) = j_l(x) \qquad j_l^{(10)}(x) = j_l{}'(x) \qquad j_l^{(20)}(x) = \frac{1}{2}[3j_l{}''(x) + j_l(x)] \\ j_l^{(11)}(x) = \sqrt{\frac{l(l+1)}{2}} \frac{j_l(x)}{x} \qquad j_l^{(21)}(x) = \sqrt{\frac{3l(l+1)}{2}} \frac{j_l(x)'}{x} \\ j_l^{(21)}(x) = \sqrt{\frac{3(l+2)!}{8(l-2)!}} \frac{j_l(x)}{x^2} \end{aligned} \tag{3.43}$$

and the primes represent derivatives with respect to the variable x. Similarly,

$${}_{\pm 2}G_2^m = \sum_l (-i)^l \sqrt{4\pi(2l+1)} [\epsilon_l^{(m)}(x) \pm i\beta_l^{(m)}(x)]_{\pm 2} Y_l^m(\hat{n}), \tag{3.44}$$

where

$$\begin{aligned} \epsilon_l^{(0)}(x) &= \sqrt{\frac{3(l+2)!}{8(l-2)!}} \frac{j_l(x)}{x^2}, \\ \epsilon_l^{(1)}(x) &= \frac{1}{2}\sqrt{(l-1)(l+2)} \left[\tfrac{j_l(x)}{x^2} + \tfrac{j_l'(x)}{x}\right], \\ \epsilon_l^{(2)}(x) &= \frac{1}{4}\left[-j_l(x) + j_l''(x) + 2\tfrac{j_l(x)}{x^2} + 4\tfrac{j_l'(x)}{x}\right], \\ \epsilon_l^{(m)} &= \epsilon_l^{(-m)}, \end{aligned} \tag{3.45}$$

and

$$\begin{aligned} \beta_l^{(0)}(x) &= 0, \\ \beta_l^{(1)}(x) &= \frac{1}{2}\sqrt{(l-1)(l+2)} \frac{j_l(x)}{x}, \\ \beta_l^{(2)}(x) &= \frac{1}{2}\left[j_l'(x) + 2\tfrac{j_l(x)}{x}\right], \\ \beta_l^{(m)} &= -\beta_l^{(-m)}. \end{aligned} \tag{3.46}$$

The above analytical solutions require knowing the source functions $S_l^{(m)}$, which themselves depend on the first few moments of the temperature and polarization moments. To solve the system, one can employ the approximate scheme, introduced by Seljak and Zaldarriaga [44, 45], in which one first solves equations (3.36), truncating the hierarchy at a finite $l \sim 30$, and then substitutes these solutions into the "line-of-sight" integrals 3.41 to find the moments at all l.

3.3 Einstein and conservation equations

The covariant Einstein equations for the scalar modes are

$$
\begin{aligned}
(k^2-3K)[H_L+\frac{1}{3}H_T+\frac{\dot a}{a}(\frac{B}{k}-\frac{\dot H_T}{k^2})] &= 4\pi G a^2\left[\delta\rho+3\frac{\dot a}{a}(\rho+p)\frac{v-B}{k}\right],\\
k^2(A+H_L+\frac{1}{3}H_T)+\left(\frac{d}{d\eta}+2\frac{\dot a}{a}\right)(kB-\dot H_T) &= -8\pi G a^2 p\Pi\,,\\
\frac{\dot a}{a}A-\dot H_L-\frac{1}{3}\dot H_T-\frac{K}{k^2}(kB-\dot H_T) &= 4\pi G a^2(\rho+p)\frac{v-B}{k}\,,\\
\left[2\frac{\ddot a}{a}-2\left(\frac{\dot a}{a}\right)^2+\frac{\dot a}{a}\frac{d}{d\eta}-\frac{k^2}{3}\right]A-\left[\frac{d}{d\eta}+\frac{\dot a}{a}\right](\dot H_L+\frac{kB}{3}) &= 4\pi G a^2(\delta p+\frac{1}{3}\delta\rho)\,.
\end{aligned}
\tag{3.47}
$$

The nonrelativistic particles, such as baryons and dark matter, do not contribute to anisotropic stress. And we obtain the continuity and Navier-Stokes equations by applying the perturbations to the conservation equations.

$$\left[\frac{d}{d\eta}+3\frac{\dot a}{a}\right]\delta\rho+3\frac{\dot a}{a}\delta p=-(\rho+p)(kv+3\dot H_L)\,, \tag{3.48}$$

$$\left[\frac{d}{d\eta}+4\frac{\dot a}{a}\right](\rho+p)\frac{v-B}{k}=\delta p-\frac{2}{3}(1-3\frac{K}{k^2})p\Pi+(\rho+p)A\,. \tag{3.49}$$

The Navier-Stokes equation can be simplified to the Euler equation if there is no anisotropic stress. These equations remain true for each fluid individually in the absence of momentum exchange, e.g., for cold dark matter. The baryons have an additional term $\frac{\dot\tau}{R}(\Theta_1^{(0)}-v_B^{(0)})$ to the Euler equation due to momentum exchange from Compton scattering with the photons.

For a seed source, the conservation equations become

$$
\begin{aligned}
\dot\rho_s &= -3\frac{\dot a}{a}(\rho_s+p_s)-kv_s^{(0)}\,,\\
\dot v_s^{(0)} &= 3\frac{\dot a}{a}v_s^{(0)}+k[p_s-\frac{2}{3}(1-\frac{3K}{k^2})\pi_s^{(0)}]\,,
\end{aligned}
\tag{3.50}
$$

which is independent of gauge since the metric fluctuations produce higher order terms.

The covariant vector mode Einstein equations are

$$
\begin{aligned}
(1-\frac{2K}{k^2})(kB^{(\pm1)}-\dot H_T^{(\pm1)}) &= 16\pi G a^2(\rho+p)\frac{v^{(\pm1)}-B^{(\pm1)}}{k}\,,\\
\left[\frac{d}{d\eta}+2\frac{\dot a}{a}\right](kB^{(\pm1)}-\dot H_T^{(\pm1)}) &= -8\pi G a^2 p\Pi^{(\pm1)}\,,
\end{aligned}
\tag{3.51}
$$

and the vector conservation equations are

$$\left[\frac{d}{d\eta}+4\frac{\dot a}{a}\right](\rho+p)\frac{v^{(\pm1)}-B^{(\pm1)}}{k}=-\frac{1}{2}(1-2\frac{K}{k^2})p\Pi^{(\pm1)}\,. \tag{3.52}$$

The tensor mode Einstein equation is

$$\left[\frac{d^2}{d\eta^2} + 2\frac{\dot{a}}{a}\frac{d}{d\eta} + (k^2 + 2K)\right] H_T^{(\pm 2)} = 8\pi G a^2 p \Pi^{(\pm 2)}\,, \tag{3.53}$$

which is true for all gauges because tensor perturbations are gauge-invariant.

3.3.1 The synchronous gauge equations

To solve the perturbation equations numerically we will be using CAMB, in which equations are written in the synchronous gauge. The synchronous gauge confines the metric perturbations to the spatial degrees of freedom

$$\begin{aligned} A &= B = 0\,, \\ \eta_T &\equiv -\frac{1}{3}H_T - H_L\,, \\ h_L &= 6H_L\,. \end{aligned} \tag{3.54}$$

The variables η_T and h_L form a stable system for numerical solutions and hence the synchronous gauge has been extensively used in numerical solutions. According to Eq.(3.47), the Einstein equations for a flat universe in synchronous gauge are

$$\begin{aligned} \dot{\eta}_T &= 4\pi G a^2 (\rho + p)\frac{v}{k}\,, \\ \ddot{h}_L + \frac{\dot{a}}{a}\dot{h}_L &= -8\pi G a^2 (\delta\rho + 3\delta p)\,, \\ -k^2\eta_T + \frac{1}{2}\frac{\dot{a}}{a}\dot{h}_L &= 4\pi G a^2 \delta\rho\,, \end{aligned} \tag{3.55}$$

while the conservation equations are

$$\delta\dot{\rho}_J + 3\frac{\dot{a}}{a}(\delta\rho_J + \delta p_J) = -(\rho_J + p_J)(kv_J + \frac{1}{2}\dot{h})\,, \tag{3.56}$$

$$\left[\frac{d}{d\tau} + 4\frac{\dot{a}}{a}\right](\rho_J + p_J)\frac{v_J}{k} = \delta p_J - \frac{2}{3}p_J\Pi_J\,. \tag{3.57}$$

Note that the lack of the potential A in the synchronous gauge implies that there are no gravitational forces in the Navier-Stokes equation. Hence, for stress-free matter like cold dark matter, zero velocity initially implies zero velocity always.

The vector Einstein equation (3.51) for synchronous gauge and flat universe becomes

$$\ddot{H}_T^{(\pm 1)} + 2\frac{\dot{a}}{a}\ddot{H}_T^{(\pm 1)} = -8\pi G a^2 (p_f \Pi_f^{(\pm 1)} + \pi_s^{(\pm 1)}), \tag{3.58}$$

and the conservation equation is

$$\dot{v}_f^{(\pm 1)} = -(1 - 3c_f^2)\frac{\dot{a}}{a}v_f^{(\pm 1)} + \frac{1}{2}k\frac{w_f}{1+w_f}\pi_f^{(\pm 1)}. \tag{3.59}$$

where $c_f^2 = \frac{\dot{p}_f}{\dot{\rho}_p}$ is the sound speed.

The seed Euler equation is given by

$$\dot{v}_s^{(\pm 1)} = -4\frac{\dot{a}}{a}v_s^{(\pm 1)} + k[p_s - \frac{1}{2}k\pi_s^{(\pm 1)}]\,. \tag{3.60}$$

The Einstein equation for the tensor modes (3.53) is the same in all gauges, and in a flat Universe it is

$$\ddot{H}_T^{(\pm 2)} + 2\frac{\dot{a}}{a}\dot{H}_T^{(\pm 2)} + k^2 H_T^{(\pm 2)} = 8\pi G a^2 p\Pi^{(\pm 2)}\,. \tag{3.61}$$

Chapter 4

Primordial magnetic fields and CMB Fluctuations induced by them

The PMF would affect the anisotropy and polarization of the CMB [46, 47] if magnetic fields were existing at the time of decoupling or soon after. A nearly homogeneous and very large scale field, which would have a particular direction, would cause an anisotropic expansion in this direction, resulting in a quadrupole anisotropy in the CMB (for example, see [48]). This leads to a tight bound of several nG [49] on the strength of a homogeneous field redshifted to today. The existing primordial magnetogenesis scenarios are more likely to produce stochastic tangled fields, that are Gaussian distributed and can be described in terms of their power spectrum. The spectrum is often normalized in terms of a quantity B_λ, which is the strength of the PMF after smoothing it over a region of size λ (Eq. 4.11), rescaled to the present epoch, assuming it decreases with the expansion as $B = B_0/a^2(t)$. The magnetic and radiation energy densities both scale with expansion as $1/a^4$.

The scalar, vector and tensor components of the perturbed stress tensor associated with the PMF would source the corresponding metric perturbations in CMB, including gravitational waves. Furthermore, the scalar part of the Lorentz force contributes to the scalar fluid velocity and associated density perturbations, while its vector part leads to the vortical (vector) fluid velocity perturbation. In the next chapter, we will see some large and small angular scale anisotropies in the CMB temperature and polarization due to these magnetically induced metric and velocity perturbations. Any large-scale helical component of the magnetic field has a parity violation effect, which would source non-zero parity odd T-B and E-B cross-correlations, which are not expected in standard inflationary models.

There are other observable effects that the PMF can have on the CMB. The magnetic field in the intergalactic medium can lead to Faraday rotation of the polarized component of the CMB, which will generate B-mode signals by rotating the existing inflationary E-mode signal. Also, the Big Bang Nucleosynthesis (BBN) constrains the radiation fraction at the

time of nucleosynthesis, limiting the PMF to $B \lesssim 10^{11}$ G at the time of nucleosynthesis [50], which translates to $B \lesssim 7 \times 10^{-7}$ G at present [51].

4.1 The Two-Point Correlation of the PMF Energy Momentum Tensor

We assume that the primordial stochastic magnetic field is generated before the radiation-matter equality, during or before the radiation dominated epoch. Before the time of recombination, the electric conductivity of the primordial plasma on scales larger than the Silk scale λ_S is substantial, allowing us to work in the infinite conductivity limit. Thus, the 'frozen-in' condition holds, and the infinite conductivity leads to the vanishing of the induced electric field. In this approximation, all the complications of MHD vanish. On sufficiently large scales, the PMF evolves like a stiff source and one can neglect the effects of backreaction of the fluid on the evolution of the magnetic field. The energy density of the field is treated as a first-order perturbation to the standard FLRW homogeneous cosmological spacetime model. The time dependence decouples from the spatial structure on sufficiently large scales, and, due to flux conservation, the magnetic field evolves like $\mathbf{B}_{phys}(\eta, \mathbf{x}) = \mathbf{B}(\eta_0, \mathbf{x})/a(\eta)^2$, where we use the normalization $a(\eta_0) = 1$ and a subscript $'0'$ denotes today and $\mathbf{B}(\mathbf{x})$ is the comoving field. On small scales, a PMF is damped because of the photon and neutrino viscosities [52], and we will account for this damping by imposing an ultraviolet cutoff at a wavelength k_D in the magnetic power spectrum.

We consider magnetic fields which are statistically isotropic and homogeneous, since the magnetic field generated in the early universe undergoes a random and stochastic process. Generally, as mentioned before, we work in Fourier space. For an inhomogeneous distribution of a scalar field, with a mean density $\bar{n}$, the inhomogeneity contrast is $\delta(\vec{x}) = (n(\vec{x}) - \bar{n})/\bar{n}$, and the power spectrum in Fourier space is defined via

$$\langle \delta(\vec{k})\delta(\vec{k'})\rangle = (2\pi)^3 P(k)\delta^3(\vec{k} - \vec{k'}), \tag{4.1}$$

where $P(k)$ has dimensions of k^{-3} or $(\text{length})^3$. The two point correlation functions of two random fields A and B in k-space can be written in terms of the dimensionless spectrum $\mathcal{P}_{AB}$ as

$$\langle A_{\mathbf{k}} B^*_{\mathbf{k}'}\rangle = \frac{2\pi^2}{k^3}\mathcal{P}_{AB}(k)\delta^{(3)}(\mathbf{k} - \mathbf{k}'). \tag{4.2}$$

If the magnetic fields are Gaussian, then their power spectrum determines all their statistical properties. We use the Fourier transformation convention

$$B_j(\mathbf{k}) = \int d^3x\, e^{i\mathbf{k}\cdot\mathbf{x}} B_j(\mathbf{x}), \qquad\qquad B_j(\mathbf{x}) = \frac{1}{(2\pi)^3}\int d^3k\, e^{-i\mathbf{k}\cdot\mathbf{x}} B_j(\mathbf{k})\ . \tag{4.3}$$

Also due to the stochastic (random) nature of the field, we take $\langle \mathbf{B}(\mathbf{x})\rangle = \mathbf{0}$. The magnetic field is divergence-free $\nabla\cdot\mathbf{B} = \mathbf{0} = \mathbf{k}\cdot\mathbf{B}(\mathbf{k})$. And, because the field is real, $B(\mathbf{k}) = B^*(-\mathbf{k})$. The Fourier space correlation function for a magnetic field, which as a vector field, can be written as [53]

$$\begin{aligned}\langle B_i(\mathbf{k}) B_j^*(\mathbf{k}')\rangle &= (2\pi)^3\delta^{(3)}(\mathbf{k}-\mathbf{k}')\mathcal{F}_{ij}^{(B)}(\mathbf{k}),\\ &= (2\pi)^3\delta^{(3)}(\mathbf{k}-\mathbf{k}')\big[S(k)P_{ij}(\hat{\mathbf{k}}) + A(k) i\epsilon_{ijm}\hat{k}_m\big],\end{aligned} \tag{4.4}$$

where $\mathcal{F}_{ij}^{(B)}(\mathbf{k}) = \mathcal{F}_{ji}^{(B)}(-\mathbf{k}) = \mathcal{F}_{ij}^{(B)*}(-\mathbf{k}) = \mathcal{F}_{ji}^{(B)*}(\mathbf{k})$, which indicates that the parity (mirror) symmetry is violated under parity transformation $\mathbf{k}\to-\mathbf{k}$ and $P_{ij}(\hat{\mathbf{k}}) = \left(\delta_{ij} - \hat{k}_i\hat{k}_j\right)$ is a projection operator onto the plane normal to $\mathbf{k}$. $k_iP_{ij} = 0$ indicates a divergence-free field. $S(k)$ and $A(k)$ are the power spectra of the symmetric and the helical parts, and can be taken to be power laws:

$$S(k) = \begin{cases} S_0\ k^{n_S}, & \text{for } k < k_D \\ 0 & \text{otherwise}\ , \end{cases} \tag{4.5}$$

and

$$A(k) = \begin{cases} A_0\ k^{n_A}, & \text{for } k < k_D \\ 0 & \text{otherwise}\ , \end{cases} \tag{4.6}$$

where S_0, A_0 are the normalisation constants, and n_S, n_A are the spectral indices of the symmetric and helical parts, respectively. k_D is a cutoff wavenumber because radiation viscosity leads to damping of small scale magnetic fields.

The mean helicity density of the magnetic field is given by

$$\mathcal{H}_B = \frac{1}{V}\int_V d\mathbf{x}^3\, \mathbf{A}(\mathbf{x})\cdot\mathbf{B}(\mathbf{x}) = \frac{1}{V}\int_V d\mathbf{x}^3\, (\mathrm{curl}^{-1}\mathbf{B})\cdot\mathbf{B}(\mathbf{x}) = \frac{1}{V}\int_V d\mathbf{x}^3\, \mathbf{A}(\mathbf{x})\cdot(\nabla\times\mathbf{A}(\mathbf{x})), \tag{4.7}$$

which is explained in section. 2.3.4. To calculate this quantity, we can learn from an analogy term called kinetic current helicity, which is given by

$$\frac{1}{V}\int_V d\mathbf{x}^3\, \mathbf{B}(\mathbf{x})\cdot(\nabla\times\mathbf{B}(\mathbf{x})), \tag{4.8}$$

which is gauge invariant. This form is in analogy to the expression of the kinetic helicity used in [53, 54, 55]. It describes the (electric) current helicity [56]. To calculate Eq.(4.8), we can replace $\frac{1}{V}\int_V d\mathbf{x}^3$ by an ensemble average $\langle ...\rangle$.

$$\begin{aligned}\langle(\nabla\times\mathbf{B}(\mathbf{x}))\cdot\mathbf{B}^*(\mathbf{x})\rangle &= \frac{1}{(2\pi)^6}\int d^3k\int d^3k'\,e^{i(\mathbf{k}'-\mathbf{k})\cdot\mathbf{x}}(2\pi)^3\delta^{(3)}(\mathbf{k}-\mathbf{k}')A(k)\left(\frac{2k_2^2}{k}+\frac{2k_3^2}{k}+\frac{2k_1^2}{k}\right)\\ &= \frac{1}{(2\pi)^3}\int d^3k\,2kA(k)\\ &= \frac{1}{(2\pi)^3}\int 4\pi k^2dk\,2kA(k). \end{aligned}\tag{4.9}$$

We find that $\nabla\times\mathbf{B}\sim k\mathbf{B}$, $\mathbf{B}=\nabla\times\mathbf{A}\sim k\mathbf{A}$, thus $\mathbf{A}\sim\mathbf{B}/k$. In analogy, the asymmetric power spectrum $A(k)$ can be related to helicity density Eq.(4.7) by

$$\begin{aligned}\mathcal{H}_B &= \frac{1}{(2\pi)^3}\int 4\pi k^2dk\,2k\frac{A(k)}{k^2}\\ &= \frac{2}{(2\pi)^3}\int_0^{k_D}4\pi kdkA(k)\\ &= \frac{8\pi}{(2\pi)^3}\frac{A_0(k_D)^{n_A+2}}{(n_A+2)}. \end{aligned}\tag{4.10}$$

One can define the averaged magnetic field energy density ${B_\lambda}^2\equiv\langle\mathbf{B}(\mathbf{x})\cdot\mathbf{B}(\mathbf{x})\rangle|_\lambda$ smoothed over a comoving scale λ by convolving it with a filter function, $\hat{f}_\lambda(k)=\exp(-\lambda^2k^2/2)$, as

$$B_\lambda^2 = \frac{1}{(2\pi)^3}\int d^3k\,S(k)\hat{f}_\lambda(k)^2=\frac{2S_0}{(2\pi)^2}\frac{1}{\lambda^{n_S+3}}\Gamma\left(\frac{n_S+3}{2}\right).\tag{4.11}$$

Subsequently, S_0 can be written in terms of B_λ^2 and $k_\lambda=2\pi/\lambda$ as

$$\begin{aligned}S_0^2 &= \frac{1}{4}\left[\frac{(2\pi)^2\lambda^{n_S+3}B_\lambda^2}{\Gamma\left(\frac{n_S+3}{2}\right)}\right]^2=\frac{1}{4}\left[\frac{(2\pi)^{n_S+5}B_\lambda^2}{\Gamma\left(\frac{n_S+3}{2}\right)k_\lambda^{n_S+3}}\right]^2\\ &= \frac{1}{4}\left[\frac{(2\pi)^{n_S+2}B_\lambda^2}{\Gamma\left(\frac{n_S+3}{2}\right)}\right]^2\frac{2\pi^6}{k_\lambda^{2n_S+6}}\,. \end{aligned}\tag{4.12}$$

Avoiding the infrared divergence at $k\to0$ when integrating the magnetic field energy density and helicity spectra requires $n_S>-3$ and $n_A>-4$, respectively.

On small scales, the interaction between plasma and magnetic field cannot be ignored. In plasma, ions are affected by the forces provided by magnetic fields, then oscillate to create a MHD wave called Alfvén wave. We assume that magnetic field damping is due to the damping of Alfvén waves by the photon viscosity. We model the magnetic field damping by introducing an ultraviolet cut-off wavenumber $k_D=2\pi/\lambda_D$[19]. The damping scale can be expressed in terms of the amplitude and the spectral index of the PMF spectrum as

[57, 58, 59]

$$\frac{k_D}{\mathrm{Mpc}^{-1}} = \left[5.5\times 10^4 h\Big(\frac{B_\lambda}{nG}\Big)^{-2}\Big(\frac{2\pi}{\lambda/\mathrm{Mpc}}\Big)^{n_B+3}\frac{\Omega_b h^2}{0.022}\right]^{\frac{1}{n_S+5}}, \tag{4.13}$$

where Ω_b is the baryon density fraction and h is the reduced Hubble constant, $H_0 = 100\,h\,\mathrm{km/(s\,Mpc)}$, and $\lambda_D \ll \lambda_S$. The primordial plasma is a perfect conductor on all scales larger than the Silk damping wavelength λ_S (the thickness of the last scattering surface) set by photon and neutrino diffusion. In what follows, we will take $\lambda = 1\,\mathrm{Mpc}$ when working with B_λ.

The averaged magnetic field energy density $\mathcal{E}_B$ (ρ_B) is given by

$$\begin{aligned}\frac{1}{2}\langle B_i(\mathbf{x})B_i^*(\mathbf{x})\rangle &= \frac{1}{2}\frac{1}{(2\pi)^3}\int d^3k\, e^{-i\mathbf{k}\cdot\mathbf{x}}\frac{1}{(2\pi)^3}\int d^3k'\, e^{+i\mathbf{k}'\cdot\mathbf{x}}\langle B_i(\mathbf{k})B_i^*(\mathbf{k}')\rangle \\ &= \frac{2}{2}\frac{1}{(2\pi)^6}\int d^3k\int d^3k'\, e^{i(\mathbf{k}'-\mathbf{k})\cdot\mathbf{x}}(2\pi)^3\delta^{(3)}(\mathbf{k}-\mathbf{k}')S(k) \\ &= \frac{1}{(2\pi)^3}\int 4\pi k^2 dk\, S(k). \end{aligned}\tag{4.14}$$

It can be expressed in terms of B_λ as

$$\begin{aligned}\mathcal{E}_B &= \frac{1}{2}\langle|\mathbf{B}(\mathbf{x})|^2\rangle = \frac{4\pi}{(2\pi)^3}\int_0^{k_D} k^2 dk S(k) \\ &= \frac{4\pi}{(2\pi)^3}\frac{S_0(k_D)^{n_S+3}}{(n_S+3)} \\ &= \frac{B_\lambda^2(k_D\lambda)^{n_S+3}}{(n_S+3)\Gamma\left(\frac{n_S+3}{2}\right)}. \end{aligned}\tag{4.15}$$

The magnetic field correlation length is defined as

$$\xi_B = \frac{1}{\mathcal{E}_B}\int_0^{k_D} 4\pi k dk S(k) = \frac{n_S+3}{(n_S+2)k_D}. \tag{4.16}$$

One can also define the effective magnetic field amplitude B_{eff}, related to the energy density and power spectrum via

$$B_{\mathrm{eff}} \equiv (2\mathcal{E}_B)^{1/2} = \frac{B_\lambda(k_D\lambda)^{\frac{n_S+3}{2}}}{\sqrt{\Gamma\left(\frac{n_S+5}{2}\right)}}. \tag{4.17}$$

When $n_S = -3$ (scale invariant spectrum), $B_{\mathrm{eff}} = B_\lambda$ for all λ.

The induced electromagnetic tensor in covariant form is

$$-T_{(ij)EM} = \frac{1}{a^2 4\pi}\left(E_iE_j + B_iB_j - \frac{1}{2}\delta_{ij}(E^2+B^2)\right).$$

Since $E \sim 0$ in perfectly conducting plasma. In Fourier space, the electromagnetic tensor is given by the convolution of the magnetic field

$$T_{B(ij)}(\mathbf{k}) = \frac{1}{4\pi a^4 (2\pi)^3} \times \int d^3q \left[\frac{1}{2}\delta_{ij} B_l(\mathbf{q}) B^l(\mathbf{k}-\mathbf{q}) - B_i(\mathbf{k}) B_j(\mathbf{k}-\mathbf{q})\right]. \tag{4.18}$$

In what follows, we will compute the two parts: $T^{(1)}_{B(ij)}(\mathbf{k}) = \frac{1}{4\pi a^4(2\pi)^3} \times \int d^3q\, \frac{1}{2}\delta_{ij} B_l(\mathbf{q}) B^l(\mathbf{k}-\mathbf{q})$ and $T^{(2)}_{B(ij)}(\mathbf{k}) = \frac{1}{4\pi a^4(2\pi)^3} \times \int d^3q\, B_i(\mathbf{k}) B_j(\mathbf{k}-\mathbf{q})$, separately.

4.1.1 The Realizability Condition

If the magnetic diffusivity is very small, and the conductivity of the plasma in the early universe is very high, the magnetic helicity is conserved. Which leads to the theorem [60]:

$$L_- |\mathbf{B}(\mathbf{x})|^{\mathbf{2}} \leq (\mathrm{curl}^{-\mathbf{1}}\mathbf{B}) \cdot \mathbf{B} \leq \mathbf{L}_+ |\mathbf{B}(\mathbf{x})|^{\mathbf{2}}, \tag{4.19}$$

where L_- and L_+ denote the smallest and the largest eigenvalues of the $(\mathrm{curl}^{-1}\mathbf{B})$, $L_- < 0 < L_+$ and the B field is divergence-free. Equation (4.19) can be simplified as

$$\frac{|(\mathrm{curl}^{-1}\mathbf{B}) \cdot \mathbf{B}|}{|L|} \leq |\mathbf{B}(\mathbf{x})|^{\mathbf{2}}, \tag{4.20}$$

where L is the larger magnitude between L_- and L_+. Considering the ensemble average, Eq. (4.20) becomes

$$\frac{|\mathcal{H}_B|}{|L|} = \frac{|\langle(\mathrm{curl}^{-1}\mathbf{B}) \cdot \mathbf{B}\rangle|}{|L|} \leq \langle |\mathbf{B}(\mathbf{x})|^{\mathbf{2}} \rangle = \mathbf{2}\mathcal{E}_{\mathbf{B}}. \tag{4.21}$$

Assuming that L has an order of the magnetic field correlation length $|L| \leq \xi_B$, we can obtain the realizability condition

$$|\mathcal{H}_B| \leq 2\xi_B \mathcal{E}_B. \tag{4.22}$$

Combing equations (4.15), (4.10), (4.16), we obtain

$$\frac{|A_0 k_D^{n_A+2}|}{|n_A+2|} \leq \frac{|S_0 k_D^{n_S+2}|}{|n_S+2|}. \tag{4.23}$$

Thus, to satisfy the realizability condition [55, 60, 61], which imposes a constraint on the power spectra, namely, $|A(k)| \leq |S(k)|$, which leads to $n_S \leq n_A$. In the limit of maximal helicity, $|S(k)| = |A(k)|$, $S_0 = |A_0|$ and $n_A = n_S$.

4.1.2 The tensor decomposition

Any tenosr T_{ij} can be decomposed into a trace part T and a traceless part consisting of three pieces, $T^{\parallel}_{ij}, T^{\perp}_{ij}$, and T^{T}_{ij}:

$$T_{ij} = \frac{\delta_{ij}}{3}T + T^{\parallel}_{ij} + T^{\perp}_{ij} + T^{T}_{ij}, \tag{4.24}$$

where $T \equiv T_{ii}$; $T^{\parallel}_{ij}$ can be constructed by some scalar field A and $T^{\perp}_{ij}$ can be wirtten in terms of some divergenceless vector $\vec{V}$ ($\partial_i V_i = 0$) as

$$\begin{aligned} T^{\parallel}_{ij} &= \left(\partial_i\partial_j - \frac{1}{3}\delta_{ij}\nabla^2\right)A\,, \\ T^{\perp}_{ij} &= \partial_i V_j + \partial_j V_i\,. \end{aligned} \tag{4.25}$$

The divergences of $T^{\parallel}_{ij}$, and $T^{\perp}_{ij}$ are longitudinal and transverse, respectively, and T^{T}_{ij} is transverse,

$$\epsilon_{ijk}\partial_j\partial_l T^{\parallel}_{lk} = 0\,, \qquad \partial_i\partial_j T^{\perp}_{ij} = 0\,, \qquad \partial_i T^{T}_{ij} = 0\,. \tag{4.26}$$

Applying this rule to the stress tensor $T_{B(ij)}$ in Eq.(4.18), we can write the magnetic field energy density Δ_B, along with the scalar, vector and tensor modes of the spatial components as

$$\frac{T_{B(ij)}}{\rho_\gamma} = \frac{\delta_{ij}}{3}\Delta_B + \Pi^{(0)}_B(\hat{k}_i\hat{k}_j - \frac{1}{3}\delta_{ij}) + \Pi^{(V)}_{B(ij)} + \Pi^{(T)}_{B(ij)}, \tag{4.27}$$

where

$$\Delta_B = \frac{1}{\rho_\gamma}T_{B(ii)} = \frac{1}{\rho_\gamma}\delta_{ij}T_{B(ij)}\,, \tag{4.28}$$

$$\Pi^{(0)}_B = \frac{1}{\rho_\gamma}\frac{2}{3}(\hat{k}_i\hat{k}_j - \frac{1}{3}\delta_{ij})T_{B(ij)}. \tag{4.29}$$

The vector component is

$$\begin{aligned} \Pi^{(V)}_{B(ij)} &= \frac{1}{\rho_\gamma}(P_{im}\hat{k}_j\hat{k}_n + P_{jn}\hat{k}_i\hat{k}_m)T_{B(mn)}\,, \\ L^{(V)}_i = k\Pi^{(V)}_i &= k\Pi^{(V)}_{ij}\hat{k}_j = \frac{1}{\rho_\gamma}kP_{im}\hat{k}_n T_{B(mn)}\,. \end{aligned} \tag{4.30}$$

In the above, $L^{(V)}_i$ is the Lorentz force vector, which can source the vorticity perturbations. We shall often use simple properties like

$$P_{ij} = \delta_{ij} - \widehat{k}_i\widehat{k}_j, P_{ii} = P_{ij}P_{ij} = 2, P_{ij}P_{im} = P_{jm}, P_{ij}\widehat{k}_i = 0. \tag{4.31}$$

The tensor component is

$$\Pi^{(T)}_{B(ij)} = \frac{1}{\rho_\gamma}(P_{im}P_{jn} - \frac{1}{2}P_{ij}P_{mn})T_{B(mn)}, \tag{4.32}$$

which sources the gravitational wave perturbations.

Following the conventions in [55, 62, 63] when dealing with the perturbations of the metric (3.8,3.11), the vector and tensor modes can be further decomposed into the normal modes, which can be written as

$$\begin{aligned}
\mathbf{e}^{(\pm1)}_i &= -\frac{i}{\sqrt{2}}(\hat{\mathbf{e}}^1_i \pm i\hat{\mathbf{e}}^2_i)\,, \\
\mathbf{e}^{(\pm1)}_{ij} &= -\frac{1}{2\sqrt{2}}[\hat{k}_j(\hat{\mathbf{e}}^1_i \pm i\hat{\mathbf{e}}^2_i) + \hat{k}_i(\hat{\mathbf{e}}^1_j \pm i\hat{\mathbf{e}}^2_j)]\,, \\
\mathbf{e}^{(\pm2)}_{ij} &= -\sqrt{\frac{3}{8}}(\hat{\mathbf{e}}^1 \pm i\hat{\mathbf{e}}^2)_i(\hat{\mathbf{e}}^1 \pm i\hat{\mathbf{e}}^2)_j.
\end{aligned} \tag{4.33}$$

where they satisfy $\mathbf{e}^{(\pm2)}_{ij}\mathbf{e}^{(\mp2)}_{ij} = 3/2$, $\delta_{ij}\mathbf{e}^{(\pm2)}_{ij} = 0$, $\widehat{k}_i\mathbf{e}^{(\pm2)}_{ij} = 0$, $\mathbf{e}^{(\pm1)}_{ij}\mathbf{e}^{(\mp1)}_{ij} = 1/2$. In this basis, the tensor and vector anisotropic stresses can be expressed as

$$\Pi^{(V)}_{B(ij)}(\vec{k}) = \pi^{(+1)}_B(\vec{k})\mathbf{e}^{(+1)}_{ij} + \pi^{(-1)}_B(\vec{k})\mathbf{e}^{(-1)}_{ij}, \tag{4.34}$$

$$\Pi^{(T)}_{B(ij)}(\vec{k}) = \pi^{(+2)}_B(\vec{k})\mathbf{e}^{(+2)}_{ij} + \pi^{(-2)}_B(\vec{k})\mathbf{e}^{(-2)}_{ij}. \tag{4.35}$$

To obtain the two point correlation, we calculate the following terms

$$\begin{aligned}
\pi^{(+1)}_B\mathbf{e}^{(+1)}_{cd}\mathbf{e}^{(-1)}_{cd} = \frac{1}{2}\pi^{(+1)}_B &= \Pi^{(V)}_{B(cd)}\mathbf{e}^{(-1)}_{cd} \\
\frac{1}{2}\pi^{(+1)*}_B &= \Pi^{(V)*}_{B(ab)}\mathbf{e}^{(+1)}_{ab} \\
\frac{1}{2}\pi^{(-1)}_B &= \Pi^{(V)}_{B(ab)}\mathbf{e}^{(+1)}_{ab} \\
\frac{1}{2}\pi^{(-1)*}_B &= \Pi^{(V)*}_{B(cd)}\mathbf{e}^{(-1)}_{cd}
\end{aligned} \tag{4.36}$$

Hence, the two point correlation can be written as

$$\begin{aligned}
\langle\Pi^{(V)}_{B(ab)}(\mathbf{k})\Pi^{(V)*}_{B(ab)}(\mathbf{k}')\rangle &= (\mathbf{e}^{(+1)}_{ab}\mathbf{e}^{(-1)}_{ab}) \times \langle\pi^{(+1)}_B(\vec{k})\pi^{(+1)*}_B(\vec{k}') + \pi^{(-1)}_B(\vec{k})\pi^{(-1)*}_B(\vec{k}')\rangle \\
&= \frac{1}{2}\langle\pi^{(+1)}_B(\vec{k})\pi^{(+1)*}_B(\vec{k}') + \pi^{(-1)}_B(\vec{k})\pi^{(-1)*}_B(\vec{k}')\rangle
\end{aligned} \tag{4.37}$$

Hence, we obtain

$$\frac{1}{4}\langle\pi_B^{(+1)}(\mathbf{k})\pi_B^{(+1)*}(\mathbf{k}')\rangle = \mathbf{e}_{ab}^{(+1)}\mathbf{e}_{cd}^{(-1)}\langle\Pi_{B(cd)}^{(V)}(\mathbf{k})\Pi_{B(ab)}^{(V)*}(\mathbf{k}')\rangle = (f^V(k) - g^V(k))\delta^{(3)}(\mathbf{k}-\mathbf{k}')$$
$$\frac{1}{4}\langle\pi_B^{(-1)}(\mathbf{k})\pi_B^{(-1)*}(\mathbf{k}')\rangle = \mathbf{e}_{ab}^{(+1)}\mathbf{e}_{cd}^{(-1)}\langle\Pi_{B(ab)}^{(V)}(\mathbf{k})\Pi_{B(cd)}^{(V)*}(\mathbf{k}')\rangle = (f^V(k) + g^V(k))\delta^{(3)}(\mathbf{k}-\mathbf{k}') \tag{4.38}$$

Considering the symmetry properties of $\langle\Pi_{B(ab)}^{(V)}\Pi_{B(cd)}^{(V)*}\rangle$, f^V is the symmetric part under the exchange of ab with cd in $(\langle\Pi_{B(cd)}^{(V)}\Pi_{B(ab)}^{(V)*}\rangle)$, while g^V is the anti-symmetric part under this permutation.

$$\begin{aligned}\frac{1}{4}\langle\pi_B^{(+1)}\pi_B^{(+1)*} + \pi_B^{(-1)}\pi_B^{(-1)*}\rangle &= 2f^V(k)\delta^{(3)}(\mathbf{k}-\mathbf{k}')\\ \frac{1}{4}\langle\pi_B^{(+1)}\pi_B^{(+1)*} - \pi_B^{(-1)}\pi_B^{(-1)*}\rangle &= -2g^V(k)\delta^{(3)}(\mathbf{k}-\mathbf{k}')\end{aligned} \tag{4.39}$$

We obtain these two functions by doing a vector projection

$$\begin{aligned}\langle\pi_B^{(+1)}(\mathbf{k})\pi_B^{(+1)*}(\mathbf{k}') + \pi_B^{(-1)}(\mathbf{k})\pi_B^{(-1)*}(\mathbf{k}')\rangle &= 8f^V(k)\delta^{(3)}(\mathbf{k}-\mathbf{k}') = 2\langle\Pi_{B(ab)}^{(V)}(\mathbf{k})\Pi_{B(ab)}^{(V)*}(\mathbf{k}')\rangle\\ \langle\pi_B^{(+1)}(\mathbf{k})\pi_B^{(+1)*}(\mathbf{k}') - \Pi_B^{(-1)}(\mathbf{k})\pi_B^{(-1)*}(\mathbf{k}')\rangle &= -8g^V(k)\delta^{(3)}(\mathbf{k}-\mathbf{k}').\end{aligned} \tag{4.40}$$

To obtain the two point correlation for tensor modes, we calculate the following terms

$$\begin{aligned}\pi_B^{(+2)}\mathbf{e}_{cd}^{(+2)}\mathbf{e}_{cd}^{(-2)} = \frac{3}{2}\pi_B^{(+2)} &= \Pi_{B(cd)}^{(T)}\mathbf{e}_{cd}^{(-2)}\\ \frac{3}{2}\pi_B^{(+2)*} &= \Pi_{B(ab)}^{(T)*}\mathbf{e}_{ab}^{(+2)}\\ \frac{3}{2}\pi_B^{(-2)} &= \Pi_{B(ab)}^{(T)}\mathbf{e}_{ab}^{(+2)}\\ \frac{3}{2}\pi_B^{(-2)*} &= \Pi_{B(cd)}^{(T)*}\mathbf{e}_{cd}^{(-2)}.\end{aligned} \tag{4.41}$$

Hence, the two point correlation can be written as

$$\begin{aligned}\langle\Pi_{B(ab)}^{(T)}(\mathbf{k})\Pi_{B(ab)}^{(T)*}(\mathbf{k}')\rangle &= (\mathbf{e}_{ab}^{(+2)}\mathbf{e}_{ab}^{(-2)}) \times \langle\pi_B^{(+2)}(\vec{k})\pi_B^{(+2)*}(\vec{k}') + \pi_B^{(-2)}(\vec{k})\pi_B^{(-2)*}(\vec{k}')\rangle\\ &= \frac{3}{2}\langle\pi_B^{(+2)}(\vec{k})\pi_B^{(+2)*}(\vec{k}') + \pi_B^{(-2)}(\vec{k})\pi_B^{(-2)*}(\vec{k}')\rangle.\end{aligned} \tag{4.42}$$

Thus,

$$\begin{aligned}\frac{9}{4}\langle\pi_B^{(+2)}(\mathbf{k})\pi_B^{(+2)*}(\mathbf{k}')\rangle &= \mathbf{e}_{ab}^{(+2)}(bk)\mathbf{e}_{cd}^{(-2)}(\mathbf{k}')\langle\Pi_{B(cd)}^{(T)}(\mathbf{k})\Pi_{B(ab)}^{(T)*}(\mathbf{k}')\rangle\\ &= (f^T(k) - g^T(k))\delta^{(3)}(\mathbf{k}-\mathbf{k}')\\ \frac{9}{4}\langle\pi_B^{(-2)}(\mathbf{k})\pi_B^{(-2)*}(\mathbf{k}')\rangle &= \mathbf{e}_{ab}^{(+2)}\mathbf{e}_{cd}^{(-2)}\langle\Pi_{B(ab)}^{(T)}(\mathbf{k})\Pi_{B(cd)}^{(T)*}(\mathbf{k}')\rangle\\ &= (f^T(k) + g^T(k))\delta^{(3)}(\mathbf{k}-\mathbf{k}')\end{aligned} \tag{4.43}$$

Simplifying it, we obtain

$$\begin{aligned}\frac{9}{4}\langle\pi_B^{(+2)}(\mathbf{k})\pi_B^{(+2)*}(\mathbf{k}')+\pi_B^{(-2)}(\mathbf{k})\pi_B^{(-2)*}(\mathbf{k}')\rangle &= 2f^T(k)\delta^{(3)}(\mathbf{k}-\mathbf{k}')\\ \frac{9}{4}\langle\pi_B^{(+2)}(\mathbf{k})\pi_B^{(+2)*}(\mathbf{k}')-\pi_B^{(-2)}(\mathbf{k})\Pi_B^{(-2)*}(\mathbf{k}')\rangle &= -2g^T(k)\delta^{(3)}(\mathbf{k}-\mathbf{k}'). \end{aligned} \quad (4.44)$$

Rewriting it, we get

$$\begin{aligned}\langle\pi_B^{(+2)}(\mathbf{k})\pi_B^{(+2)*}(\mathbf{k}')+\pi_B^{(-2)}(\mathbf{k})\pi_B^{(-2)*}(\mathbf{k}')\rangle &= \frac{8}{9}f^T(k)\delta^{(3)}(\mathbf{k}-\mathbf{k}')=\frac{2}{3}\langle\Pi_{B(ab)}^{(T)}(\mathbf{k})\Pi_{B(ab)}^{(T)*}(\mathbf{k}')\rangle\\ \langle\pi_B^{(+2)}(\mathbf{k})\pi_B^{(+2)*}(\mathbf{k}')-\pi_B^{(-2)}(\mathbf{k})\pi_B^{(-2)*}(\mathbf{k}')\rangle &= -\frac{8}{9}g^T(k)\delta^{(3)}(\mathbf{k}-\mathbf{k}'). \end{aligned} \quad (4.45)$$

4.1.3 Calculations on the two-point correlation functions

To calculate all the two point correlation functions, the first step is to evaluate the two point correlator of the magnetic field stress energy tensor defined in Equation (4.18):

$$\begin{aligned}\langle T_{B(ij)}(\mathbf{k})T^*_{B(lm)}(\mathbf{k}')\rangle &= \frac{1}{(4\pi)^2}\frac{1}{(2\pi)^6a^8}\int d^3p\int d^3q\,\langle B_i(\mathbf{p})B_j(\mathbf{k}-\mathbf{p})B_l(-\mathbf{q})B_m(\mathbf{q}-\mathbf{k}')\rangle\\ &\quad +\cdots\delta_{ij}+\cdots\delta_{lm}\ , \end{aligned} \quad (4.46)$$

The terms proportional to δ_{ij} and δ_{lm} are not shown, because they are not contributing to the final results for the tensor and vector perturbation $\langle\Pi_{ij}\Pi_{lm}\rangle$ after being projected out. Since the magnetic fields are Gaussian, we can apply Wick's theorem $\langle ABCD\rangle = \langle AB\rangle\langle CD\rangle + \langle AC\rangle\langle BD\rangle + \langle AD\rangle\langle BC\rangle$ to the first term on the right hand side. Then, the four-point correlators can be written in terms of the two-point ones:

$$\begin{aligned}\langle B_i(\mathbf{k}_i)B_j(\mathbf{k}_j)B_l(\mathbf{k}_l)B_m(\mathbf{k}_m)\rangle &= \langle B_i(\mathbf{k}_i)B_j(\mathbf{k}_j)\rangle\langle B_l(\mathbf{k}_l)B_m(\mathbf{k}_m)\rangle\\ &+ \langle B_i(\mathbf{k}_i)B_l(\mathbf{k}_l)\rangle\langle B_j(\mathbf{k}_j)B_m(\mathbf{k}_m)\rangle\\ &+ \langle B_i(\mathbf{k}_i)B_m(\mathbf{k}_m)\rangle\langle B_j(\mathbf{k}_j)B_l(\mathbf{k}_l)\rangle\ . \end{aligned} \quad (4.47)$$

Using this in Equation (4.46), after a long calculation, we can write it as

$$\begin{aligned}
\langle T^{(2)}_{B(ij)}(\mathbf{k}) T^{(2)*}_{B(lm)}(\mathbf{k}')\rangle &= \frac{\delta(\mathbf{k}-\mathbf{k}')}{(4\pi)^2 a^8}\int d^3p\,(\; S(p)S(|\mathbf{k}-\mathbf{p}|)[(\delta_{il}-\hat{p}_i\hat{p}_l)(\delta_{jm} \\
&\quad -(\widehat{\mathbf{k}-\mathbf{p}})_j(\widehat{\mathbf{k}-\mathbf{p}})_m)+(\delta_{im}-\hat{p}_i\hat{p}_m)(\delta_{jl}-(\widehat{\mathbf{k}-\mathbf{p}})_j(\widehat{\mathbf{k}-\mathbf{p}})_l)] \\
&\quad -A(p)A(|\mathbf{k}-\mathbf{p}|)[\epsilon_{ilt}\epsilon_{jmr}\hat{p}_t(\widehat{\mathbf{k}-\mathbf{p}})_r+\epsilon_{imf}\epsilon_{jlg}\hat{p}_f(\widehat{\mathbf{k}-\mathbf{p}})_g] \\
&\quad +iS(p)A(|\mathbf{k}-\mathbf{p}|)[\epsilon_{jmr}(\delta_{il}-\hat{p}_i\hat{p}_l)(\widehat{\mathbf{k}-\mathbf{p}})_r \\
&\quad +\epsilon_{jlg}(\delta_{im}-\hat{p}_i\hat{p}_m)(\widehat{\mathbf{k}-\mathbf{p}})_g] \\
&\quad +iA(p)S(|\mathbf{k}-\mathbf{p}|)[\epsilon_{ilt}(\delta_{jm}-(\widehat{\mathbf{k}-\mathbf{p}})_j(\widehat{\mathbf{k}-\mathbf{p}})_m)\hat{p}_t \\
&\quad +\epsilon_{imf}(\delta_{jl}-(\widehat{\mathbf{k}-\mathbf{p}})_j(\widehat{\mathbf{k}-\mathbf{p}})_l)\hat{p}_f]\;\} \\
&\quad +\cdots\delta_{ij}+\cdots\delta_{lm}\;. \qquad (4.48)
\end{aligned}$$

4.1.4 The scalar projection

The auto-correlation function of the magnetic energy density contrast (Eq. 4.28) is

$$\begin{aligned}
\langle \Delta_B(\mathbf{k})\Delta_B^*(\mathbf{k}')\rangle &= \frac{1}{4\rho_\gamma^2}\delta_{ij}\delta_{lm}\langle T^{(2)}_{B(ij)}(\mathbf{k})T^{(2)*}_{B(lm)}(\mathbf{k}')\rangle \\
&= \frac{1}{4\rho_\gamma^2(4\pi)^2a^8}\delta^{(3)}(\mathbf{k}-\mathbf{k}')\int d^3p\;[\; S(p)S(|\mathbf{k}-\mathbf{p}|)2(1+\mu^2) \\
&\quad -A(p)A(|\mathbf{k}-\mathbf{p}|)4\mu\;] \\
&= (2\pi)^3\frac{2\pi^2}{k^3}\delta^{(3)}(\mathbf{k}-\mathbf{k}')\mathcal{P}_{\Delta_B\Delta_B}(k), \qquad (4.49)
\end{aligned}$$

where

$$\begin{aligned}
\mathcal{P}_{\Delta_B\Delta_B}(k) = \frac{1}{4}\frac{2k^3}{(\rho_{\gamma,0})^2 4(2\pi)^2(2\pi)^5}\int d^3p \\
\times[\; S(p)S(|\mathbf{k}-\mathbf{p}|)2(1+\mu^2)-A(p)A(|\mathbf{k}-\mathbf{p}|)4\mu\;]\,. \qquad (4.50)
\end{aligned}$$

where $\beta=\hat{\mathbf{k}}\cdot(\widehat{\mathbf{k}-\mathbf{p}})$, $\gamma=\hat{\mathbf{k}}\cdot\hat{\mathbf{p}}$ and $\mu=\hat{\mathbf{p}}\cdot(\widehat{\mathbf{k}-\mathbf{p}})$. We can express the power spectrum $\mathcal{P}_{\Delta_B\Delta_B}(k)$ in terms of symbols $z=p/k$ and $x=\gamma$. Then it can be split into an integral over z from 0 to $\frac{k_D}{k}$, and an integral over $x=\gamma$ from -1 to 1. This follows from $d^3p=2\pi p^2dpdx=2\pi k^3z^2dzdx$. Thus, $\beta=(1-zx)/\sqrt{1+z^2-2zx}$ and $\mu=(x-z)/\sqrt{1+z^2-2zx}$. We obtain

$$\begin{aligned}
\mathcal{P}_{\Delta_B\Delta_B}(k) = \frac{1}{4}\frac{S_0^2}{(\rho_{\gamma,0})^2(2\pi)^6}k^{2n_s+6}\int dz z^{n_s+2} \\
\times\int dx\left(1-2zx+z^2\right)^{\frac{n_s-2}{2}}(1+x^2-4zx+2z^2) \\
-\frac{1}{2}\frac{A_0^2}{(\rho_{\gamma,0})^2(2\pi)^6}k^{2n_A+6}\int dz z^{n_A+2}\times\int dx\left(1-2zx+z^2\right)^{\frac{n_A-1}{2}}(x-z), \qquad (4.51)
\end{aligned}$$

The auto-correlation function of $\Pi_B^{(0)}$ (see Eq. (4.29)) is

$$\begin{aligned}
\langle \Pi_B^{(0)}(\mathbf{k})\Pi_B^{(0)*}(\mathbf{k}')\rangle &= (\frac{3}{2}\frac{1}{\rho_\gamma})^2(\hat{k}_i\hat{k}_j-\frac{1}{3}\delta_{ij})(\hat{k}_l\hat{k}_m-\frac{1}{3}\delta_{lm})\langle T^{(2)}_{B(ij)}(\mathbf{k})T^{(2)*}_{B(lm)}(\mathbf{k}')\rangle \\
&= \frac{9}{4\rho_\gamma^2(4\pi)^2a^8}\delta^{(3)}(\mathbf{k}-\mathbf{k}')\int d^3p \\
&\quad\times[\, S(p)S(|\mathbf{k}-\mathbf{p}|)\frac{2}{9}(9\beta^2\gamma^2-6\beta\mu\gamma-3\beta^2+\mu^2-3\gamma^2+4) \\
&\qquad -A(p)A(|\mathbf{k}-\mathbf{p}|)\frac{2}{9}(6\gamma\beta-4\mu)\,] \\
&= (2\pi)^3\frac{2\pi^2}{k^3}\delta^{(3)}(\mathbf{k}-\mathbf{k}')\mathcal{P}_{\Pi_B^{(0)}\Pi_B^{(0)}}(k), \qquad (4.52)
\end{aligned}$$

where

$$\begin{aligned}
\mathcal{P}_{\Pi_B^{(0)}\Pi_B^{(0)}}(k) &= \frac{9}{4}\times\frac{2}{9}\frac{2k^3}{(\rho_{\gamma,0})^2 4(2\pi)^2(2\pi)^5}\int d^3p\times[\, S(p)S(|\mathbf{k}-\mathbf{p}|) \\
&\quad (9\beta^2\gamma^2-6\beta\mu\gamma-3\beta^2+\mu^2-3\gamma^2+4)-A(p)A(|\mathbf{k}-\mathbf{p}|)(6\gamma\beta-4\mu)\,]\,. \qquad (4.53)
\end{aligned}$$

Rewriting it in terms of x, z gives

$$\begin{aligned}
\mathcal{P}_{\Pi_B^{(0)}\Pi_B^{(0)}}(k) &= \frac{1}{4}\frac{S_0^2}{(\rho_{\gamma,0})^2(2\pi)^6}k^{2n_s+6}\int dz z^{n_s+2} \\
&\times\int dx\left(1-2zx+z^2\right)^{\frac{n_s-2}{2}}(9x^4z^2-6zx^3+(-12z^2+1)x^2+2zx+5z^2+1) \\
&-\frac{1}{4}\frac{A_0^2}{(\rho_{\gamma,0})^2(2\pi)^6}k^{2n_A+6}\int dz z^{n_A+2}\times\int dx\left(1-2zx+z^2\right)^{\frac{n_A-1}{2}}(-6zx^2+2x+4z). \qquad (4.54)
\end{aligned}$$

The cross correlation function of $\Pi_B^{(0)}$ and Δ_B is

$$\begin{aligned}
\langle \Delta_B(\mathbf{k})\Pi_B^{(0)*}(\mathbf{k}')\rangle &= \frac{3}{2}\frac{1}{\rho_\gamma}\frac{1}{2\rho_\gamma}\delta_{ij}(\hat{k}_l\hat{k}_m-\frac{1}{3}\delta_{lm})\langle T^{(2)}_{B(ij)}(\mathbf{k})T^{(2)*}_{B(lm)}(\mathbf{k}')\rangle \\
&= \frac{3}{4\rho_\gamma^2(4\pi)^2a^8}\delta^{(3)}(\mathbf{k}-\mathbf{k}')\int d^3p\,[\, S(p)S(|\mathbf{k}-\mathbf{p}|)\frac{2}{3}(2\mu^2-1-3\mu\beta\gamma) \\
&\qquad -A(p)A(|\mathbf{k}-\mathbf{p}|)\frac{2}{3}(-3\gamma\beta+\mu)\,] \\
&= (2\pi)^3\frac{2\pi^2}{k^3}\delta^{(3)}(\mathbf{k}-\mathbf{k}')\mathcal{P}_{\Delta_B\Pi_B^{(0)}}(k), \qquad (4.55)
\end{aligned}$$

where

$$\mathcal{P}_{\Delta_B\Pi_B^{(0)}}(k) = \frac{3}{4}\times\frac{2}{3}\frac{2k^3}{(\rho_{\gamma,0})^2 4(2\pi)^2(2\pi)^5}\int d^3p \\ \times[\ S(p)S(|\mathbf{k}-\mathbf{p}|)(2\mu^2-1-3\mu\beta\gamma)+A(p)A(|\mathbf{k}-\mathbf{p}|)(3\gamma\beta-\mu)\ ]\,. \tag{4.56}$$

Rewriting it in terms of x and z gives

$$\mathcal{P}_{\Delta_B\Pi_B^{(0)}}(k) = \frac{1}{4}\frac{S_0^2}{(\rho_{\gamma,0})^2(2\pi)^6}k^{2n_s+6}\int dz z^{n_s+2} \\ \times\int dx\left(1-2zx+z^2\right)^{\frac{n_s-2}{2}}(3zx^3+(-3z^2-1)x^2+zx+z^2-1), \\ +\frac{1}{4}\frac{A_0^2}{(\rho_{\gamma,0})^2(2\pi)^6}k^{2n_A+6}\int dz z^{n_A+2}\times\int dx\left(1-2zx+z^2\right)^{\frac{n_A-1}{2}}(-3zx^2+2x+z). \tag{4.57}$$

4.1.5 The vector projection

According to Equation (4.40),

$$\begin{aligned}
\langle\pi_B^{(+1)}(\mathbf{k})\pi_B^{(+1)*}(\mathbf{k}')+\pi_B^{(-1)}(\mathbf{k})\pi_B^{(-1)*}(\mathbf{k}')\rangle &= 8f^V(k)\delta^{(3)}(\mathbf{k}-\mathbf{k}') \\
&= 2\langle\Pi_{B(ab)}^{(V)}(\mathbf{k})\Pi_{B(ab)}^{(V)*}(\mathbf{k}')\rangle \\
&= (2\pi)^3\frac{2\pi^2}{k^3}\delta^{(3)}(\mathbf{k}-\mathbf{k}')\mathcal{P}^{(+)}_{\Pi_B^{(V)}\Pi_B^{(V)}}(k), \\
\langle\pi_B^{(+1)}(\mathbf{k})\pi_B^{(+1)*}(\mathbf{k}')-\pi_B^{(-1)}(\mathbf{k})\pi_B^{(-1)*}(\mathbf{k}')\rangle &= -8g^V(k)\delta^{(3)}(\mathbf{k}-\mathbf{k}') \\
&= (2\pi)^3\frac{2\pi^2}{k^3}\delta^{(3)}(\mathbf{k}-\mathbf{k}')\mathcal{P}^{(-)}_{\Pi_B^{(V)}\Pi_B^{(V)}}(k).
\end{aligned} \tag{4.58}$$

The two point correlation function of $\Pi_{ij}^{(V)}$ (Eq.4.30) is

$$\begin{aligned}
\langle\Pi_{ab}^{(V)}(\mathbf{k})\Pi_{ab}^{(V*)}(\mathbf{k}')\rangle &= \frac{1}{\rho_\gamma^2}\delta_{ac}\delta_{bd}(P_{ai}\hat{k}_b\hat{k}_j+P_{bj}\hat{k}_a\hat{k}_i)(P_{dm}\hat{k}_c\hat{k}_l+P_{cl}\hat{k}_d\hat{k}_m) \\
&\quad\times\langle T_{B(ij)}^{(2)}(\mathbf{k})T_{B(lm)}^{(2)*}(\mathbf{k}')\rangle \\
&= \frac{\delta^{(3)}(\mathbf{k}-\mathbf{k}')}{\rho_\gamma^2(4\pi)^2a^8}\int d^3p\ [\ S(p)S(|\mathbf{k}-\mathbf{p}|)2(1-2\gamma^2\beta^2+\gamma\beta\mu) \\
&\quad -A(p)A(|\mathbf{k}-\mathbf{p}|)2(\beta\gamma-\mu)\ ]\,.
\end{aligned} \tag{4.59}$$

Remembering that

$$\mathbf{e}_{ab}^{(+1)}\mathbf{e}_{cd}^{(-1)}\langle\Pi_{B(ab)}^{(V)}\Pi_{B(cd)}^{(V)*}\rangle = (f^V(k)+g^V(k))\delta^{(3)}(\mathbf{k}-\mathbf{k}'), \tag{4.60}$$

where

$$
\begin{aligned}
f^V(k) &= \frac{1}{\rho_\gamma^2(4\pi)^2a^8}\delta^{(3)}(\mathbf{k}-\mathbf{k}')\frac{1}{4}\int d^3p\ [\ S(p)S(|\mathbf{k}-\mathbf{p}|)2(1-2\gamma^2\beta^2+\gamma\beta\mu) \\
&\quad -A(p)A(|\mathbf{k}-\mathbf{p}|)2(\beta\gamma-\mu)\ ]\,, \\
g^V(k) &= \frac{1}{\rho_\gamma^2(4\pi)^2a^8}\delta^{(3)}(\mathbf{k}-\mathbf{k}')\frac{1}{4}\int d^3p\ [\ S(p)A(|\mathbf{k}-\mathbf{p}|)2(\beta+\gamma\mu-2\beta\gamma^2) \\
&\quad +A(p)S(|\mathbf{k}-\mathbf{p}|)2(\beta\mu+\gamma-2\gamma\beta^2)\ ]\ . \qquad (4.61)
\end{aligned}
$$

we obtain

$$
\begin{aligned}
\mathcal{P}^{(+)}_{\Pi_B^{(V)}\Pi_B^{(V)}}(k) &= 8\times\frac{1}{4}\ \frac{2k^3}{4(2\pi)^2(\rho_{\gamma,0})^2(2\pi)^5}\int d^3p \\
&\quad\times[\ S(p)S(|\mathbf{k}-\mathbf{p}|)2(1-2\gamma^2\beta^2+\gamma\beta\mu)-A(p)A(|\mathbf{k}-\mathbf{p}|)2(\beta\gamma-\mu)\ ]\,.
\end{aligned} \qquad (4.62)
$$

Rewriting it in terms of x and z gives

$$
\begin{aligned}
\mathcal{P}^{(+)}_{\Pi_B^{(V)}\Pi_B^{(V)}}(k) &= 2\frac{S_0^2}{(\rho_{\gamma,0})^2(2\pi)^6}k^{2n_s+6}\int dz z^{n_s+2} \\
\times\int dx\left(1-2zx+z^2\right)^{\frac{n_s-2}{2}}&(-2z^2(x^4)+3z(x^3)+(z^2-1)(x^2)-3zx+z^2+1) \\
&-2\frac{A_0^2}{(\rho_{\gamma,0})^2(2\pi)^6}k^{2n_A+6}\int dz z^{n_A+3}\int dx(1-2zx+z^2)^{\frac{n_A-1}{2}}(1-x^2).
\end{aligned} \qquad (4.63)
$$

We also have

$$
\begin{aligned}
\mathcal{P}^{(-)}_{\Pi_B^{(V)}\Pi_B^{(V)}}(k) &= -8\times\frac{1}{4}\ \frac{2k^3}{4(2\pi)^2(\rho_{\gamma,0})^2(2\pi)^5}\int d^3p \\
\times[\ S(p)A(|\mathbf{k}-\mathbf{p}|)2(\beta-2\gamma\beta^2+\gamma\mu)&+A(p)S(|\mathbf{k}-\mathbf{p}|)2(\beta\mu+\gamma-2\gamma\beta^2)\ ]\ ,
\end{aligned} \qquad (4.64)
$$

which can be rewritten in terms of x and z as

$$
\begin{aligned}
\mathcal{P}^{(-)}_{\Pi_B^{(V)}\Pi_B^{(V)}}(k) &= -2\frac{S_0A_0}{(2\pi)^6(\rho_\gamma^0)^2}k^{n_A+n_S+6} \\
&\quad\times[\int dz z^{n_s+2}\int dx\left(1-2zx+z^2\right)^{\frac{n_A-1}{2}}(2zx^3-x^2-2zx+1) \\
&\quad-\int dz z^{n_A+3}\int dx(1-2zx+z^2)^{\frac{n_S-2}{2}}(2zx^3-x^2-2zx+1)\ ]\ .
\end{aligned} \qquad (4.65)
$$

4.1.6 The tensor projection

According to Equation (4.45),

$$\begin{aligned}
\langle \pi_B^{(+2)}(\mathbf{k})\pi_B^{(+2)*}(\mathbf{k}') + \pi_B^{(-2)}(\mathbf{k})\pi_B^{(-2)*}(\mathbf{k}')\rangle &= \frac{8}{9} f^T(k)\delta^{(3)}(\mathbf{k}-\mathbf{k}') \\
&= \frac{2}{3}\langle \Pi^{(T)}_{B(ab)}(\mathbf{k})\Pi^{(T)*}_{B(ab)}(\mathbf{k}')\rangle \\
&= (2\pi)^3 \frac{2\pi^2}{k^3}\delta^{(3)}(\mathbf{k}-\mathbf{k}')\mathcal{P}^{(+)}_{\Pi_B^{(T)}\Pi_B^{(T)}}(k), \\
\langle \pi_B^{(+2)}(\mathbf{k})\pi_B^{(+2)*}(\mathbf{k}') - \pi_B^{(-2)}(\mathbf{k})\pi_B^{(-2)*}(\mathbf{k}')\rangle &= -\frac{8}{9} g^T(k)\delta^{(3)}(\mathbf{k}-\mathbf{k}') \\
&= (2\pi)^3 \frac{2\pi^2}{k^3}\delta^{(3)}(\mathbf{k}-\mathbf{k}')\mathcal{P}^{(-)}_{\Pi_B^{(T)}\Pi_B^{(T)}}(k).
\end{aligned} \tag{4.66}$$

The two point correlation function of $\Pi_{ij}^{(T)}$ (see Eq. (refpit)) is

$$\begin{aligned}
\langle \Pi^{(T)}_{B(ab)}(\mathbf{k})\Pi^{(T)*}_{B(ab)}(\mathbf{k}')\rangle &= \frac{1}{\rho_\gamma^2}\delta_{ac}\delta_{bd}(P_{ai}P_{bj} - \frac{1}{2}P_{ab}P_{ij})(P_{cl}P_{dm} - \frac{1}{2}P_{cd}P_{lm}) \\
&\quad \times \langle T^{(2)}_{B(ij)}(\mathbf{k})T^{(2)*}_{B(lm)}(\mathbf{k}')\rangle \\
&= \frac{1}{\rho_\gamma^2(4\pi)^2 a^8}\delta^{(3)}(\mathbf{k}-\mathbf{k}')\int d^3p\ [\ S(p)S(|\mathbf{k}-\mathbf{p}|) \\
&\quad \times(1+\gamma^2)(1+\beta^2) - A(p)A(|\mathbf{k}-\mathbf{p}|)(-4\gamma\beta)\ ].
\end{aligned} \tag{4.67}$$

Remembering that

$$\mathbf{e}^{(+2)}_{ab}\mathbf{e}^{(-2)}_{cd}\langle \Pi^{(T)}_{B(ab)}\Pi^{(T)*}_{B(cd)}\rangle = (f^T(k) + g^T(k))\delta^{(3)}(\mathbf{k}-\mathbf{k}'), \tag{4.68}$$

where

$$\begin{aligned}
f^T(k) &= \frac{1}{\rho_\gamma^2(4\pi)^2 a^8}\delta^{(3)}(\mathbf{k}-\mathbf{k}')\frac{3}{4}\int d^3p\ [\ S(p)S(|\mathbf{k}-\mathbf{p}|)(1+\gamma^2)(1+\beta^2) \\
&\quad -A(p)A(|\mathbf{k}-\mathbf{p}|)(-4\gamma\beta)\ ], \\
g^T(k) &= \frac{1}{\rho_\gamma^2(4\pi)^2 a^8}\delta^{(3)}(\mathbf{k}-\mathbf{k}')\frac{3}{4}\int d^3p\ [\ S(p)A(|\mathbf{k}-\mathbf{p}|)2(1+\gamma^2)\beta \\
&\quad +A(p)S(|\mathbf{k}-\mathbf{p}|)2(1+\beta^2)\gamma\ ]\ ,
\end{aligned} \tag{4.69}$$

we obtain

$$\mathcal{P}^{(+)}_{\Pi_B^{(T)}\Pi_B^{(T)}}(k) = \frac{8}{9} \times \frac{3}{4} \frac{2k^3}{4(2\pi)^2(\rho^0_\gamma)^2(2\pi)^5} \int d^3p \\ \times [\ S(p)S(|\mathbf{k}-\mathbf{p}|)(1+\gamma^2)(1+\beta^2) + A(p)A(|\mathbf{k}-\mathbf{p}|)(4\gamma\beta)\ ]\,. \tag{4.70}$$

Rewriting it in terms of x and z gives

$$\mathcal{P}^{(+)}_{\Pi_B^{(T)}\Pi_B^{(T)}}(k) = \frac{2}{3}\frac{S_0^2}{(\rho_{\gamma,0})^2(2\pi)^6}k^{2n_s+6}\int dz z^{n_s+2} \\ \times \int dx \left(1-2zx+z^2\right)^{\frac{n_s-2}{2}} (1+x^2)(1+z^2/2(1+x^2)-2zx) \\ +\frac{4}{3}\frac{A_0^2}{(\rho_{\gamma,0})^2(2\pi)^6}k^{2n_A+6}\int dz z^{n_A+2}\int dx(1-2zx+z^2)^{\frac{n_A-1}{2}}x(1-zx). \tag{4.71}$$

Similarly,

$$\mathcal{P}^{(-)}_{\Pi_B^{(T)}\Pi_B^{(T)}}(k) = \frac{-8}{9} \times \frac{3}{4} \frac{2k^3}{4(2\pi)^2(\rho^0_\gamma)^2(2\pi)^5} \int d^3p \\ \times [\ S(p)A(|\mathbf{k}-\mathbf{p}|)2(1+\gamma^2)\beta + A(p)S(|\mathbf{k}-\mathbf{p}|)2(1+\beta^2)\gamma\ ]\ , \tag{4.72}$$

which, written in terms of x and z becomes

$$\mathcal{P}^{(-)}_{\Pi_B^{(T)}\Pi_B^{(T)}}(k) = \frac{-2}{3}\frac{S_0A_0}{(\rho_{\gamma,0})^2(2\pi)^6}k^{n_A+n_S+6}[\int dz z^{n_s+2} \\ \times \int dx \left(1-2zx+z^2\right)^{\frac{n_A-1}{2}} (1+x^2)(1-zx) \\ +\int dz z^{n_A+2}\int dx(1-2zx+z^2)^{\frac{n_S-2}{2}}(2+z^2-4zx+z^2x^2)x\ ]\ . \tag{4.73}$$

4.1.7 Integral values with the absence of cutoff

In the above equations (4.51, 4.54, 4.57 , 4.63, 4.65 , 4.71 , 4.73), the integrals can be split into an integral over z from 0 to $\frac{k_D}{k}$. When $k_D \gg k$, the integral can be set as $\int_0^\infty$. When we solve these integral we find that when spectral index $n < -2$, the results calculated from $\int_0^{\frac{k_D}{k}}$ is very close to the approximate values obtained from $\int_0^\infty$. Ignoring the cutoff in the definitions of S_B and A_B allows us factor out the k-dependence of the above integrals, we define the following expressing by dividing the coefficients, hence, the above integrals will depend only on the spectral index. From table. 4.1, we can see that in most cases the

contribution of helicity to CMB spectra is small and negative. When $n > -2$, the above integrals should be calculated from 0 to $\frac{k_D}{k}$, because the approximate solutions with the absence of cutoff is quite different from the exact solutions $\int_0^{\frac{k_D}{k}}$. In chapter 5 we will see that the behavior of the integrals are quite different in ranges between $-3 < n < -1.5$ and $-1.5 < n$. In the range $-3 < n < -1.5$, when we increase the spectral index the absolute values of the integrals get smaller, while in the range $-1.5 < n$ it is the opposite. This is because when $-3 < n < -1.5$ the cutoff effects are not dominant; while $-1.5 < n$, the dominant terms are k_D^{2n+6}, increasing n leads to greater amplitudes.

	$n = -2.9$	$n = -2.5$	$n = -2$
$\mathcal{W}^{S}_{\Delta_B\Delta_B}$	13.39	2.7225	1.85025
$\mathcal{W}^{A}_{\Delta_B\Delta_B}$	0.112	0.444	0.999
$\mathcal{W}^{S}_{\Delta_B\Pi_B^{(0)}}$	-13.025	-2.24275	-0.926
$\mathcal{W}^{A}_{\Delta_B\Pi_B^{(0)}}$	1.575	0.8895	0.50025
$\mathcal{W}^{S}_{\Pi_B^{(0)}\Pi_B^{(0)}}$	14.625	3.68275	2.77525
$\mathcal{W}^{A}_{\Pi_B^{(0)}\Pi_B^{(0)}}$	-3.2625	-2.223	-1.9995
$\mathcal{W}^{+S}_{\Pi_B^{(V)}\Pi_B^{(V)}}$	52.8	10.6762	7.401
$\mathcal{W}^{+A}_{\Pi_B^{(V)}\Pi_B^{(V)}}$	-4.498	-3.556	-3.998
$\mathcal{W}^{+S}_{\Pi_B^{(T)}\Pi_B^{(T)}}$	35.36	6.6914	3.701
$\mathcal{W}^{+A}_{\Pi_B^{(T)}\Pi_B^{(T)}}$	2.7	1.1867	0.00133
$\mathcal{W}^{(-)}_{\Pi_B^{(V)}\Pi_B^{(V)}}$	-47.98	-6.712	-2.668
$\mathcal{W}^{(-)}_{\Pi_B^{(T)}\Pi_B^{(T)}}$	-38.0267	-7.8267	-3.704

Table 4.1: Integral values calculated when $k_D \gg k$ and the cutoff is ignored. $'S'$ means the non-helical parts, $'A'$ means the helical parts.

$$
\begin{aligned}
&\frac{\mathcal{P}^{S}_{\Delta_B\Delta_B}(k)}{\frac{S_0^2}{(\rho_{\gamma,0})^2(2\pi)^6}k^{2n_s+6}} = \mathcal{W}^{S}_{\Delta_B\Delta_B} \quad , \quad \frac{\mathcal{P}^{A}_{\Delta_B\Delta_B}(k)}{\frac{A_0^2}{(\rho_{\gamma,0})^2(2\pi)^6}k^{2n_A+6}} = \mathcal{W}^{A}_{\Delta_B\Delta_B},\\
&\frac{\mathcal{P}^{S}_{\Pi_B^{(0)}\Pi_B^{(0)}}(k)}{\frac{S_0^2}{(\rho_{\gamma,0})^2(2\pi)^6}k^{2n_s+6}} = \mathcal{W}^{S}_{\Pi_B^{(0)}\Pi_B^{(0)}} \quad , \quad \frac{\mathcal{P}^{A}_{\Pi_B^{(0)}\Pi_B^{(0)}}(k)}{\frac{A_0^2}{(\rho_{\gamma,0})^2(2\pi)^6}k^{2n_A+6}} = \mathcal{W}^{S}_{\Pi_B^{(0)}\Pi_B^{(0)}},\\
&\frac{\mathcal{P}^{S}_{\Delta_B\Pi_B^{(0)}}(k)}{\frac{S_0^2}{(\rho_{\gamma,0})^2(2\pi)^6}k^{2n_s+6}} = \mathcal{W}^{S}_{\Delta_B\Pi_B^{(0)}} \quad , \quad \frac{\mathcal{P}^{A}_{\Delta_B\Pi_B^{(0)}}(k)}{\frac{A_0^2}{(\rho_{\gamma,0})^2(2\pi)^6}k^{2n_A+6}} = \mathcal{W}^{A}_{\Delta_B\Pi_B^{(0)}},\\
&\frac{\mathcal{P}^{+S}_{\Pi_B^{(V)}\Pi_B^{(V)}}(k)}{\frac{S_0^2}{(\rho_{\gamma,0})^2(2\pi)^6}k^{2n_s+6}} = \mathcal{W}^{+S}_{\Pi_B^{(V)}\Pi_B^{(V)}} \quad , \quad \frac{\mathcal{P}^{+A}_{\Pi_B^{(V)}\Pi_B^{(V)}}(k)}{\frac{A_0^2}{(\rho_{\gamma,0})^2(2\pi)^6}k^{2n_A+6}} = \mathcal{W}^{+A}_{\Pi_B^{(V)}\Pi_B^{(V)}},\\
&\frac{\mathcal{P}^{(-)}_{\Pi_B^{(V)}\Pi_B^{(V)}}(k)}{\frac{S_0A_0}{(2\pi)^6(\rho_\gamma^0)^2}k^{n_A+n_S+6}} = \mathcal{W}^{(-)}_{\Pi_B^{(V)}\Pi_B^{(V)}} \quad , \quad \frac{\mathcal{P}^{(-)}_{\Pi_B^{(T)}\Pi_B^{(T)}}(k)}{\frac{S_0A_0}{(\rho_{\gamma,0})^2(2\pi)^6}k^{n_A+n_S+6}} = \mathcal{W}^{(-)}_{\Pi_B^{(T)}\Pi_B^{(T)}},\\
&\frac{\mathcal{P}^{+S}_{\Pi_B^{(T)}\Pi_B^{(T)}}(k)}{\frac{S_0^2}{(\rho_{\gamma,0})^2(2\pi)^6}k^{2n_s+6}} = \mathcal{W}^{+S}_{\Pi_B^{(T)}\Pi_B^{(T)}} \quad , \quad \frac{\mathcal{P}^{+A}_{\Pi_B^{(T)}\Pi_B^{(T)}}(k)}{\frac{A_0^2}{(\rho_{\gamma,0})^2(2\pi)^6}k^{2n_A+6}} = \mathcal{W}^{+A}_{\Pi_B^{(T)}\Pi_B^{(T)}}.
\end{aligned}
\tag{4.74}
$$

4.2 The PMF impact on the CMB anisotropies

In this section we describe how primordial magnetic fields source the Cosmic Microwave Background (CMB) anisotropies and modify the initial conditions. The subject has already been studied in detail in [63]. The evolution of metric perturbations is described by the Einstein equations. These are modified by the presence of PMFs that represent a source term as follows:

$$
G_{\mu\nu} = 8\pi(T_{\mu\nu} + T_{B(\mu\nu)}) \,, \tag{4.75}
$$

where $T_{B(\mu\nu)}$ represents the PMF.

4.2.1 Scalar modes

Photons (γ), neutrinos (ν), baryons (b), cold dark matter (c) and the magnetic field (B) contribute to the total energy density perturbation, so that

$$
\bar{\rho}\Delta \;=\; \rho_\gamma(\Delta_\gamma + \Delta_{\rm B}) + \rho_\nu\Delta_\nu + \rho_{\rm c}\Delta_{\rm c} + \rho_{\rm b}\Delta_{\rm b}. \tag{4.76}
$$

The total anisotropic stress are given by

$$
\bar{p}\Pi \;=\; \frac{1}{3}\rho_\gamma(\pi_\gamma + \Pi_{\rm B}^{(0)}) + \frac{1}{3}\rho_\nu\pi_\nu. \tag{4.77}
$$

There is no pressure or anisotropic stress for the baryons and dark matter.

The Lorentz force induced on baryons modifies the baryon scalar velocity equation:

$$\dot{v}_b = -\frac{\dot{a}}{a}v_b + c_s^2 k v_b + R n_e a \sigma_T (v_\gamma - v_b) + \frac{R}{4}L^{(0)} \tag{4.78}$$

where $R = \frac{\rho_\gamma + p_\gamma}{\rho_b + p_b} = \frac{4\rho_\gamma}{3\rho_b}$. n_e is the free electron density and σ_T is the Thomson cross section, the differential optical depth $\dot{\tau} = n_e a \sigma_T$ describes the collision rate in conformal time. The scalar mode of Lorentz force is $L^{(0)} = k(\Delta_B - 2\Pi_{\rm B}^{(0)})$, $R = \frac{4}{3}\frac{\rho_\gamma}{\rho_b}$.

4.2.2 Vector modes

The perturbed vector Einstein equations become

$$\ddot{H}_T^{(\pm 1)} + 2\frac{\dot{a}}{a}\ddot{H}_T^{(\pm 1)} = -8\pi G a^2 (p_f \Pi_f^{(\pm 1)} + p_\gamma \Pi_B^{(\pm 1)}) \tag{4.79}$$

The Lorentz force induced on baryons, in analogy with what we found for the scalar case, modifies the baryon vector velocity equation:

$$\dot{v}_b^{(\pm 1)} = -\frac{\dot{a}}{a}v_b^{(\pm 1)} + R n_e a \sigma_T (v_\gamma^{(\pm 1)} - v_b^{(\pm 1)}) - \frac{3R}{8}(k\Pi_B^{(\pm 1)}), \tag{4.80}$$

where $k\Pi_B^{(\pm 1)}$ is the Lorentz force due to the primordial magnetic field.

4.2.3 Tensor modes

The perturbed Einstein equation for the tensor modes is given by

$$\ddot{H}_T^{(\pm 2)} + 2\frac{\dot{a}}{a}\dot{H}_T^{(\pm 2)} + k^2 H_T^{(\pm 2)} = 8\pi G a^2 (p_f \Pi_f^{(\pm 2)} + p_\gamma \Pi_B^{(\pm 1)}). \tag{4.81}$$

4.3 Initial conditions and the magnetic modes

Now that we have the Boltzmann and Einstein equations, to solve them, we need the appropriate initial conditions for the scalar, vector, and tensor modes. Before neutrino decoupling, $\eta < \eta_\nu$, the magnetic anisotropic stress is the only source of anisotropic stress and it cannot be compensated by the free streaming of neutrinos. Current numerical codes (such as CAMB) set the initial conditions on super-horizon scales $k\eta \ll 1$, long after neutrino decoupling $\eta > \eta_\nu$, after the neutrinos could develop their anisotropic stress. After neutrino decoupling, the non vanishing neutrino anisotropic stress cancels the magnetic source. Thus, there are two types of so-called "modes", corresponding to the two regimes in which the PMF sources metric perturbations. The passive mode [63, 64] sources perturbations before the neutrino decoupling, while the compensated mode [65, 66, 67] sources them after. In our model-independent approach, we assume that the PMFs could be generated at any time between the end of inflation and recombination, and consider both the passive and the compensated modes.

PMFs source all types of perturbations, scalar and tensor modes have both passive and compensated initial conditions, vector modes have only compensated initial conditions. As we will see later from numerical calculations, the dominant contributions come from the scalar mode, passive tensor mode, and the compensated vector mode. We include the standard matter species which we generally denote with subscripts: photons (γ), baryons (b), cold dark matter (c), massless neutrinos (ν). To solve the evolution of the background equation we solve the Friedmann equations for the scale factor. Following the usual conventions [63], we use the ratio of the density of species x to the critical density $\Omega_x = \rho_x/\rho_{\rm cr}$. We have radiation $\Omega_r = \Omega_\gamma + \Omega_\nu$ and matter $\Omega_m = \Omega_b + \Omega_c$, and it will also be convenient to define ratios $R_\gamma = \Omega_\gamma/\Omega_r$, $R_\nu = \Omega_\nu/\Omega_r$, $R_c = \Omega_c/\Omega_m$ and $R_b = \Omega_b/\Omega_m$.

4.3.1 Compensated modes

The compensated modes are the standard solution of the perturbed Einstein-Boltzmann equations with the PMF source contributing *after* neutrino decoupling. These modes are called 'compensated' because the PMF stresses are compensated by those of the relativistic fluids in their contributions to the metric perturbations and the initial conditions. When solving the Boltzmann and Einstein equations for large wavelengths at early times, the growing regular mode requires the source terms in the equations for the metric perturbations to vanish $h_T^{(0)} = 0$ at the lowest order. Thus, there is compensation between the magnetic terms $\Pi_B \neq 0$ and the perturbed components of the fluid. There are no passive vector modes because $H_T^{(\pm1)}$ decays rapidly, and the evolution before neutrino decoupling is not essential. With a PMF as an active source for the vector part of the Einstein-Boltzmann equations, the only regular solution is a compensated mode for which the anisotropic stress $\Pi_B^{(\pm1)}$ is compensated by $\Pi_\nu^{(\pm1)}$.

The PMF also actively sources the compensated scalar modes after neutrino decoupling. There are two such modes, sourced by Δ_B and $\Pi_B^{(0)}$, with power spectra proportional to the two-point correlations $\langle \Delta_B^* \Delta_B \rangle$ and $\langle \Pi_B^{(0)*} \Pi_B^{(0)} \rangle$, and the cross-correlation $\langle \Delta_B^* \Pi_B^{(0)} \rangle$. After neutrino decoupling, the anisotropic stress of the PMF is compensated, leading to the tensor compensated mode. We will see later that the tensor compensated mode is entirely negligible compared to other modes and can be safely ignored when deriving the CMB constraints on the PMF.

4.3.2 Passive modes

When a PMF is generated *before* neutrino decoupling, there is a passive mode derived from the homogeneous solutions. Before neutrino decoupling, the universe is dominated by the radiation fluid with $w = 1/3$, neutrinos are tightly bound with photons and baryons in the fluid, and there are no components to compensate for the anisotropic stress of the PMF. Thus, it leads to a logarithmically growing (in conformal time) metric perturbation mode. After neutrino decoupling, both passive and compensated modes are suppressed by the neu-

trino compensation. Such logarithmically growing properties of the passive modes remain as a constant offset on the amplitude of the inflationary mode, which is the primary cosmological perturbations of the standard model without PMFs. The existence of this amplitude offset is also needed to match the initial conditions before and after neutrino decoupling. Tensor modes have both passive and compensated modes. Before neutrino decoupling, with all species having zero initial anisotropic stress, $\Pi_B^{(\pm 2)}$ sources the tensor passive mode proportional to the ratio between the neutrino decoupling time and the generation time of the PMF (η_ν/η_B). On superhorizon scales, $k\eta \ll 1$, the solution of Equation (4.81) at the time of neutrino decoupling η_ν is approximately $H^{(\pm 2)}(\eta_\nu) \simeq H^{(\pm 2)}(\eta_B) + R_\gamma \Pi_B^{(\pm 2)} \beta$, where we defined $\beta \equiv \ln(\eta_\nu/\eta_B)$, η_ν is the neutrino decoupling time, η_B is the time of magnetic field generation, and we assume $H^{(\pm 2)}(\eta_B) = 0$ [63, 64].

4.3.3 Scalars

The amplitude of the adiabatic scalar mode is described by the comoving curvature perturbation ζ. Due to the generation of a PMF before neutrino decoupling, there is an additional contribution to ζ. At the time η_ν neutrinos decouple, its anisotropic stress rapidly grows to compensate the PMF anisotropic stress $\Pi_\nu \to -\frac{R_\gamma}{R_\nu}\Pi_B$. When the compensation is effective, ζ stops growing, having reached the final curvature [63].

$$\zeta = \zeta(\eta_B) - R_\gamma \Pi_B^{(0)} \left[\ln(\eta_\nu/\eta_B) + \left(\frac{5}{8R_\nu} - 1 \right) \right], \tag{4.82}$$

where $\zeta(\eta_B)$ is the comoving curvature perturbation at the time η_B, after inflation, at which the PMF was generated. For the scalar passive mode, all components have zero initial anisotropic stress and unperturbed densities, and result in adiabatic type perturbations. Since ζ is proportional to $-R_\gamma \Pi_B^{(0)} \beta$, only $\langle \Pi_B^{(0)*} \Pi_B^{(0)} \rangle$ sources the scalar passive mode.

4.3.4 Tensors

Only the photons and neutrinos can support tensor perturbations to their energy momentum tensors and at times long before recombination the photon anisotropic stress is negligible. Thus the species affecting the tensor evolution are the neutrinos, and the magnetic fields. The passive tensor mode has [63, 64]

$$H_T^{(\pm 2)} = 3 R_\gamma \Pi_B^{(\pm 2)} \left[\ln(\eta_\nu/\eta_B) + \left(\frac{5}{8R_\nu} - 1 \right) \right]. \tag{4.83}$$

For simplicity, it is assumed that $H_T^{(\pm 2)}(\eta_B) = 0$. We note that CAMB uses H_T, where $h_{ij} = \sum_{k\pm} 2 H_T Q_{ij}^2$ in tensor modes, h_{ij} is the transverse traceless part of the metric tensor. This introduces an additional factor of 1/4 into the result for the C_l in terms of P_h. Considering

this, we have

$$P_h = \left[6R_\gamma \ln(\eta_\nu/\eta_B) + \left(\frac{5}{8R_\nu} - 1\right)\right]^2 \times \langle \Pi_B^{(\pm 2)*} \Pi_B^{(\pm 2)} \rangle \,. \tag{4.84}$$

4.4 CMB spectra sourced by the PMF

In general, the angular power spectra of the correlation functions can be calculated from Equation (3.35). After applying Eqs. (3.41), (3.46) and (3.45), we can obtain $C_l^{X\tilde{X}}$ written in terms of the magnetic field sources in relevant modes as

$$\begin{aligned} C_l^{TT} &= \frac{2}{\pi}\frac{1}{(2l+1)^2}\int k^2 dk \sum_m \Theta_l^{(m)*}(\eta_0,k)\Theta_l^{(m)}(\eta_0,k) \\ &= C_l^{TT(0)} + \frac{2}{\pi}\int k^2 dk \Big[\left(\int_0^{\eta_0} d\eta e^{-\tau} \sum_{l'} S_{l'}^{(1)}(\eta) j_l^{(l'1)}(\chi)\right)^2 \\ &\quad \times \langle \pi_B^{(+1)*}\pi_B^{(+1)} + \pi_B^{(-1)*}\pi_B^{(-1)} \rangle \\ &\quad + \left(\int_0^{\eta_0} d\eta e^{-\tau} \sum_{l'} S_{l'}^{(2)}(\eta) j_l^{(l'2)}(\chi)\right)^2 \times \langle \pi_B^{(+2)*}\pi_B^{(+2)} + \pi_B^{(-2)*}\pi_B^{(-2)} \rangle \Big]. \end{aligned} \tag{4.85}$$

The term $\sum_{l'} S_{l'}^{(0)}(\eta) j_l^{(l'0)}(\chi)$ in Eq. (3.41) can be divided into two parts $\sum_{l'} S_{l'}^{(0)}(\eta) j_l^{(l'0)}(\chi) = S_{(\Delta_B)}^{(0)} \Delta_B + S_{(\Pi_B^{(0)})}^{(0)} \Pi_B^{(0)}$, where $S_{(\Delta_B)}^{(0)}$ are terms sourced by Δ_B and $S_{(\Pi_B^{(0)})}^{(0)}$ are terms sourced by $\Pi_B^{(0)}$, hence, we obtain

$$\begin{aligned} C_l^{TT(0)} &= \frac{2}{\pi}\int k^2 dk \Big[+ \left(\int_0^{\eta_0} d\eta e^{-\tau} S_{(\Delta_B)}^{(0)}(\eta)\right)^2 \times \langle \Delta_B^* \Delta_B \rangle \\ &\quad + \left(\int_0^{\eta_0} d\eta e^{-\tau} S_{(\Pi_B^{(0)})}^{(0)}(\eta)\right)^2 \times \langle \Pi_B^{(0)*} \Pi_B^{(0)} \rangle \\ &\quad + 2 \left(\int_0^{\eta_0} d\eta e^{-\tau} S_{(\Delta_B)}^{(0)}(\eta)\right) \left(\int_0^{\eta_0} d\eta' e^{-\tau} S_{(\Pi_B^{(0)})}^{(0)}(\eta')\right) \times \langle \Delta_B^* \Pi_B^{(0)} \rangle \Big]. \end{aligned} \tag{4.86}$$

Similarly, for the E-mode spectrum, we have

$$\begin{aligned} C_l^{EE} &= \frac{2}{\pi}\frac{1}{(2l+1)^2}\int k^2 dk \sum_m E_l^{(m)*}(\eta_0,k) E_l^{(m)}(\eta_0,k), \\ &= C_l^{EE(0)} + \frac{2\times 6}{\pi}\int k^2 dk \Big[\left(\int_0^{\eta_0} d\eta e^{-\tau} \dot{\tau} \epsilon_l^{(1)}(\chi) P^{(1)}(\eta)\right)^2 \\ &\quad \times \langle \pi_B^{(+1)*}\pi_B^{(+1)} + \pi_B^{(-1)*}\pi_B^{(-1)} \rangle \\ &\quad + \left(\int_0^{\eta_0} d\eta e^{-\tau} \dot{\tau} \epsilon_l^{(2)}(\chi) P^{(2)}(\eta)\right)^2 \times \langle \pi_B^{(+2)*}\pi_B^{(+2)} + \pi_B^{(-2)*}\pi_B^{(-2)} \rangle \Big]. \end{aligned} \tag{4.87}$$

The $P^{(0)}(\eta)$ term in Eq. (3.41) can be divided into two parts $P^{(0)}(\eta) = P^{(0)}_{(\Delta_B)}\Delta_B + P^{(0)}_{(\Pi^{(0)}_B)}\Pi^{(0)}_B$, where $P^{(0)}_{(\Delta_B)}$ are terms sourced by Δ_B and $P^{(0)}_{(\Pi^{(0)}_B)}$ are terms sourced by $\Pi^{(0)}_B$, hence, we obtain

$$\begin{aligned}
C_l^{EE(0)} &= \frac{2\times 6}{\pi}\int k^2dk\Big[+\left(\int_0^{\eta_0} d\eta e^{-\tau}\dot{\tau}\epsilon_l^{(0)}(\chi)P^{(0)}_{(\Delta_B)}(\eta)\right)^2\times\langle\Delta_B^*\Delta_B\rangle \\
&+\left(\int_0^{\eta_0} d\eta e^{-\tau}\dot{\tau}\epsilon_l^{(0)}(\chi)P^{(0)}_{(\Pi^{(0)}_B)}(\eta)\right)^2\times\langle\Pi_B^{(0)*}\Pi_B^{(0)}\rangle \\
&+2\left(\int_0^{\eta_0} d\eta e^{-\tau}\dot{\tau}\epsilon_l^{(0)}(\chi)P^{(0)}_{(\Delta_B)}(\eta)\right)\left(\int_0^{\eta_0} d\eta' e^{-\tau}\dot{\tau}\epsilon_l^{(0)}(\chi)P^{(0)}_{(\Pi^{(0)}_B)}(\eta')\right)\times\langle\Delta_B^*\Pi_B^{(0)}\rangle\Big].
\end{aligned} \tag{4.88}$$

For the TE cross-correlation spectrum, we have

$$\begin{aligned}
C_l^{TE} &= \frac{2}{\pi}\frac{1}{(2l+1)^2}\int k^2dk\sum_m \Theta_l^{(m)*}(\eta_0,k)E_l^{(m)}(\eta_0,k), \\
&= C_l^{TE(0)}+\frac{2\times\sqrt{6}}{\pi}\int k^2dk\Big[\left(\int_0^{\eta_0} d\eta e^{-\tau}\sum_{l'}S^{(1)}_{l'}(\eta)j_l^{(l'1)}(\chi)\right) \\
&\times\left(\int_0^{\eta_0} d\eta' e^{-\tau}\dot{\tau}\epsilon_l^{(1)}(\chi)P^{(1)}(\eta')\right)\times\langle\pi_B^{(+1)*}\pi_B^{(+1)}+\pi_B^{(-1)*}\pi_B^{(-1)}\rangle \\
&+\left(\int_0^{\eta_0} d\eta e^{-\tau}\sum_{l'}S^{(2)}_{l'}(\eta)j_l^{(l'2)}(\chi)\right)\left(\int_0^{\eta_0} d\eta' e^{-\tau}\dot{\tau}\epsilon_l^{(2)}(\chi)P^{(2)}(\eta')\right) \\
&\times\langle\pi_B^{(+2)*}\pi_B^{(+2)}+\pi_B^{(-2)*}\pi_B^{(-2)}\rangle\Big],
\end{aligned} \tag{4.89}$$

where

$$\begin{aligned}
C_l^{TE(0)} &= \frac{2\sqrt{6}}{\pi}\int k^2dk\Big[\left(\int_0^{\eta_0} d\eta e^{-\tau}S^{(0)}_{(\Delta_B)}(\eta)\right)\left(\int_0^{\eta_0} d\eta' e^{-\tau}\dot{\tau}\epsilon_l^{(0)}(\chi)P^{(0)}_{(\Delta_B)}(\eta')\right)\times\langle\Delta_B^*\Delta_B\rangle \\
&+\left(\int_0^{\eta_0} d\eta e^{-\tau}S^{(0)}_{(\Pi^{(0)}_B)}(\eta)\right)\left(\int_0^{\eta_0} d\eta' e^{-\tau}\dot{\tau}\epsilon_l^{(0)}(\chi)P^{(0)}_{(\Pi^{(0)}_B)}(\eta')\right)\times\langle\Pi_B^{(0)*}\Pi_B^{(0)}\rangle \\
&+\left(\int_0^{\eta_0} d\eta e^{-\tau}S^{(0)}_{(\Pi^{(0)}_B)}(\eta)\right)\left(\int_0^{\eta_0} d\eta' e^{-\tau}\dot{\tau}\epsilon_l^{(0)}(\chi)P^{(0)}_{(\Delta_B)}(\eta')\right)\times\langle\Delta_B^*\Pi_B^{(0)}\rangle \\
&+\left(\int_0^{\eta_0} d\eta e^{-\tau}S^{(0)}_{(\Delta_B)}(\eta)\right)\left(\int_0^{\eta_0} d\eta' e^{-\tau}\dot{\tau}\epsilon_l^{(0)}(\chi)P^{(0)}_{(\Pi^{(0)}_B)}(\eta')\right)\times\langle\Delta_B^*\Pi_B^{(0)}\rangle\Big].
\end{aligned} \tag{4.90}$$

The B-mode spectrum is

$$
\begin{aligned}
C_l^{BB} &= \frac{2}{\pi}\frac{1}{(2l+1)^2}\int k^2 dk \sum_m B_l^{(m)*}(\eta_0,k)B_l^{(m)}(\eta_0,k), \\
&= \frac{2\times 6}{\pi}\int k^2 dk\Big[-\left(\int_0^{\eta_0} d\eta e^{-\tau}\dot{\tau}\beta_l^{(1)}(\chi)P^{(1)}(\eta)\right)^2 \times \langle \pi_B^{(+1)*}\pi_B^{(+1)} + \pi_B^{(-1)*}\pi_B^{(-1)}\rangle \\
&\quad -\left(\int_0^{\eta_0} d\eta e^{-\tau}\dot{\tau}\beta_l^{(2)}(\chi)P^{(2)}(\eta)\right)^2 \times \langle \pi_B^{(+2)*}\pi_B^{(+2)} + \pi_B^{(-2)*}\pi_B^{(-2)}\rangle\Big]. \qquad (4.91)
\end{aligned}
$$

Finally, we have the parity-odd EB and TB spectra, given by

$$
\begin{aligned}
C_l^{EB} &= \frac{2}{\pi}\frac{1}{(2l+1)^2}\int k^2 dk \sum_m E_l^{(m)*}(\eta_0,k)B_l^{(m)}(\eta_0,k), \\
&= \frac{2\times 6}{\pi}\int k^2 dk\Big[\left(\int_0^{\eta_0} d\eta e^{-\tau}\dot{\tau}\epsilon_l^{(1)}(\chi)P^{(1)}(\eta)\right)\left(\int_0^{\eta_0} d\eta' e^{-\tau}\dot{\tau}\beta_l^{(1)}(\chi)P^{(1)}(\eta')\right) \\
&\quad \times\langle \pi_B^{(+1)*}\pi_B^{(+1)} - \pi_B^{(-1)*}\pi_B^{(-1)}\rangle \\
&\quad +\left(\int_0^{\eta_0} d\eta e^{-\tau}\dot{\tau}\epsilon_l^{(2)}(\chi)P^{(2)}(\eta)\right)\left(\int_0^{\eta_0} d\eta' e^{-\tau}\dot{\tau}\beta_l^{(2)}(\chi)P^{(2)}(\eta')\right) \\
&\quad \times\langle \pi_B^{(+2)*}\pi_B^{(+2)} - \pi_B^{(-2)*}\pi_B^{(-2)}\rangle\Big]. \qquad (4.92)
\end{aligned}
$$

and

$$
\begin{aligned}
C_l^{TB} &= \frac{2}{\pi}\frac{1}{(2l+1)^2}\int k^2 dk \sum_m \Theta_l^{(m)*}(\eta_0,k)B_l^{(m)}(\eta_0,k), \\
&= \frac{2\times\sqrt{6}}{\pi}\int k^2 dk\Big[\left(\int_0^{\eta_0} d\eta e^{-\tau}\sum_{l'} S_{l'}^{(1)}(\eta)j_l^{(l'1)}(\chi)\right)\left(\int_0^{\eta_0} d\eta' e^{-\tau}\dot{\tau}\beta_l^{(1)}(\chi)P^{(1)}(\eta')\right) \\
&\quad \times\langle \pi_B^{(+1)*}\pi_B^{(+1)} - \pi_B^{(-1)*}\pi_B^{(-1)}\rangle \\
&\quad +\left(\int_0^{\eta_0} d\eta e^{-\tau}\sum_{l'} S_{l'}^{(2)}(\eta)j_l^{(l'2)}(\chi)\right)\left(\int_0^{\eta_0} d\eta' e^{-\tau}\dot{\tau}\beta_l^{(2)}(\chi)P^{(2)}(\eta')\right) \\
&\quad \times\langle \pi_B^{(+2)*}\pi_B^{(+2)} - \pi_B^{(-2)*}\pi_B^{(-2)}\rangle\Big]. \qquad (4.93)
\end{aligned}
$$

4.5 Comparison with results in other papers

There have been several studies [63, 68] of the imprints in the anisotropies of the CMB due to the large scale magnetic fields. Shaw and Lewis [63] considered only the non-helical part of magnetic fields, and they made an assumption when calculating the integrals. Namely, they ignored the cutoff in the definitions of $S(\mathbf{k})$, so that their integrals become dimensionless and depend only on the spectral index. This approximation makes sense only for close to scale-invariant spectra, where the nontrivial contributions are from scales much larger than the damping scale k_D. In the following studies, we can still see that when spectral index

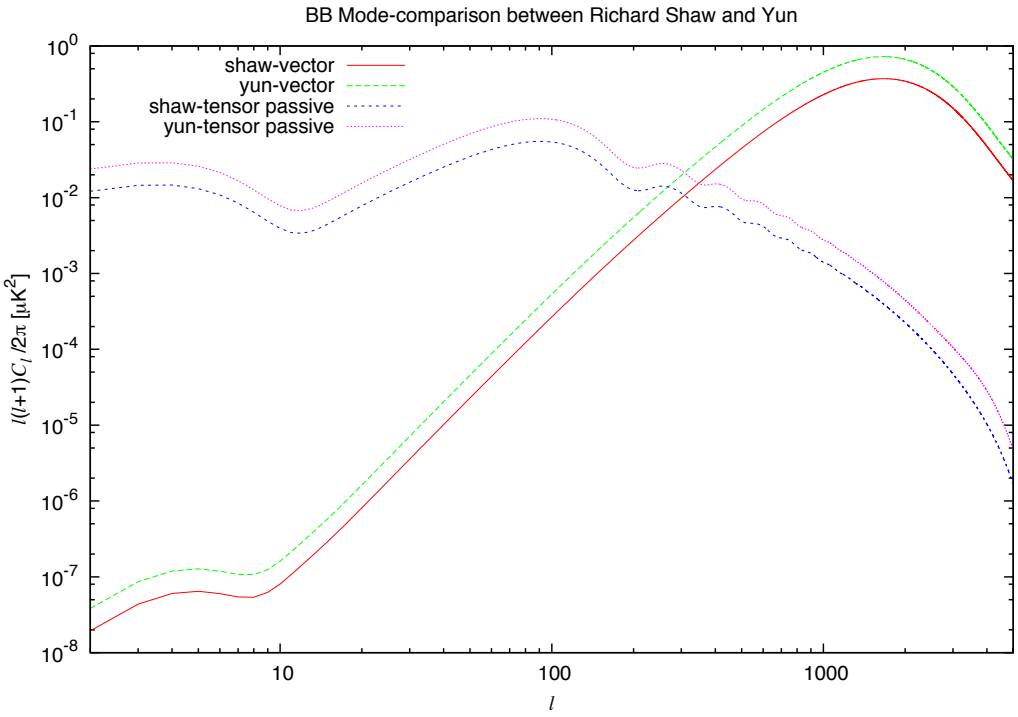

Figure 4.1: The BB angular power spectra for the vector tensor modes for the magnetic field strength $B = 4.1$ nG, spectral index of the symmetric part $n_S = -2.9$, $\eta_\nu/\eta_B = 10^{12}$. Comparison between Shaw and Lewis's results with ours. Shaw and Lewis's compensated vector modes are denoted by red solid lines, Shaw and Lewis's passive tensor modes are blue short dashed lines; our compensated vector modes are denoted green short dashed lines, tensor modes are pink dotted lines.

$n_B < -1.5$, the cutoff becomes largely irrelevant, their modifications of the power spectrum doesn't make any obvious effects on the C_ls. In their paper [63], they only calculated the results for a nearly scale invariant power spectrum and showed their impact on CMB by using their own developed Code, which they made public. Our code was based on theirs.

My results in Eq.(4.52) and Eq.(4.55) do not agree with Eq. (94) and Eq. (95) in their paper [63], although our results for integrals in Sections (4.1.4, 4.1.5 and 4.1.6) agree with the integral in their paper [63]. They missed a factor of 2 in their equations for the vector and tensor modes, coming from having two modes ± 1, ± 2. For example, the two-point correlation in vector projection is $\langle \Pi_B^{(+1)*}(\vec{k})\Pi_B^{(+1)}(\vec{k}') + \Pi_B^{(-1)*}(\vec{k})\Pi_B^{(-1)}(\vec{k}')\rangle$. We can see from Fig. (4.1), that Shaw and Lewis's results for both tensor and vector modes are a factor of 2 smaller than ours.

Kunze, in paper [68], derived the two-point correlations in all modes and considered both non-helical and helical magnetic fields, but they didn't study the effects of primordial magnetic fields on CMB. And Kunze used a different window function to model the magnetic power spectrum. She chose the powers spectra of the form,

$$P_S(k, k_m, k_L) = A_B \left(\frac{k}{k_L}\right)^{n_S} W(k, k_m) \tag{4.94}$$

$$P_A(k, k_m, k_L) = A_H \left(\frac{k}{k_L}\right)^{n_A} W(k, k_m), \tag{4.95}$$

where A_B and A_H are the amplitudes and n_S and n_A are the spectral indices of the symmetric and anti-symmetric parts, respectively. The damping of the magnetic field is determined by the Alfvén velocity and the Silk damping scale which leads to an estimate of the maximal wave number given by

$$k_m \simeq 200.694 \left(\frac{B}{\mathrm{nG}}\right)^{-1} \mathrm{Mpc}^{-1} \tag{4.96}$$

using the values of the best fit ΛCDM model of WMAP7 $\Omega_b = 0.0227h^{-2}$ and $h = 0.714$ [32]. The window function is assumed to be Gaussian of the form [68]

$$W(k, k_m) = \pi^{-\frac{3}{2}} k_m^{-3} e^{-\left(\frac{k}{k_m}\right)^2} \tag{4.97}$$

where the normalization is chosen such that $\int d^3k W(k, k_m) = 1$.

Our notation in calculating integrals in sections (4.1.4 4.1.5 4.1.6) is the same as Kunze did, we compared our results in Section 4.1 with Kunze's (Equations (3.17) to (3.23)), which are exactly the same when ignore the differences in coefficient and only compare the integrals $\int dz \int dx$ since we used different window functions.

Planck's paper [59] studied the constraints on primordial magnetic fields. They have full two-point correlations considering both non-helical and helical magnetic fields which is the same results as Paoletti [69], and they have their own code to calculate the effects on CMB and constrain for both non-helical and helical magnetic fields by using Planck data. When comparing our calculations on the integrals $\int dz \int dx$ in Section 4.1, I find that most of them agree, but the two-point correlations in vector modes doesn't agree with each other. In Paoletti, Finelli and Paci's paper [69], they applied the following vector projection of stress tensor in their calculations,

$$\Pi_{ij}^{(V)} = (P_{in}\hat{k}_j + P_{jn}\hat{k}_i)\hat{k}_m T_{B(mn)}, \tag{4.98}$$

$$\Pi_{i}^{(V)} = \Pi_{ij}^{(V)}\hat{k}_j = P_{in}\hat{k}_m T_{B(mn)}, \tag{4.99}$$

However, it doesn't satisfy symmetry for indices m and n and doesn't satisfy $T_{B(mn)} = \Pi^{(S)}_{B(mn)} + \Pi^{(T)}_{B(mn)} + \Pi^{(V)}_{B(mn)}$. The vector mode I used is

$$\Pi^{(V)}_{ij} = (P_{im}\hat{k}_j\hat{k}_n + P_{jn}\hat{k}_i\hat{k}_n)T_{B(mn)}, \tag{4.100}$$

The details are shown in Eq.(4.30). The two-point correlation function of $\Pi^{(V)}_{ij}$ (Eq.4.30) is

$$\begin{aligned}\langle\Pi^{(V)}_{ij}(\mathbf{k})\Pi^{(V*)}_{ij}(\mathbf{k}')\rangle &= \frac{1}{9p_\gamma^2}(P_{ai}\hat{k}_b\hat{k}_j + P_{bj}\hat{k}_a\hat{k}_i)(P_{al}\hat{k}_b\hat{k}_m + P_{bm}\hat{k}_a\hat{k}_l)\langle T_{B(ij)}(\mathbf{k})T^*_{B(mn)}(\mathbf{k}')\rangle \\ &= \frac{1}{9p_\gamma^2}(P_{jm}\hat{k}_i\hat{k}_l + P_{il}\hat{k}_m\hat{k}_j)\langle T_{B(ij)}(\mathbf{k})T^*_{B(mn)}(\mathbf{k}')\rangle \end{aligned} \tag{4.101}$$

resulting in

$$(P_{jm}\hat{k}_i\hat{k}_l)\langle T_{B(ij)}(\mathbf{k})T^*_{B(mn)}(\mathbf{k}')\rangle \propto \left[(1+\beta^2)(1-\gamma^2) + \gamma\beta(\mu-\gamma\beta)\right], \tag{4.102}$$

$$(P_{il}\hat{k}_m\hat{k}_j)\langle T_{B(ij)}(\mathbf{k})T^*_{B(mn)}(\mathbf{k}')\rangle \propto \left[(1-\beta^2)(1+\gamma^2) + \gamma\beta(\mu-\gamma\beta)\right], \tag{4.103}$$

and our result is the sum of Eq.(4.102) and Eq.(4.103): $\left[(1+\beta^2)(1-\gamma^2) + \gamma\beta(\mu-\gamma\beta)\right] + \left[(1-\beta^2)(1+\gamma^2) + \gamma\beta(\mu-\gamma\beta)\right] = (1 - 2\gamma^2\beta^2 + \gamma\beta\mu)$, however, Planck [59] (Eq.10) and Paoletti [69] only counted Eq.(4.102) in their paper.

In summary, we have derived the full two-point correlations considering both non-helical and helical magnetic fields with no approximations assumed when evaluating the integrals. Our equations agree well with those in Kunze's paper. Our code is based on Shaw and Lewis's [63]. The CMB spectra computed using our code generally agree with those in Planck's papers [59], despite the difference with their equations mentioned above.

Chapter 5

Theoretical predictions for the PMF induced CMB

5.1 Magnetic patches for CAMB and CosmoMC

The are several publicly available codes that solve the Boltzmann equations and calculate the power spectra for various cosmological observables. We developed a patch[1] for the publicly available Boltzmann code CAMB [70] that allows one to calculate the PMF sourced CMB spectra. The main features are briefly summarized below.

We introduce the effects of the PMF into the Einstein and Boltzmann equations closely following the formalism of [63] and the associated code by Shaw and Lewis (SL). Among the notable improvements with respect to SL are making the code compatible with CosmoMC and extending the allowed range of the magnetic spectral index to values $n_S \geq -1.5$. The latter required recalculating the integrals involved in the correlation functions of the magnetic perturbations Δ_B and $\Pi_B^{(0,1,2)}$ with the upper integration bound taken to be k_D/k instead of ∞. We confirmed that, for $-3 < n_S < -1.5$, the integrals depend weakly on k_D/k. Since the k modes involved in the computation of the CMB power spectra are much smaller than the damping scale k_D, we computed the integrals in the approximate limit $k_D/k \to \infty$. For arbitrary n_S in that range, we interpolate on a grid of pre-computed integrals. For $n_S \geq -1.5$, the integrals depend strongly on the upper integration bound k_D/k. Since for arbitrary n_B and k the integrals involve hypergeometric functions, we sampled the integrals and computed a set of fitting functions for each correlation function as in [71].

We also have extended the latest version of the CosmoMC code [72] to include the contributions of the scalar, vector and tensor compensated and passive magnetic modes[2].

[1]The patch is publicly available at `https://github.com/scalby/MagCAMB`

[2]The patch is publicly available at `https://github.com/scalby/MagCOSMOMC`

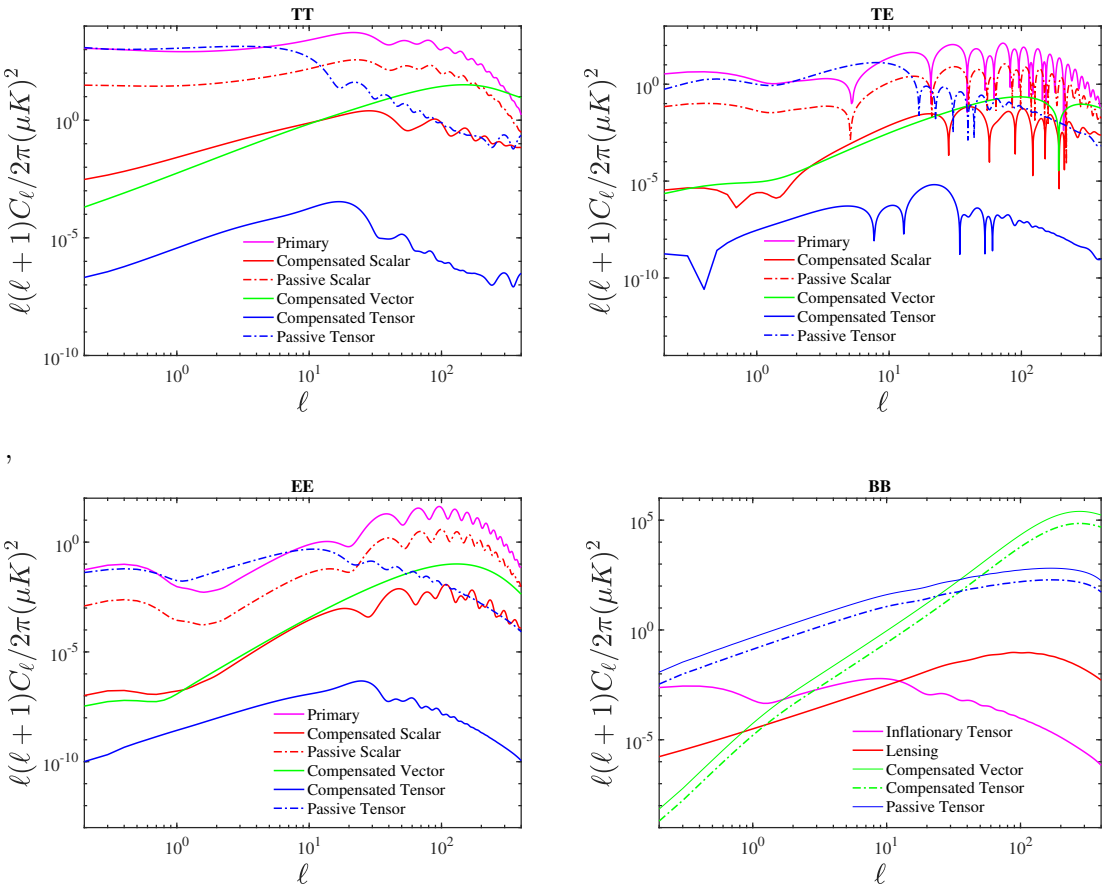

Figure 5.1: Contributions of relevant 'magnetic' modes to the CMB temperature and polarization power spectra for a non-helical PMF with $B_{1\mathrm{Mpc}} = 4.5\,\mathrm{nG}$ and $n_S = -2.9$. For the passive modes, the time of the generation of the PMF is set at $\eta_\nu/\eta_B = 10^{17}$. The cosmological parameters are set to $\omega_b = 0.022383$, $\omega_c = 0.12011$, $T_{\mathrm{CMB}} = 2.7255\,\mathrm{K}$, $h = 67.32$, $A_s = 2.1 \times 10^{-9}$, $n_s = 0.96605$, $r = 0.1$, $n_T = 1$.

5.2 Theoretical Results with Non-helical Magnetic field

In Fig. 5.1 we show the contributions of the non-helical magnetic field to the CMB spectra for a PMF with magnitude $B_{1\,\mathrm{Mpc}} = 4.5$ nG, spectral index $n_S = -2.9$ (nearly scale-invariant) and time ratio $\eta_\nu/\eta_B = 10^{17}$ corresponding to the PMF generation energy scale of 10^{14} GeV. We consider both passive and compensated initial conditions. This figure shows that the dominant contributions to the angular power spectra come from the passive scalar and compensated vector modes, and the passive tensor mode. Compensated tensor modes are too small to be noticed. Compared to the primary CMB spectra, the dominant contribution of magnetically-induced modes appears on small angular scales, where the primary CMB fluctuations are suppressed, because magnetically induced perturbations are not suppressed by Silk damping. When considering the passive tensor modes, the dominant contribution is on large angular scales.

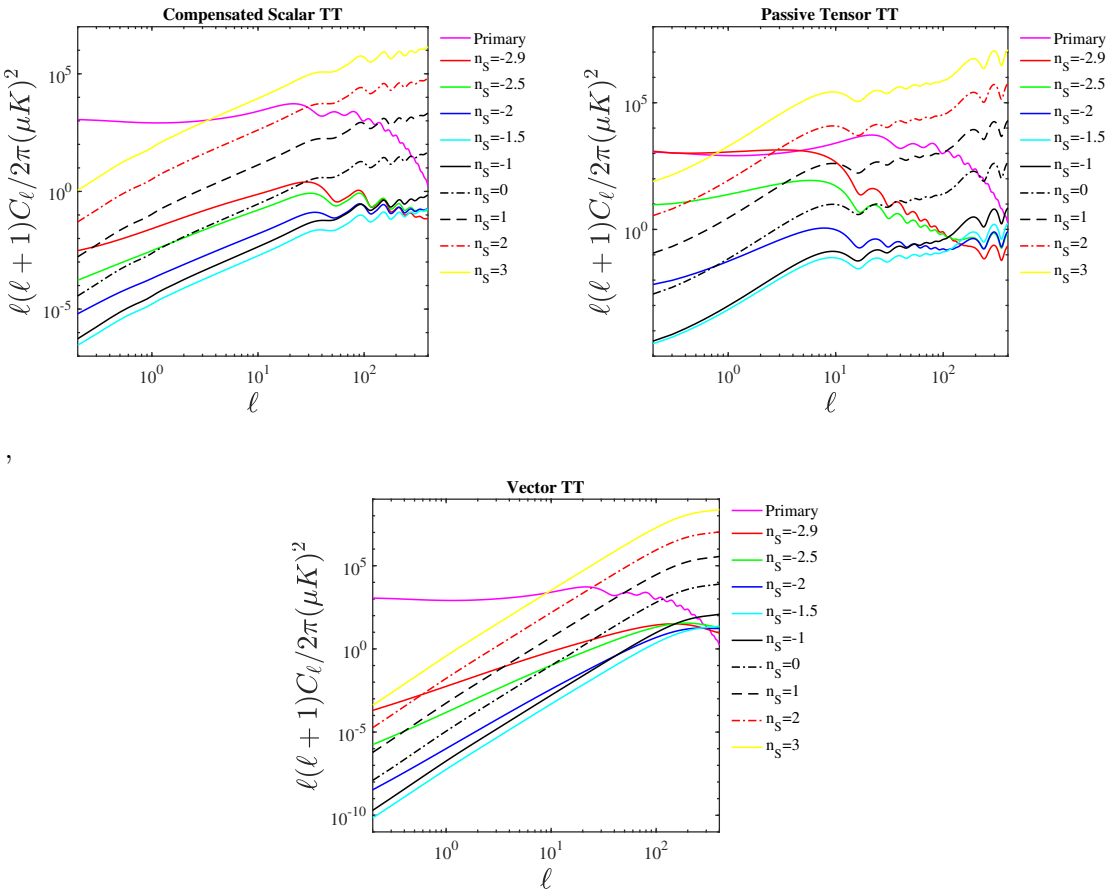

,

Figure 5.2: Contributions of different different spectral indices on the magnetic field induced CMB power spectra C_l^{TT}. A non-helical PMF with $B_{1\mathrm{Mpc}} = 4.5$, the time of the generation of the PMF is set at $\eta_\nu/\eta_B = 10^{17}$ for all plotted cases. The color 'magenta' lines show the primary CMB anisotropies. Top left: compensated scalar mode, top right: compensated vector mode, bottom: passive tensor mode.

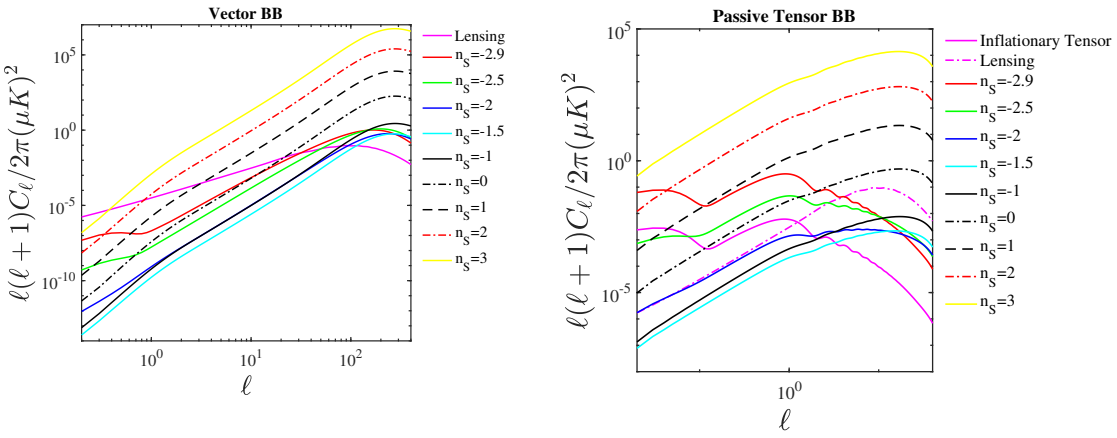

Figure 5.3: The B-mode spectrum from the PMF vector mode and passive tensor mode with $B_{1\,\mathrm{Mpc}} = 4.5\,\mathrm{nG}$ and different values of the spectral indices n_S. The time of the generation of the PMF is set at $\eta_\nu/\eta_B = 10^{17}$. The color 'magenta' lines show the inflationary tensor CMB anisotropies with $r = 0.1$ and lensing contributions. Left: compensated vector mode, right: passive tensor mode.

In Figs. 5.2 and 5.3 we present spectra for several different values of the spectral index n_S. The PMF energy momentum tensor components enter into the source term and affect the CMB power spectra. The shape of the magnetically-induced spectra strongly depends on the PMF spectral index. We can illustrate this dependence on the temperature power spectrum for scalar, vector and tensor perturbations. The qualitative change happens at $n_S = -1.5$. When changing the spectral index n_S in the range $-3 < n_S < -1.5$, the shape of the CMB spectra is changing with an increase in n_S leading to a shift of power from lower to higher ℓ. This reduces the CMB anisotropy power on scales within the observational window. In contrast, for $n_S > -1.5$, CMB spectra become cutoff dominated and scale as white noise, with the shape being practically independent of n_S. When $n_S > -1.5$, increasing the value of n_S leads to more CMB power for the same PMF strength on 1 Mpc scale.

The magnetically-induced passive tensor modes are not only determined by the amplitude and spectral index of the PMF but also depend on when the PMF is generated. Namely, the passive tensor mode sourced metric perturbation $P_h = \left[6R_\gamma \ln(\eta_\nu/\eta_B) + \left(\frac{5}{8R_\nu} - 1\right)\right]^2 \times \langle \Pi_B^{(\pm 2)*}\, \Pi_B^{(\pm 2)} \rangle$ depends on the time ratio η_ν/η_B. Depending on whether the fields were generated at the grand unification energy scale (GUT) or at a later phase transitions, this ratio may vary between 10^{17} and 10^6. In Fig. 5.4, we show how the time ratio and spectral index influence the shape and magnitude of the CMB power spectrum sourced by the passive tensor modes. For its dependence on the time ratio, we show the two extreme values of the possible range. It is obvious that increasing the time ratio leads to more CMB power for the same PMF strength on 1 Mpc scale.

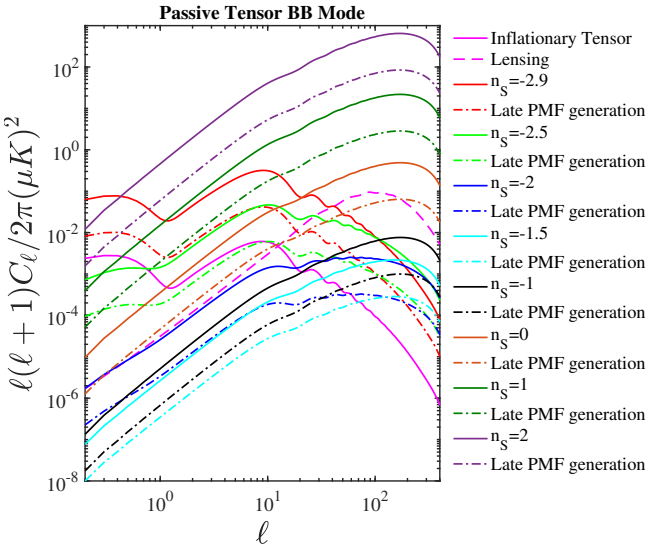

Figure 5.4: Comparison between the two extremes for the time ratio η_ν/η_B. The PMF induced B-mode spectrum due to passive tensor modes with $B_{1\,\mathrm{Mpc}} = 4.5\,\mathrm{nG}$ and different values of spectral indices n_S are shown. The PMF is generated at the GUT scale ($\eta_\nu/\eta_B = 10^{17}$, solid lines) and late times ($\eta_\nu/\eta_B = 10^6$, dash-dot lines). The solid 'magenta' line shows the primary tensor CMB anisotropies and the dash-dot 'magenta' line shows the lensing contributions.

5.3 Theoretical Results with Helical Magnetic field

We consider the maximally helical case, when $|S(k)| = |A(k)|$, $S_0 = |A_0|$, and $n_A = n_S$. The CMB spectra will be the sums of non-helical PMF contributions shown in the previous section and the contribution from the anti-symmetric part of the magnetic spectrum. As we will see, in most cases, the additional contributions to the sources due to helicity is small but negative, which makes the total contributions weaker. Magnetic helicity can produce the parity odd cross correlations between the E and B polarization anisotropies, as well as between temperature and B polarization anisotropies. These parity odd cross correlations are sourced by the mixed terms in the correlation function of the energy momentum tensor, proportional to $\langle \pi_B^{(+1)}(\mathbf{k})\pi_B^{(+1)*}(\mathbf{k}') - \pi_B^{(-1)}(\mathbf{k})\pi_B^{(-)*}(\mathbf{k}')\rangle$ for vector modes and $\langle \pi_B^{(+2)}(\mathbf{k})\pi_B^{(+2)*}(\mathbf{k}') - \pi_B^{(-2)}(\mathbf{k})\pi_B^{(-2)*}(\mathbf{k}')\rangle$ for tensor modes. In Fig. 5.5 we present the predictions for the PMF induced compensated and passive modes, adding the additional contributions to the sources due to helicity. We set the magnitude $B_{1\,\mathrm{Mpc}} = 4.5$ nG, spectral index $n_S = -2.9$ (scale invariant) and time ratio $\eta_\nu/\eta_B = 10^{17}$ corresponding to the PMF generation energy scale of 10^{14} GeV. We also show the TB and EB spectra for vector modes and the compensated and passive tensor modes in Fig. 5.6 with spectra index $n = -1$.

The shape of the magnetically-induced spectra strongly depends on the PMF spectral index. We show this dependence on TB and EB spectra for vector modes and passive tensor

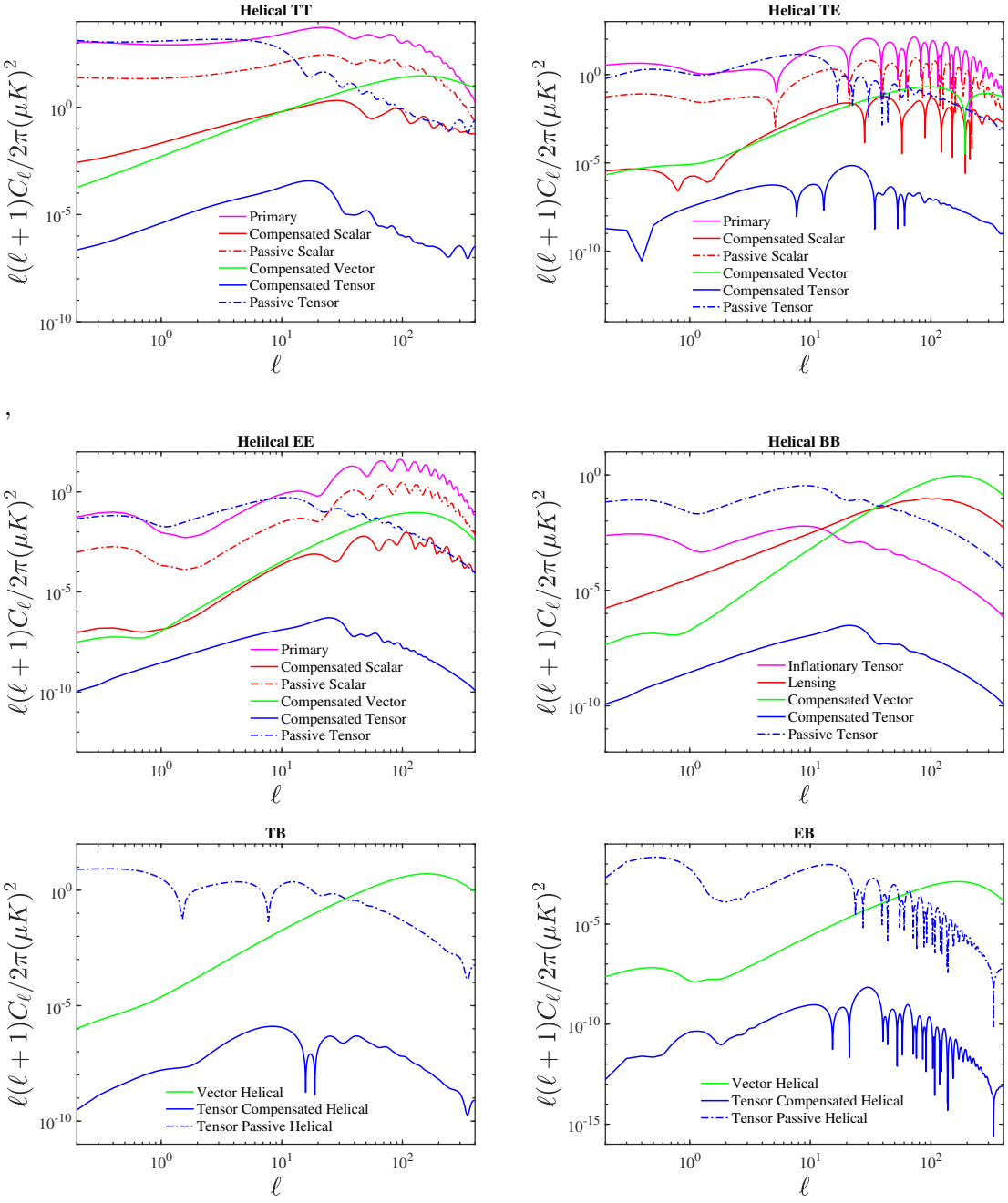

Figure 5.5: Contributions of relevant 'magnetic' modes to the CMB temperature and polarization power spectra for a maximum helical PMF with $B_{1\mathrm{Mpc}} = 4.5\,\mathrm{nG}$ and $n_S = n_A = -2.9$. For the passive modes, the time of the generation of PMF is set at $\eta_\nu/\eta_B = 10^{17}$. The cosmological parameters are set to $\omega_b = 0.022383$, $\omega_c = 0.12011$, $T_{\mathrm{CMB}} = 2.7255\,\mathrm{K}$, $h = 67.32$, $A_s = 2.1 \times 10^{-9}$, $n_s = 0.96605$, $r = 0.1$, $n_T = 1$. The parity odd C_ls: C_l^{TB} and C_l^{TB} due to the helicity of PMF are shown in the bottom.

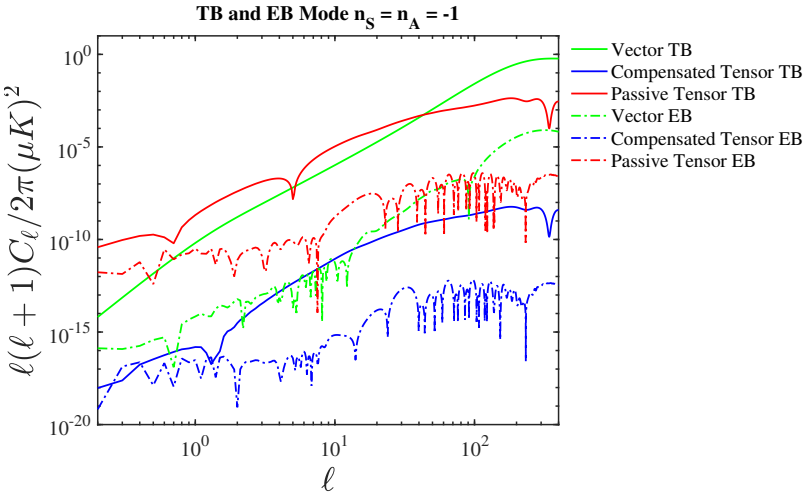

Figure 5.6: Helical magnetic field induced parity odd CMB cross-correlations C_l^{TB} and C_l^{EB}. We consider a maximum helical PMF with $B_{1\mathrm{Mpc}} = 5\,\mathrm{nG}$, and $n_S = n_A = -1$. The PMF is generated at the GUT scale ($\eta_\nu/\eta_B = 10^{17}$. Solid lines show TB, dash-dot lines show EB. Green lines are vector mode, red lines are passive tensor modes, blue lines are compensated tensor modes.

modes in Fig. 5.7, since the dependence of other spectra is similar to the case of non-helical fields. The qualitative change happened at $n_S = -1.5$ as before, which divides it into two regions. In Fig. 5.8 we show the dependence on the time ratio and PMF spectral index. The behavior is similar to the non-helical case.

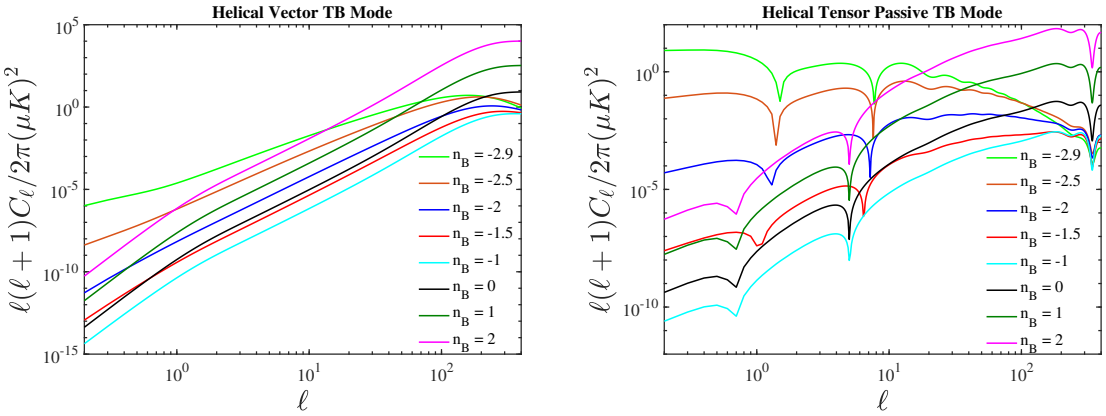

,

Figure 5.7: Contributions of different spectral indices on the magnetic field induced CMB power spectra C_l^{TB}. We consider a maximum helical PMF with $B_{1\mathrm{Mpc}} = 4.5$, and $n_S = n_A = -2.9$, the time of the generation of the PMF is set at $\eta_\nu/\eta_B = 10^{17}$. Left: compensated vector mode, right: passive tensor mode.

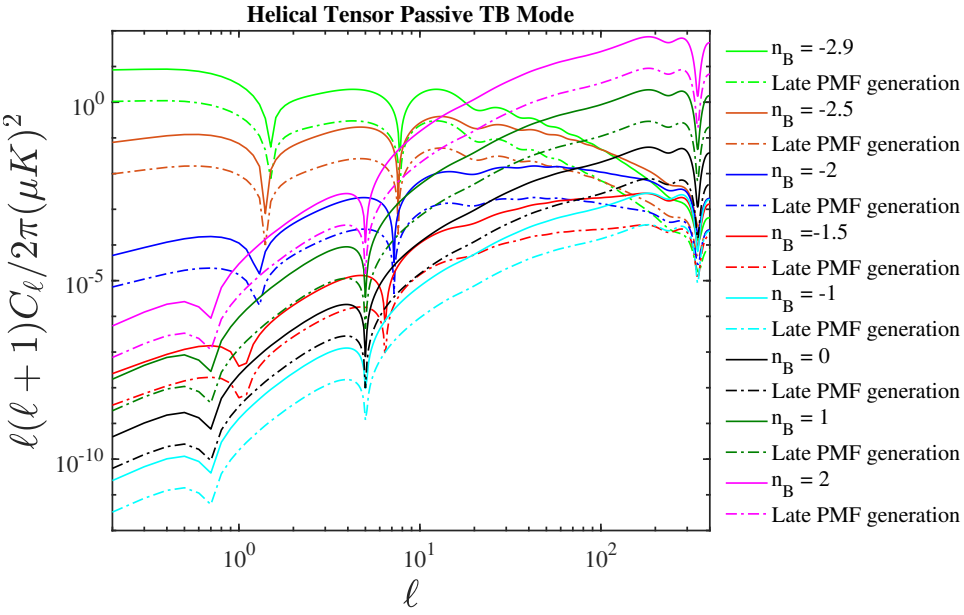

Figure 5.8: Contributions of different spectral indices on the magnetic field induced CMB power spectra C_l^{TB} and comparison between the two extremes for the time ratio η_ν/η_B. Considering the maximum helical PMF with $B_{1\mathrm{Mpc}} = 4.5$, and $n_S = n_A = -2.9$. The PMF is generated at the GUT scale ($\eta_\nu/\eta_B = 10^{17}$, solid lines) and late times ($\eta_\nu/\eta_B = 10^6$, dash-dot lines).

5.3.1 Comparison between non-helical and helical PMF results

In Figs. 5.9, 5.11, 5.10 and 5.12 we compare the CMB spectra induced by non-helical and helical PMFs. As a rule, there is no difference in the shape and the slope of the angular power spectra, but there is a shift in the amplitude. For the spectral index $n = -2.9$ (Fig. 5.9) the helical shift is much smaller than that for the spectral index $n = 2$ (Fig. 5.10).

Generally, as one can see from Fig. 5.12, the helical contribution are small for spectral indices $n < -1.5$. As one increases the spectral index, the helical contribution becomes more pronounced, and always has a negative effect, reducing the overall amplitude.

The compensated tensor modes are subdominant and can be ignored when we constrain the PMF. For the TT, TE and EE spectra, the dominant contribution comes from the scalar and vector compensated modes and the passive tensor modes. And scalar passive mode becomes relevant on large angular scales for the nearly scale-invariant $n = -2.9$ power spectra. The compensated vector modes dominate at small angular scales, but the passive tensor modes contribute at low and intermediate multipoles. For BB spectra, the passive tensor modes together with the compensated vector mode can be well constrained by the B-mode data.

The current and future CMB experiments capable of detecting the B modes from weak lensing can put a constraint on the magnetic vector mode contribution to the B mode

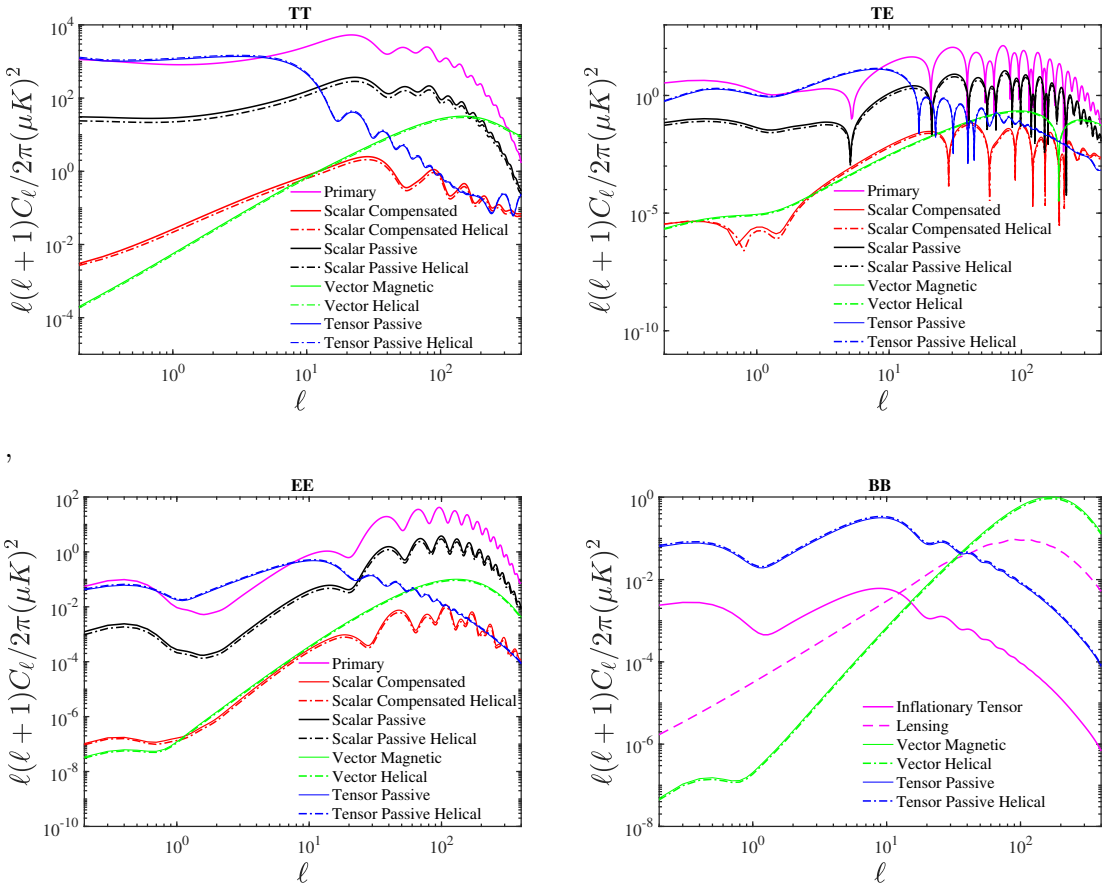

Figure 5.9: Comparison between CMB power spectra due to non-helical PMF and maximum helical PMF. We consider PMFs with $B_{1\mathrm{Mpc}} = 4.5\,\mathrm{nG}$ and $n_S = n_A = -2.9$. For the passive modes, the time of the generation of the PMF is set at $\eta_\nu/\eta_B = 10^{17}$. Solid lines are non-helical PMFs, dash-dotted lines are maximum helical PMFs. 'Red' and 'black' lines are scalar modes, 'green' lines are vector modes, 'blue' lines are tensor modes.

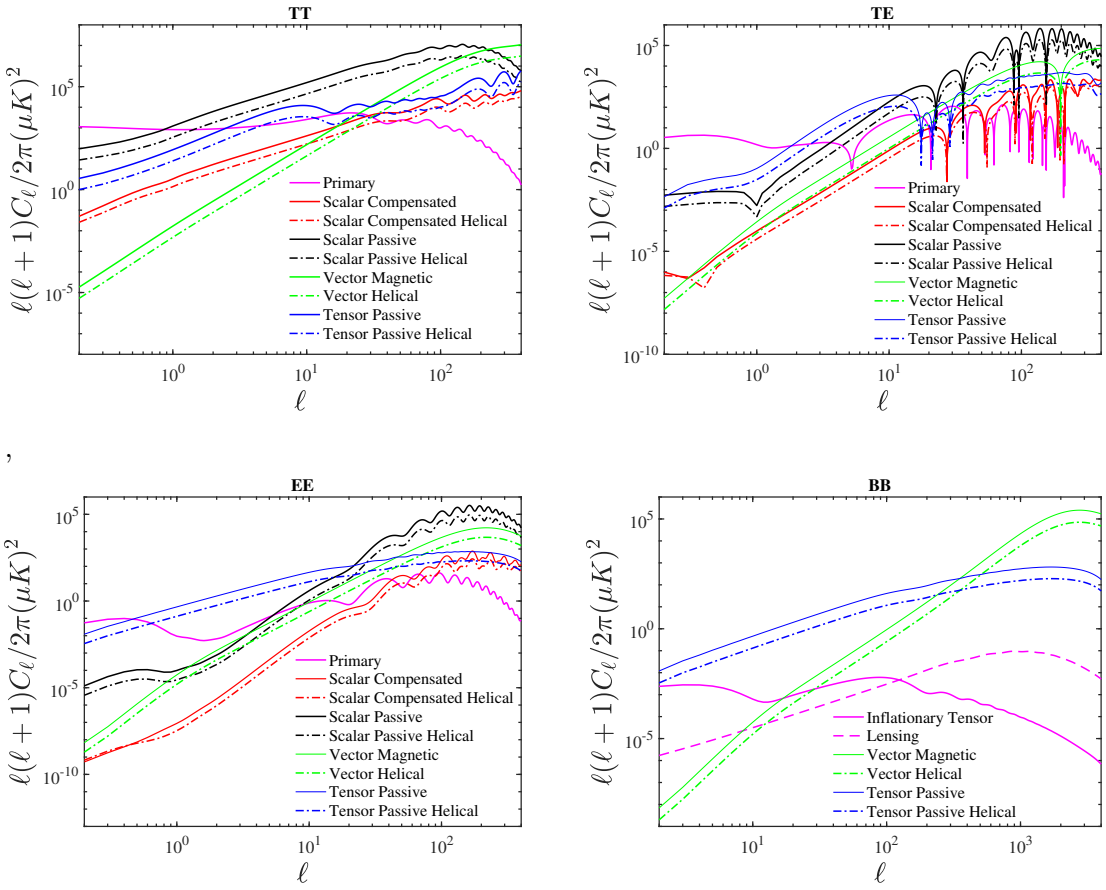

Figure 5.10: Comparison between CMB power spectra due to non-helical PMF and maximum helical PMF. We consider PMFs with $B_{1\mathrm{Mpc}} = 4.5\,\mathrm{nG}$ and $n_S = n_A = 2$. For the passive modes, the time of the generation of the PMF is set at $\eta_\nu/\eta_B = 10^{17}$. Solid lines are non-helical PMFs, dash-dotted lines are maximum helical PMFs. 'Red' and 'black' lines are scalar modes, 'green' lines are vector modes, 'blue' lines are tensor modes.

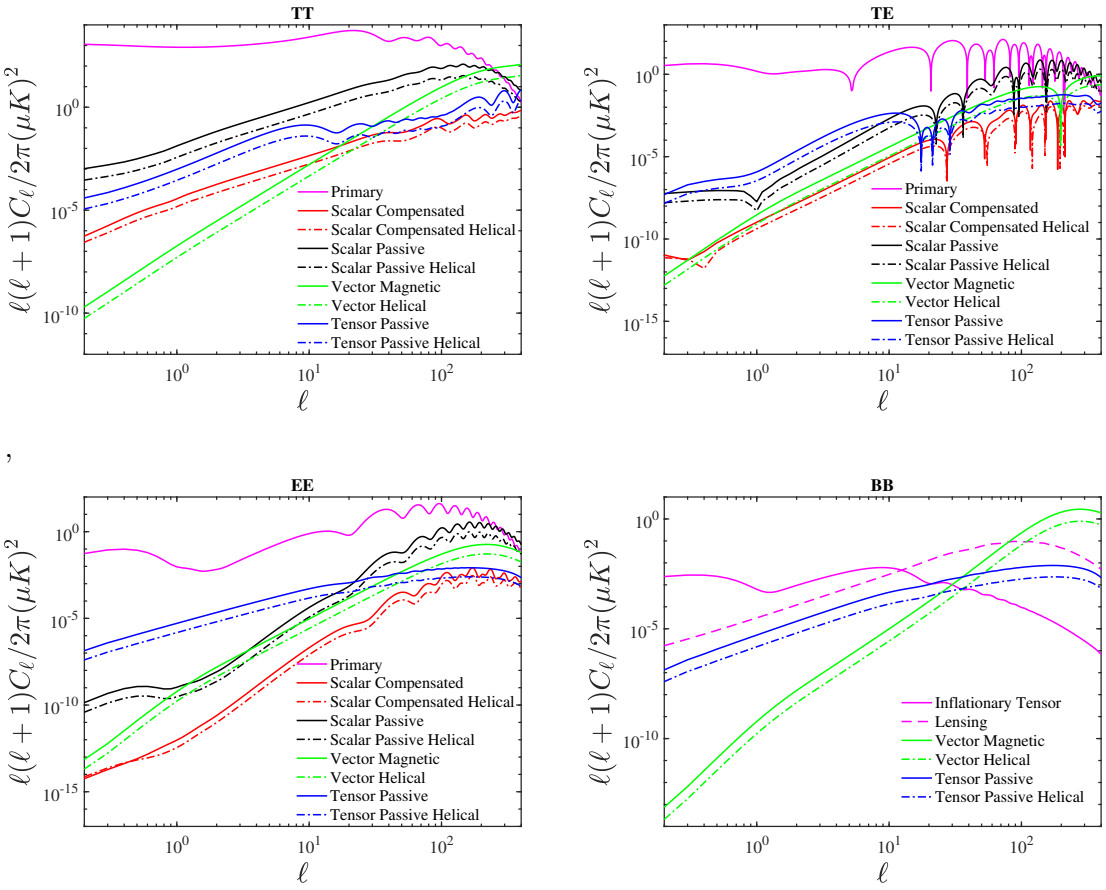

Figure 5.11: Comparison between CMB power spectra due to non-helical PMF and maximum helical PMF. We consider PMFs with $B_{1\mathrm{Mpc}} = 4.5\,\mathrm{nG}$ and $n_S = n_A = -1$. For the passive modes, the time of the generation of the PMF is set at $\eta_\nu/\eta_B = 10^{17}$. Solid lines are non-helical PMFs, dash-dotted lines are maximum helical PMFs. 'Red' and 'black' lines are scalar modes, 'green' lines are vector modes, 'blue' lines are tensor modes.

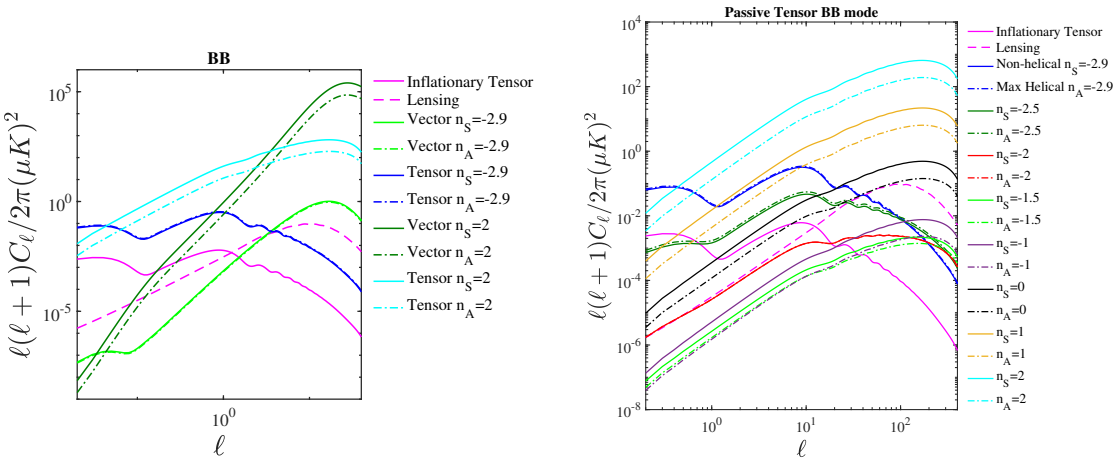

Figure 5.12: The B-mode spectrum from the maximum helical PMF with vector mode and tensor passive mode. Comparison between non-helical PMF and maximum helical PMF induced CMB power spectra at different values of spectral indices n. We consider PMFs with $B_{1\,\mathrm{Mpc}} = 4.5\,\mathrm{nG}$. The time of the generation of the PMF is set at $\eta_\nu/\eta_B = 10^{17}$. The color 'magenta' lines show the inflationary tensor $r = 0.1$ CMB anisotropies and dash-dotted 'magenta' lines show the lensing contributions. Left: compensated vector mode and passive tensor mode with two cases (spectral index $n = 2$ and $n = -2.9$), right: only passive tensor mode.

polarization power spectrum. As shown in Fig. 5.13, the large-ℓ measurements of the B-mode polarization performed by the SPT can place competitive bounds on the amplitude of the PMF. We show the new SPT bandpowers [1] and add the helical magnetic field with spectral index $n-2.9$ (expected from inflation) and $n = 2$ (expected from phase transitions) in Fig. 5.14 with different magnitudes of magnetic fields. We plot the sum of the vector compensated and the tensor passive mode. The PMF vector modes are relevant for large-ℓ, and the passive PMF tensor modes are relevant at small-ℓ. For the scale-invariant PMF the B-mode spectrum peaks around $l \sim 1700$, but for $n = 2$ the peak shifts to $l \sim 2750$. In the following section, we will use the SPT B-mode power spectrum data to derive constraint on the PMF after marginalizing over other parameters.

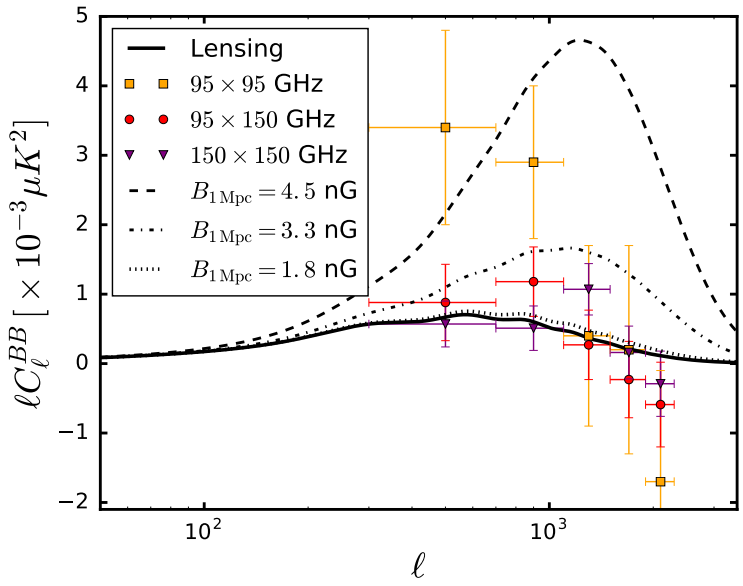

Figure 5.13: The B-mode spectrum from a scale-invariant non-helical PMF vector mode added to the lensing contribution (solid black line) for $B_{1\,\mathrm{Mpc}} = 4.5$ nG (dashed line), $B_{1\,\mathrm{Mpc}} = 3.3$ nG (dash-dotted line) and $B_{1\,\mathrm{Mpc}} = 1.8$ nG (dotted line). The three SPT bandpowers are shown in black, red and yellow.

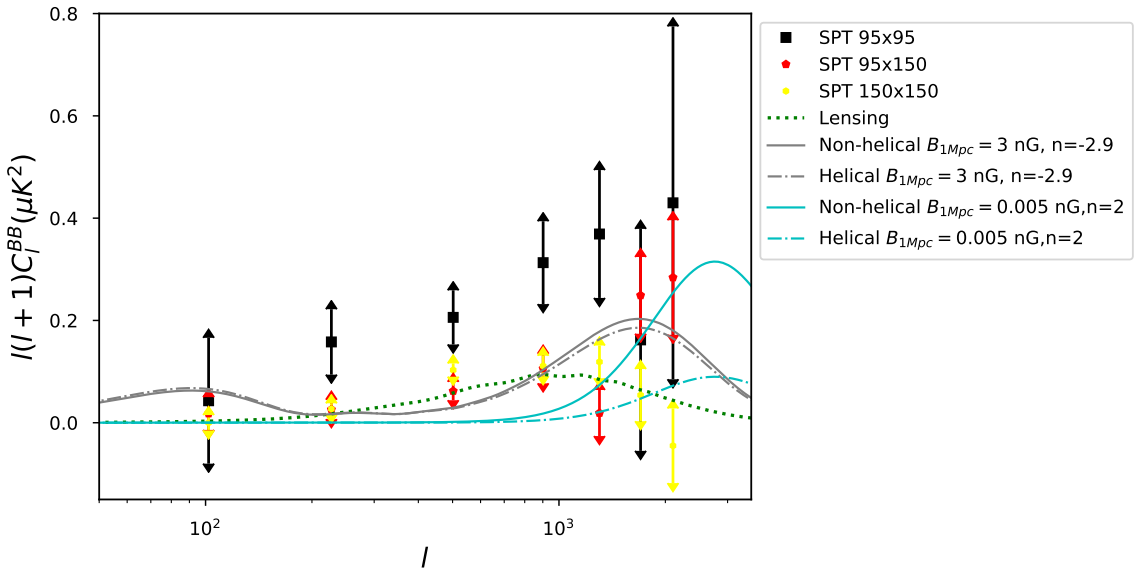

Figure 5.14: The B-mode polarization power spectrum is from a scale-invariant ($n_S = n_A = -2.9$) and GUT scale generated ($\eta_\nu/\eta_B = 10^{17}$) PMF. We show the sum of vector mode and tensor passive mode. Both non-helical (solid lines) and maximum helical (dash-dot lines) PMFs are present. Shown are $B_{1\,\mathrm{Mpc}} = 3$ nG (grey lines) with $n = -2.9$, $B_{1\,\mathrm{Mpc}} = 0.005$ nG (cyan lines) with $n = 2$. The three SPT[1] bandpowers are shown in black, red and yellow. The lensing contribution is shown in green dotted line.

Chapter 6

Bounds on non-helical PMF from current CMB data

In this Chapter, we use the measurements of the CMB anisotropies power spectra by the Planck satellite [73] and the 2015 CMB B-mode polarization spectra from the SPT [74] to constrain the amplitude, the spectral index and the generation time of the PMF.

For Planck, we use the joint TT, TE, EE and BB likelihood in the range $2 < \ell < 29$, denoted as LowTEB, together with the high-ℓ temperature likelihood in the range $30 < \ell < 2508$, simply denoted as TT. We also consider the case in which the TT likelihood is replaced with the joint TT, TE and EE polarization likelihood (denoted as TTTEEE). We also perform the analysis with and without using the likelihood from the BICEP2/Keck-Planck (BKP) cross correlation analysis [75].

The 2015 SPT likelihood [74] is a multivariate Gaussian likelihood and uses three bandpowers from the 95GHz $\times$ 95GHz, 95GHz $\times$ 150GHz and 150GHz $\times$ 150GHz spectra. It also takes into account the contributions to B-modes from the dust emission within our Galaxy and from the polarized emission from extragalactic sources. The dust emission is modelled according to Eq. (21) in [74] and is scaled by an overall dust emission amplitude $A_{\rm dust}$ [76]. The extragalactic sources are modelled through a constant C_l term with different amplitudes for each bandpower, $A_{\rm PS,95}$, $A_{\rm PS,95\times150}$ and $A_{\rm PS,150}$. These nuisance parameters are marginalized over using priors shown in Tabel 6.1. We have extended the SPT likelihood code to include the contributions of the PMF to the CMB B-modes.

Parameter	Prior	
$A_{\rm dust}$	$[0.0, 2.5]$	Gaussian
$A_{\rm PS,95}$	$[0.0, 4.0]$	flat
$A_{\rm PS,95\times150}$	$[0.0, 4.0]$	flat
$A_{\rm PS,150}$ ...	[0.04.0]	flat

Table 6.1: Priors on the nuisance parameters used in the 2015 SPT likelihood described in Sect. 6.2.

We assume a flat universe and, as in [59]. A non-zero neutrino mass would only enhance the power on large scales in a magnetic field induced spectrum, where the PMF contribution is less relevant [63]. Since neutrino mass would not affect the results very much, we restrict our analysis to three massless neutrinos. We also assume that the primary (inflationary) and the passive and compensated magnetic modes are uncorrelated, so that their contributions to the CMB spectra can be calculated separately and simply added as

$$C_\ell^{\rm theor} = C_\ell^{\rm prim} + C_\ell^{\rm pass} + C_\ell^{\rm comp}. \tag{6.1}$$

A scenario with correlated inflationary and magnetic modes has been discussed in [38] in a context of a specific model. We account for the effect of weak lensing by large scale structure on the primary mode only, and we marginalize over astrophysical residuals [59, 73].

The pivot Fourier number for the primary primordial spectrum is set to $k_* = 0.05{\rm Mpc}^{-1}$, while the magnetic smoothing scale is set to $\lambda = 1{\rm Mpc}$. We vary the baryon density $\omega_b = \Omega_b h^2$, the CDM density $\omega_c = \Omega_c h^2$, the reionization optical depth $\tau_{\rm reion}$, the ratio of the sound horizon to the angular diameter distance at decoupling θ, and the amplitude A_s and the spectral index n_s of the primary primordial spectrum of curvature perturbations. We also vary the additional magnetic parameters $B_{1{\rm Mpc}}$, n_S and $\beta = \log_{10}(\eta_\nu/\eta_B)$. The priors assumed on the parameters are given in Table 6.2.

Parameter	Flat Prior
ω_b	$[0.005, 0.1]$
ω_c	$[0.001, 0.99]$
$\tau_{\rm reion}$	$[0.01, 0.8]$
θ	$[0.5, 10]$
$\ln(10^{10} A_s)$	$[2, 4]$
n_s	$[0.8, 1.2]$
r	$[0, 2]$
$B_{1{\rm Mpc}}$	$[0, 10]$
$\log_{10}(B_{1{\rm Mpc}}/{\rm nG})$	$[-5, 1]$
$\log_{10}(\eta_\nu/\eta_B)$	$[4, 17]$
n_B	$[-2.9, 3]$

Table 6.2: Priors on the parameters varied in the MCMC analysis. We performed the analysis separately with the uniform and logarithmic priors on $B_{1{\rm Mpc}}$.

As can be seen from Fig. 5.1, for nearly scale-invariant PMFs, the passive tensor magnetic mode is similar in shape to the primary (inflationary) tensor mode, with an amplitude that depends on the time of the generation of the PMF, $\beta = \log_{10}(\eta_\nu/\eta_B)$. To address a potential degeneracy between the tensor-to-scalar ratio $r = A_T/A_s$ and β, we consider the cases with a fixed $r = 0$, as well as with co-varying the two parameters.

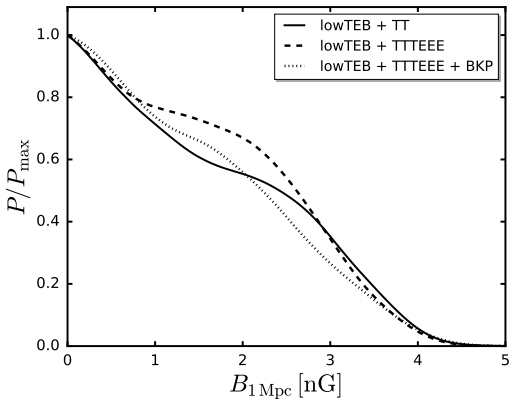

Figure 6.1: The probability distribution function for the magnetic amplitude $B_{1\,\rm Mpc}$ from the PLANCK data sets described in Sect. 6.1. We show only the case with $r = 0$ since varying r does not affect the results.

6.1 Constraints from Planck data

To derive constraints on the PMF from PLANCK, we use the PLANCK likelihood code described in detail in [73]. A thorough analysis has already been conducted by the PLANCK collaboration in [59]. Since scalar passive modes are not supposed to contribute significantly to the magnetic signals in the CMB (as shown in Chapter. 5), the authors of [59] included them only in the special case of a nearly scale invariant PMF with $n_B = -2.9$. Conversely, we include scalar passive modes in all of our analysis for the sake of completeness.

Fig. 6.1 shows the marginalized probability distribution function (PDF) for $B_{1\,\rm Mpc}$ derived from PLANCK data. The Figure only shows the case with $r = 0$, since the PDF in the case of co-varied r was essentially the same. The 95% CL bounds on $B_{1\,\rm Mpc}$ are summarized in Tab. 6.3, including the case with co-varied r.

Data sets	$B_{1\,\rm Mpc}$/nG
LOWTEB + TT, $r = 0$	< 3.3
LOWTEB + TT, r free	< 3.3
LOWTEB + TTTEEE, $r = 0$	< 3.2
LOWTEB + TTTEEE, r free	< 3.2
LOWTEB + TTTEEE + BKP, $r = 0$	< 3.3
LOWTEB + TTTEEE + BKP, r free	< 3.3

Table 6.3: Upper bounds (95% CL) for the PMF amplitude $B_{1\,\rm Mpc}$ obtained from the combination of PLANCK data sets described in Sect. 6.1. The magnetic spectral index n_B and the PMF generation epoch parameter β are unconstrained.

The magnetic spectral index n_B and the PMF generation epoch parameter β are unconstrained. We discuss these parameters in more detail in the next subsection.

6.2 Constraints from Planck combined with the 2015 SPT B-modes

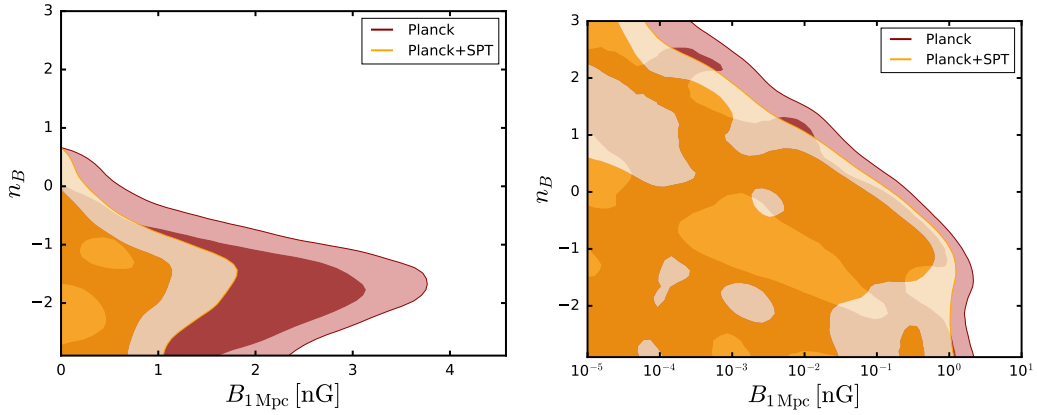

Figure 6.2: Left panel: the joint probability for the magnetic amplitude $B_{1\,\mathrm{Mpc}}$ and the magnetic index n_B using uniform prior on $B_{1\,\mathrm{Mpc}}$. Right panel: the joint probability for $B_{1\,\mathrm{Mpc}}$ and n_B using uniform prior on $\log_{10}(B_{1\,\mathrm{Mpc}}/\mathrm{nG})$. The two shaded regions represent the 68%C.L. and 95% C.L. respectively. The apparent bound on n_B in the left panel disappears when using the logarithmic prior, as shown in the right panel.

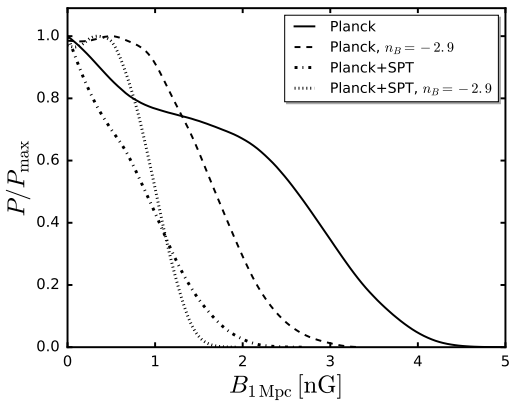

Figure 6.3: The marginalized PDFs for the magnetic amplitude $B_{1\,\mathrm{Mpc}}$ from Planck and the combination of Planck and SPT. We only show the PDFs obtained with $r = 0$, as the case with co-varying r is essentially the same. We also show the PDFs for the nearly scale-invariant case, $n_B = -2.9$.

Combining Planck with the B-mode polarization spectrum from SPT significantly tightens the bounds on the PMF, because of the contribution of the PMF vector modes, as illustrated in Fig. 5.13. We perform the analysis using the 2015 SPT likelihood and the Planck lowTEB and TTTEEE likelihoods, referring to the combination of them as Planck for simplicity. We do not include the BKP data, after the analysis in the previous subsection confirmed that it does not affect the bounds on the PMF.

In Fig. 6.2, we show the joint probability for the magnetic amplitude $B_{1\,\mathrm{Mpc}}$ and the magnetic index n_B from Planck alone and after combining PLANCK with SPT. The two parameters are correlated, with the bound on $B_{1\,\mathrm{Mpc}}$ becoming weaker with increasing n_B in the $-3 < n_B < -1.5$ range, and stronger for $n_S > -1.5$. This is due the qualitative change in the dependence of the CMB spectra on the magnetic power spectrum that occurs at $n_S = -1.5$. Namely, as illustrated in Fig. 5.1, an increase in n_B results in a shift of power from lower to higher ℓ, reducing the CMB power on scales inside the observational window and thus allowing for larger PMF strengths. In contrast, for $n_B > -1.5$, the shapes of the CMB spectra are cutoff dominated, with larger n_B resulting in more CMB power for the same PMF strength on 1 Mpc scale, leading to tighter constraints on $B_{1\,\mathrm{Mpc}}$.

Fig. 6.2 separately shows the cases with a uniform (left panel) and the logarithmic (right panel) priors on $B_{1\,\mathrm{Mpc}}$. As expected, the apparent upper bound on n_B, present in the case of the uniform prior and also observed in [59], is not physical and disappears in the case of the logarithmic prior. Indeed, there cannot be a bound on the spectral index of the PMF spectrum without a positive detection of the amplitude. The PDFs for the amplitude $B_{1\,\mathrm{Mpc}}$, after marginalizing over n_B, are shown in Fig. 6.3.

Two values of n_B are of particular theoretical interest. The first and simplest models of inflationary magnetogenesis predict a nearly scale-invariant PMF with $n_B \approx -3$. The combined bound from PLANCK and SPT on the nearly scale-invariant PMF ($n_B = -2.9$)[1] is $B_{1\,\mathrm{Mpc}} \approx B_{\mathrm{eff}} < 1.2$ nG at 95% CL. The corresponding bound from PLANCK alone is 2.0 nG, in agreement with [59].

The PMFs generated in post-inflationary phase transitions have small coherence lengths and are uncorrelated on cosmological scales. Causality forces the spectra of such fields to have $n_B = 2$ on scales of relevance to CMB anisotropies [61]. For such fields, we find $B_{1\,\mathrm{Mpc}} < 0.002$ nG at 95% CL. However, since most of the power of the causally generated PMFs is concentrated near the cutoff scale $2\pi/k_D \ll 1$Mpc, using $B_{1\,\mathrm{Mpc}}$ to quantify their amplitude can be misleading. Instead, it is more appropriate to use $\Omega_{B\gamma}$ or B_{eff}, which are representative of the total PMF energy density [26, 77]. The effective magnetic field amplitude B_{eff} is related to energy density and power spectrum by $B_{\mathrm{eff}} \equiv (2\mathcal{E}_B)^{1/2} = \frac{B_\lambda (k_D \lambda)^{\frac{n_B+3}{2}}}{\sqrt{\Gamma\left(\frac{n_B+5}{2}\right)}} = 3.3 \times 10^3 \sqrt{\Omega_{B\gamma}}\,\mathrm{nG}$. And $\Omega_{B\gamma} = \mathcal{E}_B/\rho_\gamma$. We derive $\Omega_{B\gamma} < 10^{-3}$ or $B_{\mathrm{eff}} < 100$ nG at 95% CL. For reference, the Big Bang Nucleosynthesis constrains the magnetic fraction to be $\Omega_{B\gamma} \lesssim 0.1$ [40].

Constraints on the PMF strength after marginalizing over n_B, as well as for the two special cases of theoretical interest, are summarized in Table 6.4. With respect to the case where

[1]To avoid divergent integrals, we restrict our analysis to $n_B \geq -2.9$. We also note that the dependence on the smoothing scale disappears and $B_{1\,\mathrm{Mpc}} = B_{\mathrm{eff}}$ for scale-invariant fields.

	$B_{1\,\mathrm{Mpc}}$/nG	B_{eff}/nG	$\Omega_{B\gamma}$
n_B marginalized	< 1.5	n/a	n/a
$n_B = -2.9$	< 1.2	< 1.2	$< 1.4 \times 10^{-7}$
$n_B = 2$	< 0.002	< 100	$< 10^{-3}$

Table 6.4: Upper bounds (95% CL) on the PMF amplitude $B_{1\,\mathrm{Mpc}}$, the effective PMF strength B_{eff} and the magnetic density fraction $\Omega_{B\gamma}$ obtained from PLANCK and SPT.

the spectral index is a free variable, the cases with fixed spectral index can put stronger constraints on the PMF amplitude, because one of the two parameters describing the PMF is fixed.

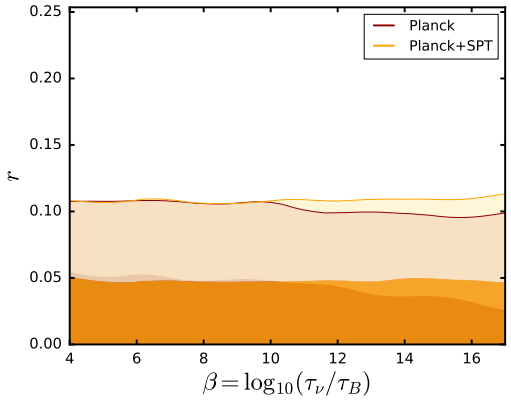

Figure 6.4: The joint probability for the scalar to tensor ratio r and the time of generation of the PMF $\log_{10}(\tau_\nu/\tau_B)$. The two shaded regions represent the 68%CL and 95% CL, respectively.

The joint probabilities for r and $\beta = \log_{10}(\tau_\nu/\tau_B)$, after marginalizing over other parameters, are shown in Fig. 6.4. It is evident that there is no degeneracy between them and that the time of the generation of the PMF is not constrained by data. This is because the contribution of the passive scalar and tensor modes to TT, TE and EE are too small even for the maximum allowed value of $\beta = 17$. As one can see from Fig. 5.1, the passive tensor mode is comparable in amplitude to the primary TT at low ℓ when $B_{1\,\mathrm{Mpc}} = 4.5$ nG and $\beta = 17$. For smaller values of β, even higher PMF strengths would be required for the passive tensor mode to be relevant. Such high values of PMF are not allowed because of the PMF vector mode contribution to TT at high ℓ. Any remaining weak sensitivity to β is further diluted by degeneracies with A_s, n_s and τ_{reion}. Thus, the passive tensor mode contribution to TT at low ℓ is irrelevant for the strengths of PMF allowed by TT at high ℓ. The scalar passive mode is even less irrelevant, as evident from Fig. 5.1. Note that adding the BPK B-mode data does not make a big difference because of large uncertainties at ℓ where the contribution from the passive tensor mode is prominent. Adding the SPT data does not help in constraining β either, because SPT only constrains the vector mode con-

tribution to BB and does not add information on scales relevant to the passive tensor mode.

Chapter 7

Bounds on a Helical PMF from current CMB data

Here we present the constraints from Planck on helical and non-helical PMFs. The set up used to derive the bound on a helical PMF is the same as the non-helical case, which is discussed in the previous chapter. We assume a flat universe and, as in [59], restrict our analysis to three massless neutrinos. The pivot Fourier number for the primary primordial spectrum is set to $k_* = 0.05\text{Mpc}^{-1}$, while the magnetic smoothing scale is set to $\lambda = 1\text{Mpc}$. We also assume that the primary (inflationary) and the passive and compensated magnetic modes are uncorrelated, so that their contributions to the CMB spectra can be calculated separately and simply added as

$$C_\ell^{\text{theor}} = C_\ell^{\text{prim}} + C_\ell^{\text{pass scalar}} + + C_\ell^{\text{pass tensor}} + C_\ell^{\text{comp scalar}} + C_\ell^{\text{comp vector}}, \qquad (7.1)$$

where we include the passive scalar mode, passive tensor mode, compensated scalar mode and the compensated vector mode. The compensated tensor mode is ignored because it is subdominant. According to Figure 3 of [78], the presence of PMFs does not significantly affect the the marginalized posteriors of the standard ΛCDM parameters. Thus, we fixed most of the parameters and varied the amplitude A_s and the spectral index n_s of the primary primordial spectrum of curvature perturbations. We also vary the additional magnetic parameters $B_{1\text{Mpc}}$, and $\beta = \log_{10}(\eta_\nu/\eta_B)$, and consider set discrete values of spectral indices. We assume a maximally helical field with $n_S = n_A = n_B$. The priors assumed for the parameters are given in Table 7.1.

7.1 Constraints from Planck data

We use the 2015 Planck likelihood code described in detail in [73] and perform a MCMC analysis, including the maximally helical contribution. We restrict our analysis to the case of temperature and polarization with only even cross-correlations. We do not include odd

Parameter	Flat Prior
ω_b	0.0224
ω_c	0.1196
$\tau_{\rm reion}$	0.0535
θ	1.04096
$\ln(10^{10}A_s)$ ..	$[2, 4]$
n_s	$[0.8, 1.2]$
r	0
$B_{\rm 1Mpc}$	$[0, 10]$
$\log_{10}(\eta_\nu/\eta_B)$	$[4, 17]$
n_B	$-2.9, 2.5, -2, -1.5, -1, 0, 1, 2, 3$

Table 7.1: Priors on the parameters varied in the MCMC analysis.

parity cross-correlators in our analysis because the odd parity cross-correlations TB and EB are present only for very low multipoles (large angular scales), where the signal from helical PMFs is negligible.

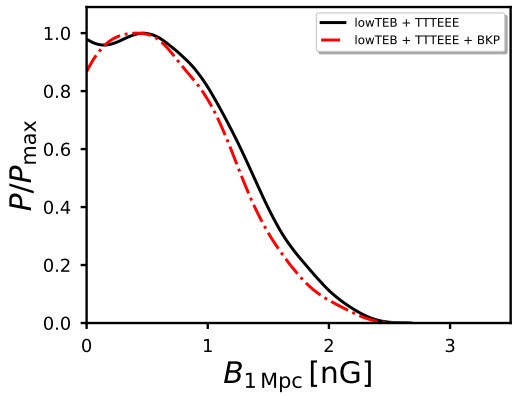

Figure 7.1: The probability distribution function for the magnetic amplitude $B_{1\,\rm Mpc}$ from the Planck data sets described in Sect. 7.1. The magnetic spectral index $n_B = -2.9$. We show only the case with $r = 0$ since varying r does not affect the results.

Data sets	$B_{1\,\rm Mpc}$/nG
LowTEB + TTTEEE, $r = 0$	< 1.7
LowTEB + TTTEEE + BKP, $r = 0$	< 1.6

Table 7.2: Upper bounds (95% CL) for the maximal helical PMF amplitude $B_{1\,\rm Mpc}$ obtained from the combination of Planck data sets described in Sect. 7.1. The magnetic spectral index $n_B = -2.9$, and the PMF generation epoch parameter β are unconstrained.

Fig. 7.1 shows the marginalized probability distribution for $B_{1\,\rm Mpc}$ in the case of a nearly scale-invariant PMF derived from Planck LowTEB, TTTEEE likelihood and Planck LowTEB, TTTEEE including the BKP data. The 95% CL bounds on $B_{1\,\rm Mpc}$ are summarized in Tab. 7.2, which shows that the inclusion of the BKP data leads to

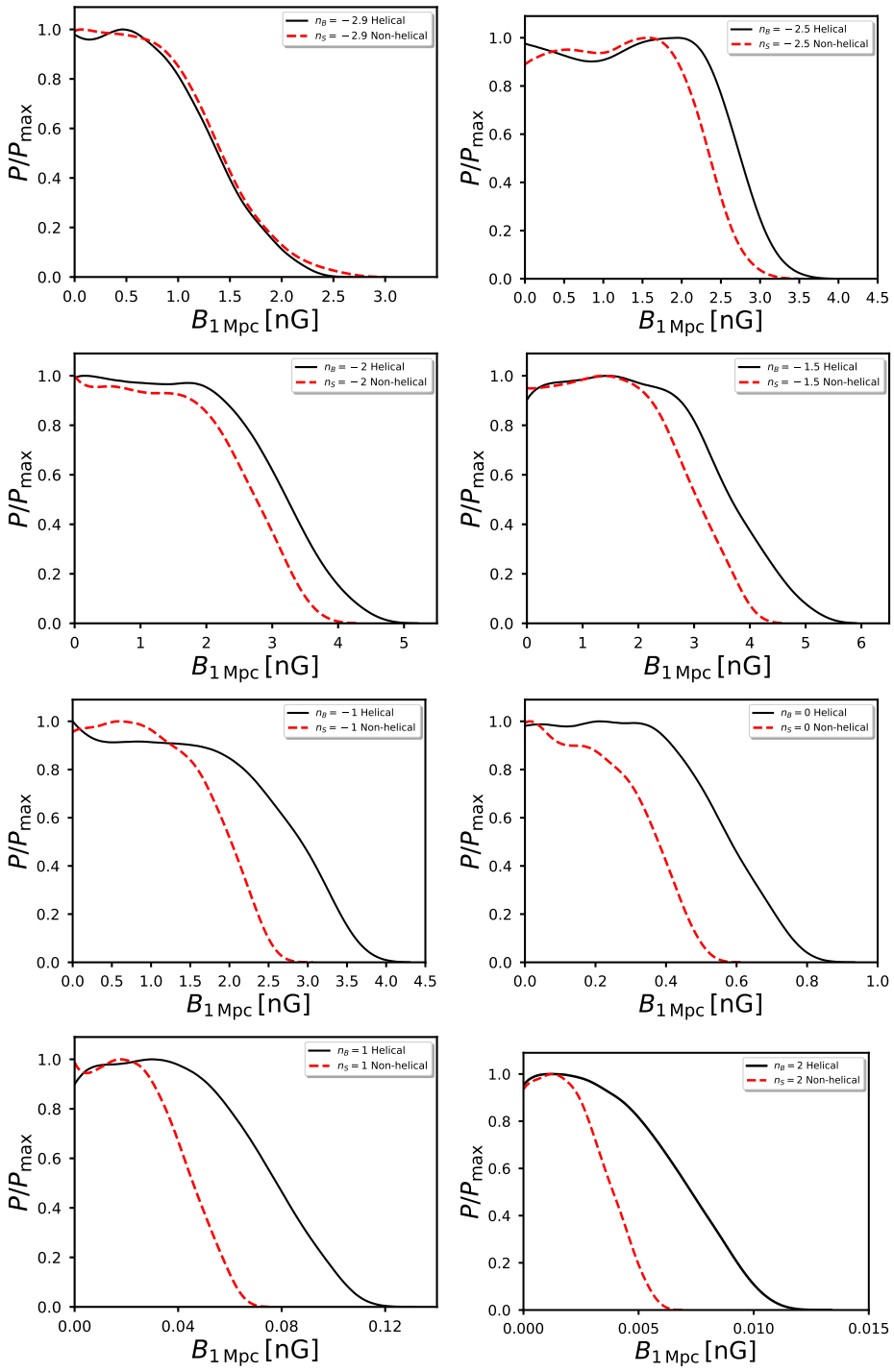

Figure 7.2: The probability distribution function for the magnetic amplitude $B_{1\,\mathrm{Mpc}}$ from the PLANCK data sets described in Sect. 7.1. We show only the case with $r = 0$ since varying r does not affect the results. For PLANCK, we use the PLANCK likelihood LowTEB, TTTEEE. We show the constraints from different spectral indices. Black lines show the helical PMF, red dashed lines show the non-helical PMF.

a slightly stronger constraint than the PLANCK LOWTEB, TTTEEE likelihood alone. Fig. 7.2 shows the marginalized probability distribution function for $B_{1\,\mathrm{Mpc}}$ for several fixed spectral indices (we choose a grid of values covering the full relevant range). This Figure only shows the case with $r = 0$, since the PDF in the case of co-varied r was essentially the same. The PMF generation epoch parameter β are unconstrained. The Figure compares the bounds on the PMF amplitude $B_{1\,\mathrm{Mpc}}$ in the maximally helical case and the non-helical case for each fixed spectral index, with the results summarized in Table. 7.4 and Table. 7.3. The analysis with the Planck LowTEB, TTTEEE likelihood in the helical case is in Table. 7.4. We observe that the inclusion of helicity tends to weaken the constraint on $B_{1\,\mathrm{Mpc}}$ when comparing with Table. 7.3. As discussed in Chapter. 5 (see Figs. 5.10, 5.11, 5.12) the magnetic fields with a maximal helicity component produce less CMB fluctuations in both temperature and polarization than non-helical PMFs of the same strength. As a result of this, the amplitude of a maximally helical magnetic fields are less constrained than non-helical fields for this Planck 2015 data release. However, this effect is negligible for a nearly scale-invariant PMF. Namely, for $n_B = -2.9$, the bound is 1.7 nG with a helical PMF and 1.8 nG with a non-helical PMF. This is the only case when helical PMF has a stronger constrain than the non-helical case. This can be explained by the Figure. 5.9, helical passive tensor modes are greater than the corresponding non-helical case, and the passive tensor modes is the primary magnetic contribution to the CMB power spectra for a nearly scale-invariant PMF power spectra.

As expected from the spectral index's impact on the angular power spectrum (Figure. 5.2), the constraint is weakest for $n_B = -1.5$. The bound on $B_{1\,\mathrm{Mpc}}$ becomes weaker with increasing n_B in the $-3 < n_B < -1.5$ range, and stronger for $n_B > -1.5$. The trend of the results with fixed spectral indices is in agreement with the dependence on the spectral index seen in the plots in Figure. 5.12, which show the qualitative change in the dependence of the CMB spectra on the magnetic power spectrum that occurs at $n_B = -1.5$. Namely, as illustrated in Fig. 5.1, an increase in n_B results in a shift of power from lower to higher ℓ, reducing the CMB power on scales inside the observational window and thus allowing for larger PMF strengths. In contrast, for $n_B > -1.5$, the shapes of the CMB spectra are cutoff dominated, with larger n_B resulting in more CMB power for the same PMF strength on 1 Mpc scale, leading to tighter constraints on $B_{1\,\mathrm{Mpc}}$.

7.2 Constraints from Planck combined with the SPT

Combining PLANCK with the B-mode polarization spectrum from SPT significantly tightens the bounds on the PMF, because of the contribution of the PMF vector modes, as illustrated in Fig. 5.14 and Fig. 7.4. We perform the analysis using the 2015 SPT likelihood and the PLANCK LOWTEB and TTTEEE likelihoods, referring to the combination of them as

	$B_{1\,\mathrm{Mpc}}$/nG (68% limits)	$B_{1\,\mathrm{Mpc}}$/nG (95% limits)	$B_{1\,\mathrm{Mpc}}$/nG (99% limits)
$n_B = -2.9$	< 1.0	< 1.8	< 2.2
$n_B = -2.5$	n/a	< 2.4	< 2.7
$n_B = -2$	< 1.9	< 3.0	< 3.4
$n_B = -1.5$	< 2.1	< 3.3	< 3.7
$n_B = -1$	< 1.4	< 2.1	< 2.4
$n_B = 0$	< 0.26	< 0.42	< 0.48
$n_B = 1$	< 0.032	< 0.052	< 0.060
$n_B = 2$	< 0.0027	< 0.0046	< 0.0053

Table 7.3: Upper bounds (99% CL, 95% CL, 68% CL) on the non-helical PMF amplitude $B_{1\,\mathrm{Mpc}}$ obtained from Planck LowTEB, TTTEEE likelihood.

	$B_{1\,\mathrm{Mpc}}$/nG (68% limits)	$B_{1\,\mathrm{Mpc}}$/nG (95% limits)	$B_{1\,\mathrm{Mpc}}$/nG (99% limits)
$n_B = -2.9$	< 0.99	< 1.7	< 2.1
$n_B = -2.5$	< 1.9	< 2.7	< 3.1
$n_B = -2$	< 2.2	< 3.5	< 4.1
$n_B = -1.5$	n/a	< 4.1	< 4.7
$n_B = -1$	< 2.0	< 3.1	< 3.4
$n_B = 0$	< 0.40	< 0.64	< 0.72
$n_B = 1$	< 0.054	< 0.087	< 0.10
$n_B = 2$	< 0.0051	< 0.0085	< 0.0099

Table 7.4: Upper bounds (99% CL, 95% CL, 68% CL) on the helical PMF amplitude $B_{1\,\mathrm{Mpc}}$ obtained from Planck LowTEB, TTTEEE likelihood.

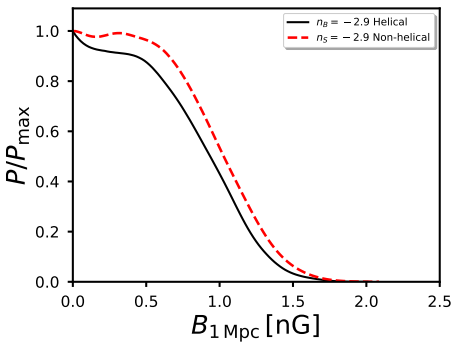

Figure 7.3: The probability distribution function for the magnetic amplitude $B_{1\,\mathrm{Mpc}}$ from the combination of Planck and SPT. We show only the case with $r = 0$ since varying r does not affect the results. For Planck, we use the Planck likelihood LowTEB, TTTEEE. We show the constraints from different spectral indices. Black lines show the helical PMF, red dashed lines show the non-helical PMF.

Parameter	Prior	
A_{dust}	$[0.0, 2.5]$	Gaussian
$A_{\mathrm{PS},95}$	$[0.0, 4.0]$	flat
$A_{\mathrm{PS},95\times150}$	$[0.0, 4.0]$	flat
$A_{\mathrm{PS},150}$ ...	$[0.04.0]$	flat

Table 7.5: Priors on the nuisance parameters used in the SPT.

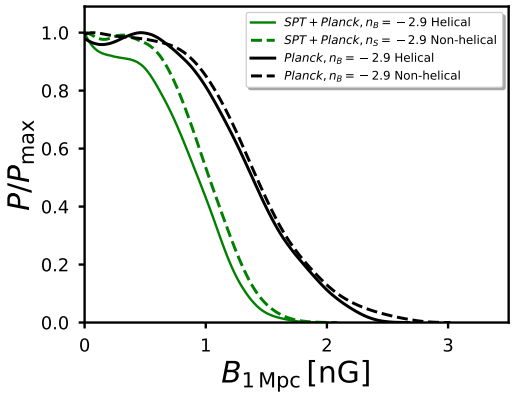

Figure 7.4: The marginalized PDFs for the magnetic amplitude $B_{1\,\rm Mpc}$ from PLANCK and the combination of PLANCK and SPT. We only show the PDFs obtained with $r = 0$, as the case with co-varying r is essentially the same. We show the PDFs for the nearly scale-invariant case, $n_B = -2.9$ for both helical and non-helical PMFs.

PLANCK for simplicity. The PDFs for the amplitude $B_{1\,\rm Mpc}$, with specific spectral index n_B, are shown in Fig. 7.4 and Fig. 7.3.

We consider two cases of interest, the almost scale invariant fields with $n_B = -2.9$ and the PMFs generated in post-inflationary phase transitions $n_B = 2$. For $n_B = -2.9$, we obtain $B_{1\,\rm Mpc} \approx B_{\rm eff} < 1.2$ nG at 95% CL for a non-helical PMF. Considering a helical PMF, we obtain a stronger bound $B_{1\,\rm Mpc} \approx B_{\rm eff} < 1.1$ nG at 95% CL. The corresponding bound from PLANCK alone is 1.7 nG, in agreement with [59].

The PMFs generated in post-inflationary phase transitions have small coherence lengths and are uncorrelated on cosmological scales. Causality forces the spectra of such fields to have $n_B = 2$ on scales of relevance to CMB anisotropies [61]. For such fields, we find $B_{1\,\rm Mpc} < 0.002$ nG at 95% CL for a non-helical PMF. However, since most of the power of the causally generated PMFs is concentrated near the cutoff scale $2\pi/k_D \ll 1$Mpc, using $B_{1\,\rm Mpc}$ to quantify their amplitude can be misleading. Instead, it is more appropriate to use $\Omega_{B\gamma}$ or $B_{\rm eff}$, which are representative of the total PMF energy density. We derive $\Omega_{B\gamma} < 10^{-3}$ or $B_{\rm eff} < 100$ nG at 95% CL. When considering helicity, the constraint weakens. we obtain $B_{1\,\rm Mpc} < 0.009$ nG at 95% CL, $\Omega_{B\gamma} < 10^{-3}$ or $B_{\rm eff} < 130$ nG at 95% CL. For reference, the Big Bang Nucleosynthesis constrains the magnetic fraction to be $\Omega_{B\gamma} \lesssim 0.1$ [40]. Constraints on the PMF strength for the two special cases of theoretical interest, are summarized in Table 7.6.

	$B_{1\,\mathrm{Mpc}}$/nG	B_{eff}/nG	$\Omega_{B\gamma}$
$n_B = -2.9$ Helical	< 1.1	< 1.1	$< 1.2 \times 10^{-7}$
$n_B = -2.9$ Non-helical	< 1.2	< 1.2	$< 1.4 \times 10^{-7}$
$n_B = 2$ Helical	< 0.0085	< 130	$< 10^{-3}$
$n_B = 2$ Non-helical	< 0.002	< 84	$< 6 \times 10^{-4}$

Table 7.6: Upper bounds (95% CL) on the PMF amplitude $B_{1\,\mathrm{Mpc}}$, the effective PMF strength B_{eff} and the magnetic density fraction $\Omega_{B\gamma}$ obtained from PLANCK and SPT. We present the results for both helical and non-helical cases.

Data sets	$B_{1\,\mathrm{Mpc}}$/nG
LowTEB + TTTEEE, ...	< 1.7
LowTEB + TTTEEE + BKP, ...	< 1.6
LowTEB + TTTEEE + SPT, ...	< 1.1
LowTEB + TTTEEE + BKP + SPT,	< 1.1

Table 7.7: Upper bounds (95% CL) for the maximal helical PMF amplitude $B_{1\,\mathrm{Mpc}}$ obtained from the combination of PLANCK data sets described in Sect. 7.1 and SPT. The magnetic spectral index $n_B = -2.9$, $r = 0$, and the PMF generation epoch parameter β is unconstrained.

7.3 Constraints from 500 Square Degrees of SPTpol Data

The 2019 SPT likelihood fits the observed CMB B-modes using the following expression:

$$D_\ell = r D_\ell^{\mathrm{tens}} + A_{\mathrm{lens}} D_\ell^{\mathrm{lens}} + C + P_L^{\nu_1\times\nu_2} D_\ell^{\mathrm{Poiss}} + A_{\mathrm{dust}} S_{150}^{\nu_1\times\nu_2} D_\ell^{\mathrm{dust,150}}, \tag{7.2}$$

where $D_\ell = \ell(\ell+1)C_\ell$, D_ℓ^{lens} is the theoretical prediction for the lensing power spectrum (as calculated by CAMB), D_ℓ^{tens} is the inflationary B-mode power spectrum, D_ℓ^{Poiss} is the Poisson noise power spectrum and $D_\ell^{\mathrm{dust,150}}$ is the galactic dust foreground power spectrum at the frequency of 150GHz. A_{lens} is a fitting constant that multiplies the lensing power spectrum, and r is the tensor to scalar ratio. C is a constant term added to the total power spectrum, $P_L^{\nu_1\times\nu_2}$ is a frequency dependent constant that multiplies the Poissonian noise D_ℓ^{Poiss}. Finally, $S_{150}^{\nu_1\times\nu_2}$ is a frequency depende nt constant fixed at 1 for the band 150x150 GHZ, that converts the foreground noise from 150 GHz to the other frequency bands, and A_{dust} is a multiplicative constant that multiplies the dust foregrounds. The D_ℓs are then binned in the data bins with $D_{\ell_{\mathrm{bin}}} = W_{\ell_{\mathrm{bin}}\ell}^{\nu_1\times\nu_2} D_\ell / A_{\mathrm{cal}}^{\nu_1\times\nu_2}$, with $W_{\ell_{\mathrm{bin}}\ell}^{\nu_1\times\nu_2}$ being the window function matrix, and then combined with the data points $D_{\ell_{\mathrm{bin}}}^{\mathrm{data}}$,

$$\Delta D_{\ell_{\mathrm{bin}}} = f_{\mathrm{beam}} D_{\ell_{\mathrm{bin}}} - D_{\ell_{\mathrm{bin}}}^{\mathrm{data}} \tag{7.3}$$

where f_{beam} are the beam factors. Finally the SPT log-likelihood is given by:

$$-\log L_{\mathrm{spt}} = \frac{1}{2}[\Delta D_{\ell'} C_{\ell'\ell}^{-1} \Delta D_\ell + \log|C|]. \tag{7.4}$$

We use the priors given in Tabel 7.8 and use the updtaed Python SPT likelihood code[79] to constrain the PMF with their CMB B-mode bandpowers.

Parameter	Prior	
$A_{\rm BB}$	$[0, 100]$	
$A_{\rm dust}$	$[0, 0.3]$	Gaussian
$A_{\rm cal}^{\nu_1}$	$[0.8, 1.25]$	Gaussian
$A_{\rm cal}^{\nu_2}$	$[0.8, 1.25]$	Gaussian
$P_L^{150\times150}$.	$[0, 2]$	
$P_L^{90\times150}$.	$[0, 5]$	
$P_L^{90\times90}$ ..	$[0, 10]$	

Table 7.8: Priors on the nuisance parameters used in the 2019 SPT likelihood.

Adding the magnetic field power spectrum into the 2019 SPT likelihood, we obtain

$$D_\ell = rD_\ell^{\rm tens}+A_{\rm lens}D_\ell^{\rm lens}+C+P_L^{\nu_1\times\nu_2}D_\ell^{\rm Poiss}+A_{\rm dust}S_{150}^{\nu_1\times\nu_2}D_\ell^{\rm dust,150}+A_{\rm PMF}(D_\ell^{\rm PMF,V}+A_\beta D_\ell^{\rm PMF,T}) \tag{7.5}$$

where $A_{\rm PMF} = (\frac{B_{\rm 1Mpc}}{3{\rm nG}})^4$, $A_\beta = (\frac{\beta}{17})^{1.9}$ [80].

We find that $B_{1\,\rm Mpc} < 0.06$ nG at 68% CL for non-helical PMF with a spectral index $n_B = 2$, and $B_{1\,\rm Mpc} < 0.08$ nG for a helical PMF with $n_B = 2$. The corresponding marginalized probability distribution functions are shown in Figs. 7.5 and 7.6. The increase in the upper bound from 0.06 to 0.08 nG is consistent with the factor of ~ 3 difference in the PMF sourced vector mode contribution to BB. Since the CMB spectra scale as $B_{\rm 1Mpc}^4$, it translates into a factor of $3^{1/4} \approx 1.3 \approx 0.08/0.06$ difference in the bound.

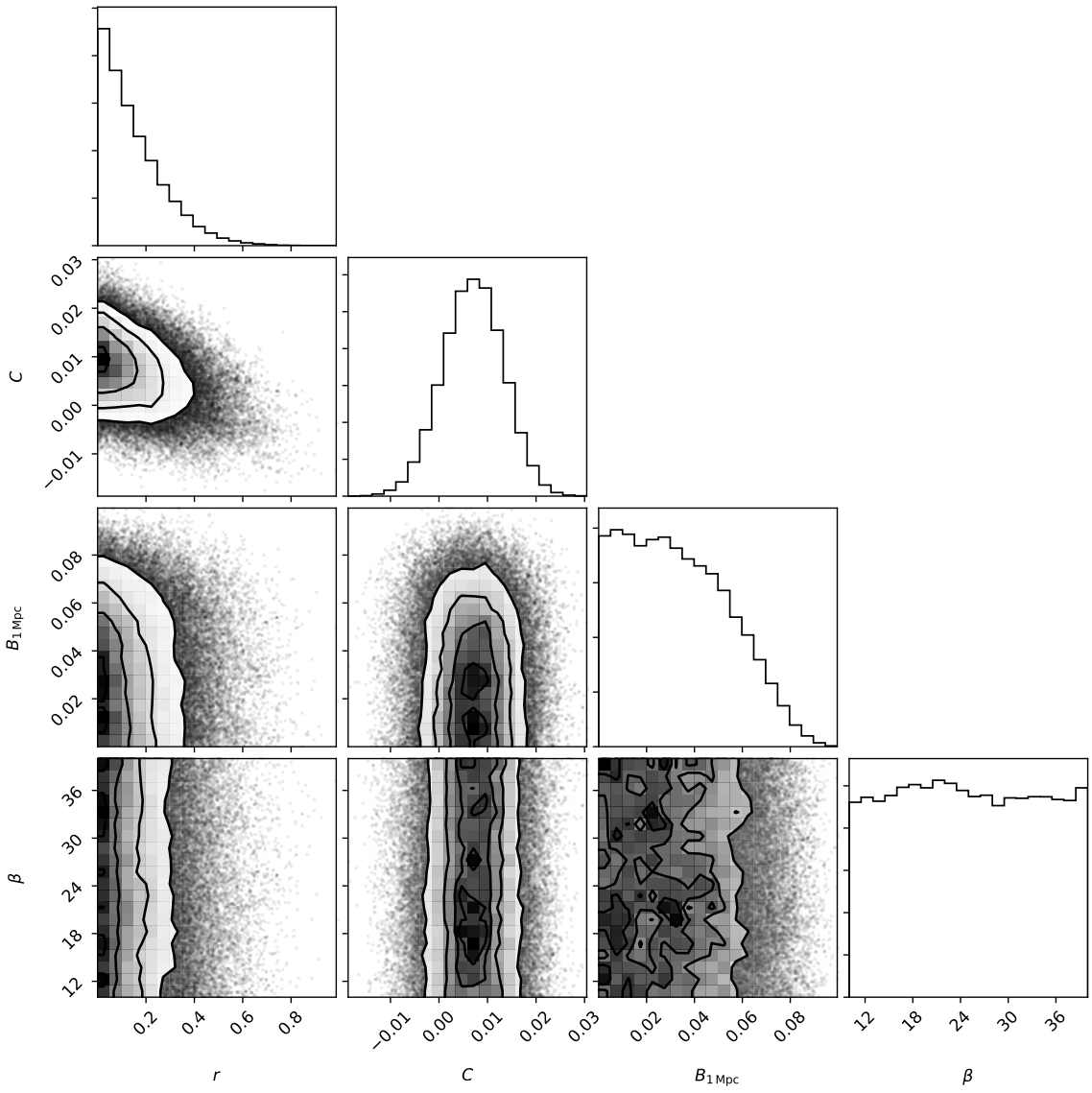

Figure 7.5: Parameter constraints from 2019 SPT data at 68% CL. We consider a non-helical PMF with $n_B = 2$.

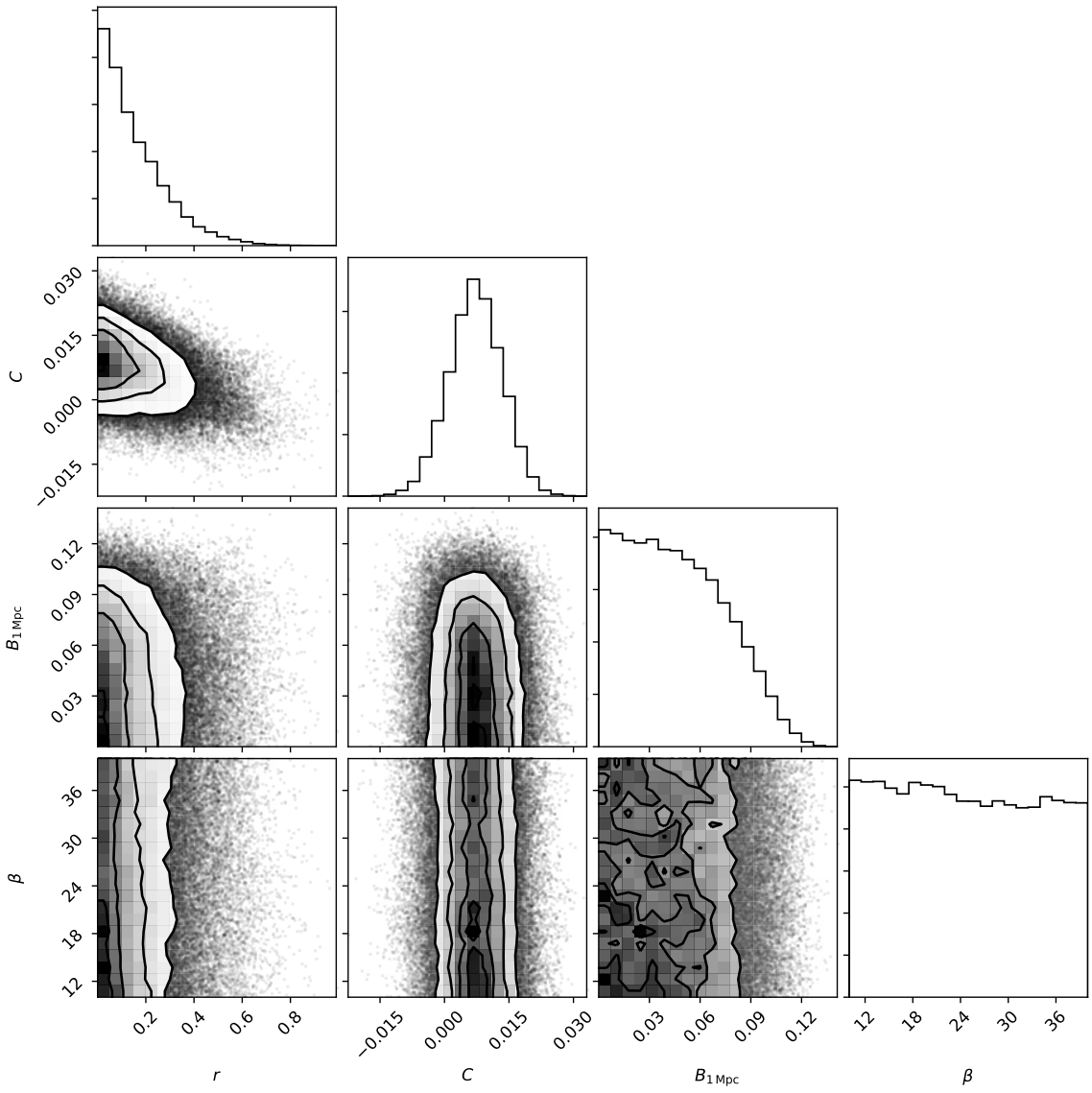

Figure 7.6: Parameter constraints from 2019 SPT data at 68% CL. We consider a maximum helical PMF with $n_B = 2$.

Chapter 8

Summary and outlook

We have derived the bounds on the strength of the primordial magnetic field (both non-helical and helical) from the SPT CMB B-mode polarization measurements in combination with the CMB temperature and polarization data from Planck, as well as the 2015 Planck data alone, 2019 SPT data alone.

For a nearly scale-invariant helical PMF with $n_B = -2.9$, the bound is 1.7 nG at 95% CL from the 2015 Planck data alone. This is the only case when a helical PMF is better constrained than the non-helical one. Usually, adding maximal helicity relaxes the bound on $B_{1\,\mathrm{Mpc}}$, effectively allowing more magnetic energy to be present without violating the CMB.

Adding the SPT information significantly tightens the bound, as it constrains the PMF vector mode contribution to B-modes at $\ell \sim 1000$. Specifically, adding the SPT data reduces the 95% CL bound on $B_{1\,\mathrm{Mpc}}$, after marginalizing over the magnetic spectral index n_B, from 3.3 nG to 1.5 nG. For a nearly scale-invariant PMF with $n_B = -2.9$, the bound is reduced from 2 nG to 1.2 nG for a non-helical PMF. The effective strength of a PMF generated in post-inflationary phase transitions, with $n_B = 2$, is constrained to $B_{\mathrm{eff}} < 100$ nG, corresponding to $\Omega_{B\gamma} < 10^{-3}$, or $B_{1\,\mathrm{Mpc}} < 0.002$ nG, at 95% CL for non-helical PMFS. By adding helicity we obtain a slightly stronger constraint on a nearly scale-invariant PMF, namely, 1.1 nG when combining Planck with the B-mode polarization spectrum from SPT. This is the only case where adding the helicity does not weaken the CMB constraints on PMF.

Our results, as well as those obtained by the POLARBEAR collaboration in [35], demonstrate that one can extract competitive information about PMFs even from relatively poor B-mode measurements. Future CMB experiments, in addition to significantly improving the measurement of the B-mode spectrum at lower ℓ, will eventually provide reliable data on scales relevant for the inflationary tensor mode. Such data will help to constrain the passive tensor PMF mode and, thus, the time of the generation of the PMF. Future CMB experiments will also constrain the parity-odd TB and EB correlations, leading to meaningful bounds on the helical component of the PMF, which has been neglected in the present

work. They will also tightly constrain the mode-coupling correlations induced by the Faraday rotation of CMB polarizations. The Faraday rotation angle is linear in $B_{1\,\mathrm{Mpc}}$, while CMB anisotropies scale as a square of the PMF strength (so that the CMB spectra scale as $B^4_{1\,\mathrm{Mpc}}$), and, with the improved sensitivity and resolution of upcoming experiments, can reduce the upper bound on $B_{1\,\mathrm{Mpc}}$ by an order of magnitude.

Bibliography

[1] J. T. Sayre, C. L. Reichardt, J. W. Henning, P. A. R. Ade, A. J. Anderson, J. E. Austermann, J. S. Avva, J. A. Beall, A. N. Bender, B. A. Benson, F. Bianchini, L. E. Bleem, J. E. Carlstrom, C. L. Chang, H. C. Chiang, R. Citron, C. Corbett Moran, T. M. Crawford, A. T. Crites, T. de Haan, M. A. Dobbs, W. Everett, J. Gallicchio, E. M. George, A. Gilbert, N. Gupta, N. W. Halverson, N. Harrington, G. C. Hilton, G. P. Holder, W. L. Holzapfel, J. D. Hrubes, N. Huang, J. Hubmayr, K. D. Irwin, L. Knox, A. T. Lee, D. Li, A. Lowitz, J. J. McMahon, S. S. Meyer, L. M. Mocanu, J. Montgomery, A. Nadolski, T. Natoli, J. P. Nibarger, G. Noble, V. Novosad, S. Padin, S. Patil, C. Pryke, J. E. Ruhl, B. R. Saliwanchik, K. K. Schaffer, C. Sievers, G. Smecher, A. A. Stark, C. Tucker, K. Vanderlinde, T. Veach, J. D. Vieira, G. Wang, N. Whitehorn, W. L. K. Wu, and V. Yefremenko. Measurements of B-mode Polarization of the Cosmic Microwave Background from 500 Square Degrees of SPTpol Data. *arXiv e-prints*, page arXiv:1910.05748, Oct 2019.

[2] J. C. Mather, E. S. Cheng, D. A. Cottingham, R. E. Eplee, Jr., D. J. Fixsen, T. Hewagama, R. B. Isaacman, K. A. Jensen, S. S. Meyer, P. D. Noerdlinger, S. M. Read, L. P. Rosen, R. A. Shafer, E. L. Wright, C. L. Bennett, N. W. Boggess, M. G. Hauser, T. Kelsall, S. H. Moseley, Jr., R. F. Silverberg, G. F. Smoot, R. Weiss, and D. T. Wilkinson. Measurement of the cosmic microwave background spectrum by the COBE FIRAS instrument. ApJ, 420:439–444, January 1994.

[3] D. J. Fixsen and J. C. Mather. The Spectral Results of the Far-Infrared Absolute Spectrophotometer Instrument on COBE. ApJ, 581:817–822, December 2002.

[4] G. F. Smoot, C. L. Bennett, A. Kogut, E. L. Wright, J. Aymon, N. W. Boggess, E. S. Cheng, G. de Amici, S. Gulkis, M. G. Hauser, G. Hinshaw, P. D. Jackson, M. Janssen, E. Kaita, T. Kelsall, P. Keegstra, C. Lineweaver, K. Loewenstein, P. Lubin, J. Mather, S. S. Meyer, S. H. Moseley, T. Murdock, L. Rokke, R. F. Silverberg, L. Tenorio, R. Weiss, and D. T. Wilkinson. Structure in the COBE differential microwave radiometer first-year maps. ApJ, 396:L1–L5, September 1992.

[5] M. R. Nolta, J. Dunkley, R. S. Hill, G. Hinshaw, E. Komatsu, D. Larson, L. Page, D. N. Spergel, C. L. Bennett, B. Gold, N. Jarosik, N. Odegard, J. L. Weiland, E. Wollack, M. Halpern, A. Kogut, M. Limon, S. S. Meyer, G. S. Tucker, and E.L. Wright. Five-Year Wilkinson Microwave Anisotropy Probe (WMAP) Observations: Angular Power Spectra. ApJS, 180:296–305, February 2009.

[6] Andrii Neronov and Ievgen Vovk. Evidence for Strong Extragalactic Magnetic Fields from Fermi Observations of TeV Blazars. *Science*, 328(5974):73, Apr 2010.

[7] P. P. Kronberg. Extragalactic magnetic fields. *Reports on Progress in Physics*, 57(4):325–382, Apr 1994.

[8] Rainer Beck and Richard Wielebinski. *Magnetic Fields in Galaxies*, volume 5, page 641. 2013.

[9] C. L. Carilli and G. B. Taylor. Cluster Magnetic Fields. ARA&A, 40:319–348, Jan 2002.

[10] Martin L. Bernet, Francesco Miniati, Simon J. Lilly, Philipp P. Kronberg, and Miroslava Dessauges-Zavadsky. Strong magnetic fields in normal galaxies at high redshift. Nature, 454(7202):302–304, Jul 2008.

[11] Russell M. Kulsrud and Ellen G. Zweibel. On the origin of cosmic magnetic fields. *Reports on Progress in Physics*, 71(4):046901, Apr 2008.

[12] Ruth Durrer and Andrii Neronov. Cosmological magnetic fields: their generation, evolution and observation. A&A Rev., 21:62, Jun 2013.

[13] Alejandra Kandus, Kerstin E. Kunze, and Christos G. Tsagas. Primordial magnetogenesis. Phys. Rep., 505(1):1–58, Aug 2011.

[14] Ie. Vovk, A. M. Taylor, D. Semikoz, and A. Neronov. Fermi/LAT Observations of 1ES 0229+200: Implications for Extragalactic Magnetic Fields and Background Light. ApJ, 747(1):L14, Mar 2012.

[15] Shin'ichiro Ando and Alexander Kusenko. Evidence for Gamma-ray Halos Around Active Galactic Nuclei and the First Measurement of Intergalactic Magnetic Fields. ApJ, 722(1):L39–L44, Oct 2010.

[16] F. Tavecchio, G. Ghisellini, L. Foschini, G. Bonnoli, G. Ghirlanda, and P. Coppi. The intergalactic magnetic field constrained by Fermi/Large Area Telescope observations of the TeV blazar 1ES0229+200. MNRAS, 406(1):L70–L74, Jul 2010.

[17] A. M. Taylor, I. Vovk, and A. Neronov. Extragalactic magnetic fields constraints from simultaneous GeV-TeV observations of blazars. A&A, 529:A144, May 2011.

[18] Christos G. Tsagas. Electromagnetic fields in curved spacetimes. *Classical and Quantum Gravity*, 22(2):393–407, Jan 2005.

[19] Kandaswamy Subramanian and John D. Barrow. Microwave Background Signals from Tangled Magnetic Fields. Phys. Rev. Lett., 81(17):3575–3578, Oct 1998.

[20] Michael S. Turner and Lawrence M. Widrow. Inflation-produced, large-scale magnetic fields. *Phys. Rev. D*, 37:2743–2754, May 1988.

[21] Lawrence M. Widrow, Dongsu Ryu, Dominik R. G. Schleicher, Kandaswamy Subramanian, Christos G. Tsagas, and Rudolf A. Treumann. The First Magnetic Fields. Space Sci. Rev., 166(1-4):37–70, May 2012.

[22] Camille Bonvin, Chiara Caprini, and Ruth Durrer. Magnetic fields from inflation: The CMB temperature anisotropies. Phys. Rev. D, 88(8):083515, Oct 2013.

[23] Jarkko Ahonen and Kari Enqvist. Magnetic field generation in first order phase transition bubble collisions. Phys. Rev. D, 57(2):664–673, Jan 1998.

[24] Michael McNeil Forbes and Ariel Zhitnitsky. Primordial galactic magnetic fields from domain walls at the qcd phase transition. *Phys. Rev. Lett.*, 85:5268–5271, Dec 2000.

[25] Leonard S. Kisslinger. Magnetic wall from chiral phase transition and cmbr correlations. *Phys. Rev. D*, 68:043516, Aug 2003.

[26] Tina Kahniashvili, Alexander G. Tevzadze, and Bharat Ratra. Phase Transition Generated Cosmological Magnetic Field at Large Scales. ApJ, 726(2):78, Jan 2011.

[27] Alexander G. Tevzadze, Leonard Kisslinger, Axel Brand enburg, and Tina Kahniashvili. Magnetic Fields from QCD Phase Transitions. ApJ, 759(1):54, Nov 2012.

[28] Eduard F. Piratova, Edilson A. Reyes, and Héctor J. Hortúa. Helical magnetic fields via baryon asymmetry. *arXiv e-prints*, page arXiv:1409.1567, Sep 2014.

[29] Chiara Caprini and Lorenzo Sorbo. Adding helicity to inflationary magnetogenesis. J. Cosmology Astropart. Phys., 2014(10):056, Oct 2014.

[30] Douglas Scott. The standard model of cosmology: A skeptic's guide, 2018.

[31] Planck Collaboration, R. Adam, P. A. R. Ade, N. Aghanim, Y. Akrami, M. I. R. Alves, F. Argüeso, M. Arnaud, F. Arroja, M. Ashdown, J. Aumont, C. Baccigalupi, M. Ballardini, A. J. Band ay, R. B. Barreiro, J. G. Bartlett, N. Bartolo, S. Basak, P. Battaglia, E. Battaner, R. Battye, K. Benabed, A. Benoît, A. Benoit-Lévy, J. P. Bernard, M. Bersanelli, B. Bertincourt, P. Bielewicz, I. Bikmaev, J. J. Bock, H. Böhringer, A. Bonaldi, L. Bonavera, J. R. Bond, J. Borrill, F. R. Bouchet, F. Boulanger, M. Bucher, R. Burenin, C. Burigana, R. C. Butler, E. Calabrese, J. F. Cardoso, P. Carvalho, B. Casaponsa, G. Castex, A. Catalano, A. Challinor, A. Chamballu, R. R. Chary, H. C. Chiang, J. Chluba, G. Chon, P. R. Christensen, S. Church, M. Clemens, D. L. Clements, S. Colombi, L. P. L. Colombo, C. Combet, B. Comis, D. Contreras, F. Couchot, A. Coulais, B. P. Crill, M. Cruz, A. Curto, F. Cuttaia, L. Danese, R. D. Davies, R. J. Davis, P. de Bernardis, A. de Rosa, G. de Zotti, J. Delabrouille, J. M. Delouis, F. X. Désert, E. Di Valentino, C. Dickinson, J. M. Diego, K. Dolag, H. Dole, S. Donzelli, O. Doré, M. Douspis, A. Ducout, J. Dunkley, X. Dupac, G. Efstathiou, P. R. M. Eisenhardt, F. Elsner, T. A. Enßlin, H. K. Eriksen, E. Falgarone, Y. Fantaye, M. Farhang, S. Feeney, J. Fergusson, R. Fernandez-Cobos, F. Feroz, F. Finelli, E. Florido, O. Forni, M. Frailis, A. A. Fraisse, C. Franceschet, E. Franceschi, A. Frejsel, A. Frolov, S. Galeotta, S. Galli, K. Ganga, C. Gauthier, R. T. Génova-Santos, M. Gerbino, T. Ghosh, M. Giard, Y. Giraud-Héraud, E. Giusarma, E. Gjerløw, J. González-Nuevo, K. M. Górski, K. J. B. Grainge, S. Gratton, A. Gregorio, A. Gruppuso, J. E. Gudmundsson, J. Hamann, W. Handley, F. K. Hansen, D. Hanson, D. L. Harrison, A. Heavens, G. Helou, S. Henrot-Versillé, C. Hernández-Monteagudo, D. Herranz, S. R. Hildebrandt, E. Hivon, M. Hobson, W. A. Holmes, A. Hornstrup, W. Hovest, Z. Huang, K. M. Huffenberger, G. Hurier, S. Ilić, A. H. Jaffe, T. R. Jaffe, T. Jin, W. C. Jones, M. Juvela, A. Karakci, E. Keihänen, R. Keskitalo, I. Khamitov, K. Kiiveri, J. Kim, T. S. Kisner, R. Kneissl, J. Knoche, L. Knox, N. Krachmalnicoff, M. Kunz, H. Kurki-Suonio, F. Lacasa, G. Lagache, A. Lähteenmäki, J. M. Lamarre, M. Langer, A. Lasenby,

M. Lattanzi, C. R. Lawrence, M. Le Jeune, J. P. Leahy, E. Lellouch, R. Leonardi, J. León-Tavares, J. Lesgourgues, F. Levrier, A. Lewis, M. Liguori, P. B. Lilje, M. Lilley, M. Linden-Vørnle, V. Lindholm, H. Liu, M. López-Caniego, P. M. Lubin, Y. Z. Ma, J. F. Macías-Pérez, G. Maggio, D. Maino, D. S. Y. Mak, N. Mandolesi, A. Mangilli, A. Marchini, A. Marcos-Caballero, D. Marinucci, M. Maris, D. J. Marshall, P. G. Martin, M. Martinelli, E. Martínez-González, S. Masi, S. Matarrese, P. Mazzotta, J. D. McEwen, P. McGehee, S. Mei, P. R. Meinhold, A. Melchiorri, J. B. Melin, L. Mendes, A. Mennella, M. Migliaccio, K. Mikkelsen, M. Millea, S. Mitra, M. A. Miville-Deschênes, D. Molinari, A. Moneti, L. Montier, R. Moreno, G. Morgante, D. Mortlock, A. Moss, S. Mottet, M. Münchmeyer, D. Munshi, J. A. Murphy, A. Narimani, P. Naselsky, A. Nastasi, F. Nati, P. Natoli, M. Negrello, C. B. Netterfield, H. U. Nørgaard-Nielsen, F. Noviello, D. Novikov, I. Novikov, M. Olamaie, N. Oppermann, E. Orlando, C. A. Oxborrow, F. Paci, L. Pagano, F. Pajot, R. Paladini, S. Pandolfi, D. Paoletti, B. Partridge, F. Pasian, G. Patanchon, T. J. Pearson, M. Peel, H. V. Peiris, V. M. Pelkonen, O. Perdereau, L. Perotto, Y. C. Perrott, F. Perrotta, V. Pettorino, F. Piacentini, M. Piat, E. Pierpaoli, D. Pietrobon, S. Plaszczynski, D. Pogosyan, E. Pointecouteau, G. Polenta, L. Popa, G. W. Pratt, G. Prézeau, S. Prunet, J. L. Puget, J. P. Rachen, B. Racine, W. T. Reach, R. Rebolo, M. Reinecke, M. Remazeilles, C. Renault, A. Renzi, I. Ristorcelli, G. Rocha, M. Roman, E. Romelli, C. Rosset, M. Rossetti, A. Rotti, G. Roudier, B. Rouillé d'Orfeuil, M. Rowan-Robinson, J. A. Rubiño-Martín, B. Ruiz-Granados, C. Rumsey, B. Rusholme, N. Said, V. Salvatelli, L. Salvati, M. Sandri, H. S. Sanghera, D. Santos, R. D. E. Saunders, A. Sauvé, M. Savelainen, G. Savini, B. M. Schaefer, M. P. Schammel, D. Scott, M. D. Seiffert, P. Serra, E. P. S. Shellard, T. W. Shimwell, M. Shiraishi, K. Smith, T. Souradeep, L. D. Spencer, M. Spinelli, S. A. Stanford, D. Stern, V. Stolyarov, R. Stompor, A. W. Strong, R. Sudiwala, R. Sunyaev, P. Sutter, D. Sutton, A. S. Suur-Uski, J. F. Sygnet, J. A. Tauber, D. Tavagnacco, L. Terenzi, D. Texier, L. Toffolatti, M. Tomasi, M. Tornikoski, D. Tramonte, M. Tristram, A. Troja, T. Trombetti, M. Tucci, J. Tuovinen, M. Türler, G. Umana, L. Valenziano, J. Valiviita, F. Van Tent, T. Vassallo, L. Vibert, M. Vidal, M. Viel, P. Vielva, F. Villa, L. A. Wade, B. Walter, B. D. Wand elt, R. Watson, I. K. Wehus, N. Welikala, J. Weller, M. White, S. D. M. White, A. Wilkinson, D. Yvon, A. Zacchei, J. P. Zibin, and A. Zonca. Planck 2015 results. I. Overview of products and scientific results. A&A, 594:A1, Sep 2016.

[32] D. Larson, J. Dunkley, G. Hinshaw, E. Komatsu, M. R. Nolta, C. L. Bennett, B. Gold, M. Halpern, R. S. Hill, N. Jarosik, A. Kogut, M. Limon, S. S. Meyer, N. Odegard, L. Page, K. M. Smith, D. N. Spergel, G. S. Tucker, J. L. Weiland, E. Wollack, and E. L. Wright. Seven-year Wilkinson Microwave Anisotropy Probe (WMAP) Observations: Power Spectra and WMAP-derived Parameters. ApJS, 192(2):16, Feb 2011.

[33] R. Keisler, C. L. Reichardt, K. A. Aird, B. A. Benson, L. E. Bleem, J. E. Carlstrom, C. L. Chang, H. M. Cho, T. M. Crawford, A. T. Crites, T. de Haan, M. A. Dobbs, J. Dudley, E. M. George, N. W. Halverson, G. P. Holder, W. L. Holzapfel, S. Hoover, Z. Hou, J. D. Hrubes, M. Joy, L. Knox, A. T. Lee, E. M. Leitch, M. Lueker, D. Luong-Van, J. J. McMahon, J. Mehl, S. S. Meyer, M. Millea, J. J. Mohr, T. E. Montroy, T. Natoli, S. Padin, T. Plagge, C. Pryke, J. E. Ruhl, K. K. Schaffer, L. Shaw, E. Shirokoff, H. G. Spieler, Z. Staniszewski, A. A. Stark, K. Story, A. van Engelen, K. Vanderlinde, J. D. Vieira, R. Williamson, and O. Zahn. A Measurement of the Damping Tail of the

Cosmic Microwave Background Power Spectrum with the South Pole Telescope. ApJ, 743(1):28, Dec 2011.

[34] Daniela Paoletti and Fabio Finelli. Constraints on a stochastic background of primordial magnetic fields with WMAP and South Pole Telescope data. *Physics Letters B*, 726(1-3):45–49, Oct 2013.

[35] Peter A. R. Ade, Kam Arnold, Matt Atlas, Carlo Baccigalupi, Darcy Barron, David Boettger, Julian Borrill, Scott Chapman, Yuji Chinone, Ari Cukierman, Matt Dobbs, Anne Ducout, Roland o Dunner, Tucker Elleflot, Josquin Errard, Giulio Fabbian, Stephen Feeney, Chang Feng, Adam Gilbert, Neil Goeckner-Wald, John Groh, Grantland Hall, Nils W. Halverson, Masaya Hasegawa, Kaori Hattori, Masashi Hazumi, Charles Hill, William L. Holzapfel, Yasuto Hori, Logan Howe, Yuki Inoue, Gregory C. Jaehnig, Andrew H. Jaffe, Oliver Jeong, Nobuhiko Katayama, Jonathan P. Kaufman, Brian Keating, Zigmund Kermish, Reijo Keskitalo, Theodore Kisner, Akito Kusaka, Maude Le Jeune, Adrian T. Lee, Erik M. Leitch, David Leon, Yun Li, Eric Linder, Lindsay Lowry, Frederick Matsuda, Tomotake Matsumura, Nathan Miller, Josh Montgomery, Michael J. Myers, Martin Navaroli, Haruki Nishino, Takahiro Okamura, Hans Paar, Julien Peloton, Levon Pogosian, Davide Poletti, Giuseppe Puglisi, Christopher Raum, Gabriel Rebeiz, Christian L. Reichardt, Paul L. Richards, Colin Ross, Kaja M. Rotermund, David E. Schenck, Blake D. Sherwin, Meir Shimon, Ian Shirley, Praween Siritanasak, Graeme Smecher, Nathan Stebor, Bryan Steinbach, Aritoki Suzuki, Junichi Suzuki, Osamu Tajima, Satoru Takakura, Alexei Tikhomirov, Takayuki Tomaru, Nathan Whitehorn, Brandon Wilson, Amit Yadav, Alex Zahn, Oliver Zahn, and Polarbear Collaboration. POLARBEAR constraints on cosmic birefringence and primordial magnetic fields. Phys. Rev. D, 92(12):123509, Dec 2015.

[36] Alex Zucca, Yun Li, and Levon Pogosian. Constraints on Primordial Magnetic Fields from Planck combined with the South Pole Telescope CMB B-mode polarization measurements. *Phys. Rev.*, D95(6):063506, 2017.

[37] Bharat Ratra. Cosmological "Seed" Magnetic Field from Inflation. ApJ, 391:L1, May 1992.

[38] Kerstin E. Kunze. CMB and matter power spectra from cross correlations of primordial curvature and magnetic fields. Phys. Rev. D, 87(10):103005, May 2013.

[39] G. S. Bali, F. Bruckmann, G. Endrődi, Z. Fodor, S. D. Katz, S. Krieg, A. Schäfer, and K. K. Szabó. The QCD phase diagram for external magnetic fields. *Journal of High Energy Physics*, 2012:44, Feb 2012.

[40] Dario Grasso and Hector R. Rubinstein. Revisiting nucleosynthesis constraints on primordial magnetic fields. *Physics Letters B*, 379:73–79, Feb 1996.

[41] Eric G. Blackman. Magnetic Helicity and Large Scale Magnetic Fields: A Primer. Space Sci. Rev., 188(1-4):59–91, May 2015.

[42] Alexei A. Pevtsov, Mitchell A. Berger, Alexander Nindos, Aimee A. Norton, and Lidia van Driel-Gesztelyi. *Magnetic Helicity, Tilt, and Twist*, volume 53, page 285. 2015.

[43] W. Hu and M. White. CMB anisotropies: Total angular momentum method. Phys. Rev. D, 56:596–615, July 1997.

[44] M. Zaldarriaga and U. Seljak. All-sky analysis of polarization in the microwave background. Phys. Rev. D, 55:1830–1840, February 1997.

[45] Matias Zaldarriaga and Uros Seljak. CMBFAST for Spatially Closed Universes. ApJS, 129(2):431–434, Aug 2000.

[46] K. Subramanian. Primordial magnetic fields and CMB anisotropies. *Astronomische Nachrichten*, 327:403, Jun 2006.

[47] Ruth Durrer. Cosmic magnetic fields and the CMB. New A Rev., 51(3-4):275–280, Mar 2007.

[48] Kip S. Thorne. Primordial Element Formation, Primordial Magnetic Fields, and the Isotropy of the Universe. ApJ, 148:51, Apr 1967.

[49] John D. Barrow, Pedro G. Ferreira, and Joseph Silk. Constraints on a Primordial Magnetic Field. Phys. Rev. Lett., 78(19):3610–3613, May 1997.

[50] Alejandra Kandus, Kerstin E. Kunze, and Christos G. Tsagas. Primordial magnetogenesis. *Phys. Rept.*, 505:1–58, 2011.

[51] D. Grasso and H. R. Rubinstein. Magnetic fields in the early Universe. Phys. Rep., 348(3):163–266, Jul 2001.

[52] Karsten Jedamzik, Višnja Katalinić, and Angela V. Olinto. Damping of cosmic magnetic fields. Phys. Rev. D, 57(6):3264–3284, Mar 1998.

[53] Tina Kahniashvili and Bharat Ratra. Effects of cosmological magnetic helicity on the cosmic microwave background. Phys. Rev. D, 71(10):103006, May 2005.

[54] Levon Pogosian, Tanmay Vachaspati, and Serge Winitzki. Signatures of kinetic and magnetic helicity in the cosmic microwave background radiation. Phys. Rev. D, 65(8):083502, Apr 2002.

[55] Chiara Caprini, Ruth Durrer, and Tina Kahniashvili. Cosmic microwave background and helical magnetic fields: The tensor mode. Phys. Rev. D, 69(6):063006, Mar 2004.

[56] Leonid Malyshkin and Stanislav Boldyrev. Magnetic Dynamo Action in Helical Turbulence. ApJ, 671(2):L185–L188, Dec 2007.

[57] Kandaswamy Subramanian and John D. Barrow. Magnetohydrodynamics in the early universe and the damping of nonlinear Alfvén waves. Phys. Rev. D, 58(8):083502, Oct 1998.

[58] Andrew Mack, Tina Kahniashvili, and Arthur Kosowsky. Microwave background signatures of a primordial stochastic magnetic field. Phys. Rev. D, 65(12):123004, Jun 2002.

[59] Planck Collaboration, P. A. R. Ade, N. Aghanim, M. Arnaud, F. Arroja, M. Ashdown, J. Aumont, C. Baccigalupi, M. Ballardini, A. J. Banday, R. B. Barreiro, N. Bartolo, E. Battaner, K. Benabed, A. Benoît, A. Benoit-Lévy, J. P. Bernard, M. Bersanelli, P. Bielewicz, J. J. Bock, A. Bonaldi, L. Bonavera, J. R. Bond, J. Borrill, F. R. Bouchet, M. Bucher, C. Burigana, R. C. Butler, E. Calabrese, J. F. Cardoso, A. Catalano, A. Chamballu, H. C. Chiang, J. Chluba, P. R. Christensen, S. Church, D. L. Clements, S. Colombi, L. P. L. Colombo, C. Combet, F. Couchot, A. Coulais, B. P. Crill, A. Curto, F. Cuttaia, L. Danese, R. D. Davies, R. J. Davis, P. de Bernardis, A. de Rosa, G. de Zotti, J. Delabrouille, F. X. Désert, J. M. Diego, K. Dolag, H. Dole, S. Donzelli, O. Doré, M. Douspis, A. Ducout, X. Dupac, G. Efstathiou, F. Elsner, T. A. Enßlin, H. K. Eriksen, J. Fergusson, F. Finelli, E. Florido, O. Forni, M. Frailis, A. A. Fraisse, E. Franceschi, A. Frejsel, S. Galeotta, S. Galli, K. Ganga, M. Giard, Y. Giraud-Héraud, E. Gjerløw, J. González-Nuevo, K. M. Górski, S. Gratton, A. Gregorio, A. Gruppuso, J. E. Gudmundsson, F. K. Hansen, D. Hanson, D. L. Harrison, G. Helou, S. Henrot-Versillé, C. Hernández-Monteagudo, D. Herranz, S. R. Hildebrand t, E. Hivon, M. Hobson, W. A. Holmes, A. Hornstrup, W. Hovest, K. M. Huffenberger, G. Hurier, A. H. Jaffe, T. R. Jaffe, W. C. Jones, M. Juvela, E. Keihänen, R. Keskitalo, J. Kim, T. S. Kisner, J. Knoche, M. Kunz, H. Kurki-Suonio, G. Lagache, A. Lähteenmäki, J. M. Lamarre, A. Lasenby, M. Lattanzi, C. R. Lawrence, J. P. Leahy, R. Leonardi, J. Lesgourgues, F. Levrier, M. Liguori, P. B. Lilje, M. Linden-Vørnle, M. López-Caniego, P. M. Lubin, J. F. Macías-Pérez, G. Maggio, D. Maino, N. Mand olesi, A. Mangilli, M. Maris, P. G. Martin, E. Martínez-González, S. Masi, S. Matarrese, P. McGehee, P. R. Meinhold, A. Melchiorri, L. Mendes, A. Mennella, M. Migliaccio, S. Mitra, M. A. Miville-Deschênes, D. Molinari, A. Moneti, L. Montier, G. Morgante, D. Mortlock, A. Moss, D. Munshi, J. A. Murphy, P. Naselsky, F. Nati, P. Natoli, C. B. Netterfield, H. U. Nørgaard-Nielsen, F. Noviello, D. Novikov, I. Novikov, N. Oppermann, C. A. Oxborrow, F. Paci, L. Pagano, F. Pajot, D. Paoletti, F. Pasian, G. Patanchon, O. Perdereau, L. Perotto, F. Perrotta, V. Pettorino, F. Piacentini, M. Piat, E. Pierpaoli, D. Pietrobon, S. Plaszczynski, E. Pointecouteau, G. Polenta, L. Popa, G. W. Pratt, G. Prézeau, S. Prunet, J. L. Puget, J. P. Rachen, R. Rebolo, M. Reinecke, M. Remazeilles, C. Renault, A. Renzi, I. Ristorcelli, G. Rocha, C. Rosset, M. Rossetti, G. Roudier, J. A. Rubiño-Martín, B. Ruiz-Granados, B. Rusholme, M. Sandri, D. Santos, M. Savelainen, G. Savini, D. Scott, M. D. Seiffert, E. P. S. Shellard, M. Shiraishi, L. D. Spencer, V. Stolyarov, R. Stompor, R. Sudiwala, R. Sunyaev, D. Sutton, A. S. Suur-Uski, J. F. Sygnet, J. A. Tauber, L. Terenzi, L. Toffolatti, M. Tomasi, M. Tristram, M. Tucci, J. Tuovinen, G. Umana, L. Valenziano, J. Valiviita, B. Van Tent, P. Vielva, F. Villa, L. A. Wade, B. D. Wandelt, I. K. Wehus, D. Yvon, A. Zacchei, and A. Zonca. Planck 2015 results. XIX. Constraints on primordial magnetic fields. A&A, 594:A19, Sep 2016.

[60] Axel Brandenburg, Ruth Durrer, Tina Kahniashvili, Sayan Mand al, and Weichen Winston Yin. Statistical properties of scale-invariant helical magnetic fields and applications to cosmology. J. Cosmology Astropart. Phys., 2018(8):034, Aug 2018.

[61] Ruth Durrer and Chiara Caprini. Primordial magnetic fields and causality. J. Cosmology Astropart. Phys., 2003(11):010, Nov 2003.

[62] Wayne Hu and Martin White. CMB anisotropies: Total angular momentum method. Phys. Rev. D, 56(2):596–615, Jul 1997.

[63] J. Richard Shaw and Antony Lewis. Massive neutrinos and magnetic fields in the early universe. Phys. Rev. D, 81(4):043517, Feb 2010.

[64] Antony Lewis. CMB anisotropies from primordial inhomogeneous magnetic fields. Phys. Rev. D, 70(4):043011, Aug 2004.

[65] Fabio Finelli, Francesco Paci, and Daniela Paoletti. Impact of stochastic primordial magnetic fields on the scalar contribution to cosmic microwave background anisotropies. Phys. Rev. D, 78(2):023510, Jul 2008.

[66] Massimo Giovannini. Magnetized initial conditions for CMB anisotropies. Phys. Rev. D, 70(12):123507, Dec 2004.

[67] Massimo Giovannini. Tight coupling expansion and fully inhomogeneous magnetic fields. Phys. Rev. D, 74(6):063002, Sep 2006.

[68] K. E. Kunze. Effects of helical magnetic fields on the cosmic microwave background. Phys. Rev. D, 85(8):083004, April 2012.

[69] Mario Ballardini, Fabio Finelli, and Daniela Paoletti. CMB anisotropies generated by a stochastic background of primordial magnetic fields with non-zero helicity. *JCAP*, 1510(10):031, 2015.

[70] Antony Lewis, Anthony Challinor, and Anthony Lasenby. Efficient Computation of Cosmic Microwave Background Anisotropies in Closed Friedmann-Robertson-Walker Models. ApJ, 538(2):473–476, Aug 2000.

[71] Daniela Paoletti and Fabio Finelli. CMB constraints on a stochastic background of primordial magnetic fields. Phys. Rev. D, 83(12):123533, Jun 2011.

[72] Antony Lewis and Sarah Bridle. Cosmological parameters from CMB and other data: A Monte Carlo approach. Phys. Rev. D, 66(10):103511, Nov 2002.

[73] Planck Collaboration, N. Aghanim, M. Arnaud, M. Ashdown, J. Aumont, C. Baccigalupi, A. J. Band ay, R. B. Barreiro, J. G. Bartlett, N. Bartolo, E. Battaner, K. Benabed, A. Benoît, A. Benoit-Lévy, J. P. Bernard, M. Bersanelli, P. Bielewicz, J. J. Bock, A. Bonaldi, L. Bonavera, J. R. Bond, J. Borrill, F. R. Bouchet, F. Boulanger, M. Bucher, C. Burigana, R. C. Butler, E. Calabrese, J. F. Cardoso, A. Catalano, A. Challinor, H. C. Chiang, P. R. Christensen, D. L. Clements, L. P. L. Colombo, C. Combet, A. Coulais, B. P. Crill, A. Curto, F. Cuttaia, L. Danese, R. D. Davies, R. J. Davis, P. de Bernardis, A. de Rosa, G. de Zotti, J. Delabrouille, F. X. Désert, E. Di Valentino, C. Dickinson, J. M. Diego, K. Dolag, H. Dole, S. Donzelli, O. Doré, M. Douspis, A. Ducout, J. Dunkley, X. Dupac, G. Efstathiou, F. Elsner, T. A. Enßlin, H. K. Eriksen, J. Fergusson, F. Finelli, O. Forni, M. Frailis, A. A. Fraisse, E. Franceschi, A. Frejsel, S. Galeotta, S. Galli, K. Ganga, C. Gauthier, M. Gerbino, M. Giard, E. Gjerløw, J. González-Nuevo, K. M. Górski, S. Gratton, A. Gregorio, A. Gruppuso, J. E. Gudmundsson, J. Hamann, F. K. Hansen, D. L. Harrison, G. Helou, S. Henrot-Versillé, C. Hernández-Monteagudo, D. Herranz, S. R. Hildebrand t, E. Hivon, W. A. Holmes, A. Hornstrup, K. M. Huffenberger, G. Hurier, A. H. Jaffe, W. C. Jones, M. Juvela, E. Keihänen, R. Keskitalo, K. Kiiveri, J. Knoche, L. Knox, M. Kunz, H. Kurki-Suonio, G. Lagache, A. Lähteenmäki, J. M. Lamarre, A. Lasenby, M. Lattanzi, C. R. Lawrence, M. Le Jeune, R. Leonardi,

J. Lesgourgues, F. Levrier, A. Lewis, M. Liguori, P. B. Lilje, M. Lilley, M. Linden-Vørnle, V. Lindholm, M. López-Caniego, J. F. Macías-Pérez, B. Maffei, G. Maggio, D. Maino, N. Mandolesi, A. Mangilli, M. Maris, P. G. Martin, E. Martínez-González, S. Masi, S. Matarrese, P. R. Meinhold, A. Melchiorri, M. Migliaccio, M. Millea, S. Mitra, M. A. Miville-Deschênes, A. Moneti, L. Montier, G. Morgante, D. Mortlock, S. Mottet, D. Munshi, J. A. Murphy, A. Narimani, P. Naselsky, F. Nati, P. Natoli, F. Noviello, D. Novikov, I. Novikov, C. A. Oxborrow, F. Paci, L. Pagano, F. Pajot, D. Paoletti, B. Partridge, F. Pasian, G. Patanchon, T. J. Pearson, O. Perdereau, L. Perotto, V. Pettorino, F. Piacentini, M. Piat, E. Pierpaoli, D. Pietrobon, S. Plaszczynski, E. Pointecouteau, G. Polenta, N. Ponthieu, G. W. Pratt, S. Prunet, J. L. Puget, J. P. Rachen, M. Reinecke, M. Remazeilles, C. Renault, A. Renzi, I. Ristorcelli, G. Rocha, M. Rossetti, G. Roudier, B. Rouillé d'Orfeuil, J. A. Rubiño-Martín, B. Rusholme, L. Salvati, M. Sandri, D. Santos, M. Savelainen, G. Savini, D. Scott, P. Serra, L. D. Spencer, M. Spinelli, V. Stolyarov, R. Stompor, R. Sunyaev, D. Sutton, A. S. Suur-Uski, J. F. Sygnet, J. A. Tauber, L. Terenzi, L. Toffolatti, M. Tomasi, M. Tristram, T. Trombetti, M. Tucci, J. Tuovinen, G. Umana, L. Valenziano, J. Valiviita, F. Van Tent, P. Vielva, F. Villa, L. A. Wade, B. D. Wandelt, I. K. Wehus, D. Yvon, A. Zacchei, and A. Zonca. Planck 2015 results. XI. CMB power spectra, likelihoods, and robustness of parameters. A&A, 594:A11, Sep 2016.

[74] R. Keisler, S. Hoover, N. Harrington, J. W. Henning, P. A. R. Ade, K. A. Aird, J. E. Austermann, J. A. Beall, A. N. Bender, B. A. Benson, L. E. Bleem, J. E. Carlstrom, C. L. Chang, H. C. Chiang, H. M. Cho, R. Citron, T. M. Crawford, A. T. Crites, T. de Haan, M. A. Dobbs, W. Everett, J. Gallicchio, J. Gao, E. M. George, A. Gilbert, N. W. Halverson, D. Hanson, G. C. Hilton, G. P. Holder, W. L. Holzapfel, Z. Hou, J. D. Hrubes, N. Huang, J. Hubmayr, K. D. Irwin, L. Knox, A. T. Lee, E. M. Leitch, D. Li, D. Luong-Van, D. P. Marrone, J. J. McMahon, J. Mehl, S. S. Meyer, L. Mocanu, T. Natoli, J. P. Nibarger, V. Novosad, S. Padin, C. Pryke, C. L. Reichardt, J. E. Ruhl, B. R. Saliwanchik, J. T. Sayre, K. K. Schaffer, E. Shirokoff, G. Smecher, A. A. Stark, K. T. Story, C. Tucker, K. Vanderlinde, J. D. Vieira, G. Wang, N. Whitehorn, V. Yefremenko, and O. Zahn. Measurements of Sub-degree B-mode Polarization in the Cosmic Microwave Background from 100 Square Degrees of SPTpol Data. ApJ, 807(2):151, Jul 2015.

[75] BICEP2/Keck Collaboration, Planck Collaboration, P. A. R. Ade, N. Aghanim, Z. Ahmed, R. W. Aikin, K. D. Alexander, M. Arnaud, J. Aumont, C. Baccigalupi, A. J. Banday, D. Barkats, R. B. Barreiro, J. G. Bartlett, N. Bartolo, E. Battaner, K. Benabed, A. Benoît, A. Benoit-Lévy, S. J. Benton, J. P. Bernard, M. Bersanelli, P. Bielewicz, C. A. Bischoff, J. J. Bock, A. Bonaldi, L. Bonavera, J. R. Bond, J. Borrill, F. R. Bouchet, F. Boulanger, J. A. Brevik, M. Bucher, I. Buder, E. Bullock, C. Burigana, R. C. Butler, V. Buza, E. Calabrese, J. F. Cardoso, A. Catalano, A. Challinor, R. R. Chary, H. C. Chiang, P. R. Christensen, L. P. L. Colombo, C. Combet, J. Connors, F. Couchot, A. Coulais, B. P. Crill, A. Curto, F. Cuttaia, L. Danese, R. D. Davies, R. J. Davis, P. de Bernardis, A. De Rosa, G. de Zotti, J. Delabrouille, J. M. Delouis, F. X. Désert, C. Dickinson, J. M. Diego, H. Dole, S. Donzelli, O. Doré, M. Douspis, C. D. Dowell, L. Duband, A. Ducout, J. Dunkley, X. Dupac, C. Dvorkin, G. Efstathiou, F. Elsner, T. A. Enßlin, H. K. Eriksen, E. Falgarone, J. P. Filippini, F. Finelli, S. Fliescher, O. Forni, M. Frailis, A. A. Fraisse, E. Franceschi, A. Frejsel,

S. Galeotta, S. Galli, K. Ganga, T. Ghosh, M. Giard, E. Gjerløw, S. R. Golwala, J. González-Nuevo, K. M. Górski, S. Gratton, A. Gregorio, A. Gruppuso, J. E. Gudmundsson, M. Halpern, F. K. Hansen, D. Hanson, D. L. Harrison, M. Hasselfield, G. Helou, S. Henrot-Versillé, D. Herranz, S. R. Hildebrandt, G. C. Hilton, E. Hivon, M. Hobson, W. A. Holmes, W. Hovest, V. V. Hristov, K. M. Huffenberger, H. Hui, G. Hurier, K. D. Irwin, A. H. Jaffe, T. R. Jaffe, J. Jewell, W. C. Jones, M. Juvela, A. Karakci, K. S. Karkare, J. P. Kaufman, B. G. Keating, S. Kefeli, E. Keihänen, S. A. Kernasovskiy, R. Keskitalo, T. S. Kisner, R. Kneissl, J. Knoche, L. Knox, J. M. Kovac, N. Krachmalnicoff, M. Kunz, C. L. Kuo, H. Kurki-Suonio, G. Lagache, A. Lähteenmäki, J. M. Lamarre, A. Lasenby, M. Lattanzi, C. R. Lawrence, E. M. Leitch, R. Leonardi, F. Levrier, A. Lewis, M. Liguori, P. B. Lilje, M. Linden-Vørnle, M. López-Caniego, P. M. Lubin, M. Lueker, J. F. Macías-Pérez, B. Maffei, D. Maino, N. Mandolesi, A. Mangilli, M. Maris, P. G. Martin, E. Martínez-González, S. Masi, P. Mason, S. Matarrese, K. G. Megerian, P. R. Meinhold, A. Melchiorri, L. Mendes, A. Mennella, M. Migliaccio, S. Mitra, M. A. Miville-Deschênes, A. Moneti, L. Montier, G. Morgante, D. Mortlock, A. Moss, D. Munshi, J. A. Murphy, P. Naselsky, F. Nati, P. Natoli, C. B. Netterfield, H. T. Nguyen, H. U. Nørgaard-Nielsen, F. Noviello, D. Novikov, I. Novikov, R. O'Brient, R. W. Ogburn, A. Orlando, L. Pagano, F. Pajot, R. Paladini, D. Paoletti, B. Partridge, F. Pasian, G. Patanchon, T. J. Pearson, O. Perdereau, L. Perotto, V. Pettorino, F. Piacentini, M. Piat, D. Pietrobon, S. Plaszczynski, E. Pointecouteau, G. Polenta, N. Ponthieu, G. W. Pratt, S. Prunet, C. Pryke, J. L. Puget, J. P. Rachen, W. T. Reach, R. Rebolo, M. Reinecke, M. Remazeilles, C. Renault, A. Renzi, S. Richter, I. Ristorcelli, G. Rocha, M. Rossetti, G. Roudier, M. Rowan-Robinson, J. A. Rubiño-Martín, B. Rusholme, M. Sandri, D. Santos, M. Savelainen, G. Savini, R. Schwarz, D. Scott, M. D. Seiffert, C. D. Sheehy, L. D. Spencer, Z. K. Staniszewski, V. Stolyarov, R. Sudiwala, R. Sunyaev, D. Sutton, A. S. Suur-Uski, J. F. Sygnet, J. A. Tauber, G. P. Teply, L. Terenzi, K. L. Thompson, L. Toffolatti, J. E. Tolan, M. Tomasi, M. Tristram, M. Tucci, A. D. Turner, L. Valenziano, J. Valiviita, B. van Tent, L. Vibert, P. Vielva, A. G. Vieregg, F. Villa, L. A. Wade, B. D. Wandelt, R. Watson, A. C. Weber, I. K. Wehus, M. White, S. D. M. White, J. Willmert, C. L. Wong, K. W. Yoon, D. Yvon, A. Zacchei, A. Zonca, Bicep2/Keck, and Planck Collaborations. Joint Analysis of BICEP2/Keck Array and Planck Data. Phys. Rev. Lett., 114(10):101301, Mar 2015.

[76] Planck Collaboration, R. Adam, P. A. R. Ade, N. Aghanim, M. Arnaud, J. Aumont, C. Baccigalupi, A. J. Banday, R. B. Barreiro, J. G. Bartlett, N. Bartolo, E. Battaner, K. Benabed, A. Benoit-Lévy, J. P. Bernard, M. Bersanelli, P. Bielewicz, A. Bonaldi, L. Bonavera, J. R. Bond, J. Borrill, F. R. Bouchet, F. Boulanger, A. Bracco, M. Bucher, C. Burigana, R. C. Butler, E. Calabrese, J. F. Cardoso, A. Catalano, A. Challinor, A. Chamballu, R. R. Chary, H. C. Chiang, P. R. Christensen, D. L. Clements, S. Colombi, L. P. L. Colombo, C. Combet, F. Couchot, A. Coulais, B. P. Crill, A. Curto, F. Cuttaia, L. Danese, R. D. Davies, R. J. Davis, P. de Bernardis, G. de Zotti, J. Delabrouille, J. M. Delouis, F. X. Désert, C. Dickinson, J. M. Diego, K. Dolag, H. Dole, S. Donzelli, O. Doré, M. Douspis, A. Ducout, J. Dunkley, X. Dupac, G. Efstathiou, F. Elsner, T. A. Enßlin, H. K. Eriksen, E. Falgarone, F. Finelli, O. Forni, M. Frailis, A. A. Fraisse, E. Franceschi, A. Frejsel, S. Galeotta, S. Galli, K. Ganga, T. Ghosh, M. Giard, Y. Giraud-Héraud, E. Gjerløw, J. González-Nuevo, K. M. Górski, S. Gratton, A. Gregorio, A. Gruppuso, V. Guillet, F. K. Hansen, D. Hanson, D. L. Harrison, G. Helou, S. Henrot-Versillé, C. Hernández-Monteagudo, D. Herranz, E. Hivon,

M. Hobson, W. A. Holmes, K. M. Huffenberger, G. Hurier, A. H. Jaffe, T. R. Jaffe, J. Jewell, W. C. Jones, M. Juvela, E. Keihänen, R. Keskitalo, T. S. Kisner, R. Kneissl, J. Knoche, L. Knox, N. Krachmalnicoff, M. Kunz, H. Kurki-Suonio, G. Lagache, J. M. Lamarre, A. Lasenby, M. Lattanzi, C. R. Lawrence, J. P. Leahy, R. Leonardi, J. Lesgourgues, F. Levrier, M. Liguori, P. B. Lilje, M. Linden-Vørnle, M. López-Caniego, P. M. Lubin, J. F. Macías-Pérez, B. Maffei, D. Maino, N. Mandolesi, A. Mangilli, M. Maris, P. G. Martin, E. Martínez-González, S. Masi, S. Matarrese, P. Mazzotta, P. R. Meinhold, A. Melchiorri, L. Mendes, A. Mennella, M. Migliaccio, S. Mitra, M. A. Miville-Deschênes, A. Moneti, L. Montier, G. Morgante, D. Mortlock, A. Moss, D. Munshi, J. A. Murphy, P. Naselsky, F. Nati, P. Natoli, C. B. Netterfield, H. U. Nørgaard-Nielsen, F. Noviello, D. Novikov, I. Novikov, L. Pagano, F. Pajot, R. Paladini, D. Paoletti, B. Partridge, F. Pasian, G. Patanchon, T. J. Pearson, O. Perdereau, L. Perotto, F. Perrotta, V. Pettorino, F. Piacentini, M. Piat, E. Pierpaoli, D. Pietrobon, S. Plaszczynski, E. Pointecouteau, G. Polenta, N. Ponthieu, L. Popa, G. W. Pratt, S. Prunet, J. L. Puget, J. P. Rachen, W. T. Reach, R. Rebolo, M. Remazeilles, C. Renault, A. Renzi, S. Ricciardi, I. Ristorcelli, G. Rocha, C. Rosset, M. Rossetti, G. Roudier, B. Rouillé d'Orfeuil, J. A. Rubiño-Martín, B. Rusholme, M. Sandri, D. Santos, M. Savelainen, G. Savini, D. Scott, J. D. Soler, L. D. Spencer, V. Stolyarov, R. Stompor, R. Sudiwala, R. Sunyaev, D. Sutton, A. S. Suur-Uski, J. F. Sygnet, J. A. Tauber, L. Terenzi, L. Toffolatti, M. Tomasi, M. Tristram, M. Tucci, J. Tuovinen, L. Valenziano, J. Valiviita, B. Van Tent, L. Vibert, P. Vielva, F. Villa, L. A. Wade, B. D. Wandelt, R. Watson, I. K. Wehus, M. White, S. D. M. White, D. Yvon, A. Zacchei, and A. Zonca. Planck intermediate results. XXX. The angular power spectrum of polarized dust emission at intermediate and high Galactic latitudes. A&A, 586:A133, Feb 2016.

[77] Levon Pogosian, Amit P. S. Yadav, Yi-Fung Ng, and Tanmay Vachaspati. Primordial magnetism in the CMB: Exact treatment of Faraday rotation and WMAP7 bounds. Phys. Rev. D, 84(4):043530, Aug 2011.

[78] D. Paoletti and F. Finelli. Constraints on primordial magnetic fields from magnetically-induced perturbations: current status and future perspectives with LiteBIRD and future ground based experiments. J. Cosmology Astropart. Phys., 2019(11):028, Nov 2019.

[79] Daniel Foreman-Mackey, David W. Hogg, Dustin Lang, and Jonathan Goodman. emcee: The MCMC Hammer. PASP, 125(925):306, Mar 2013.

[80] Dylan R. Sutton, Chang Feng, and Christian L. Reichardt. Current and Future Constraints on Primordial Magnetic Fields. ApJ, 846(2):164, Sep 2017.

Appendix A

Calculations on the integrals in the two point correlation funcstions

We use a simple law for the PMF EMT spectra with the normalisation constants and spectral indices for the magnetic field power spectrum given in Eq. (4.6). Since $S(k) = 0$ and $A(k) = 0$ for $k > k_D$, two conditions need to be taken into account:

$$q < k_D\,, \qquad\qquad |\mathbf{k} - \mathbf{q}| < k_D\,. \tag{A.1}$$

Combining the two conditions k-dependence becomes $0 < k < 2k_D$, the second condition leads γ to

$$\begin{aligned} |\mathbf{k} - \mathbf{q}|^2 &< k_D^2\,, \\ k^2 + q^2 - 2kq\gamma &< k_D^2\,, \\ \gamma &> \frac{k^2 + q^2 - k_D^2}{2kq} = \frac{1 + z^2 - \tilde{k}_D^2}{2z}, \end{aligned} \tag{A.2}$$

where $\gamma = \hat{\mathbf{k}} \cdot \hat{\mathbf{q}} = x$, $z = \frac{q}{k}$, $x_0 = \frac{1+z^2-\tilde{k}_D^2}{2z}$, $\tilde{k}_D = k_D/k$. Considering $-1 < \gamma < 1$, leading to $x_0 < 1$, thus, $1 - \tilde{k}_D < z < 1 + \tilde{k}_D$, considering $0 < z < \tilde{k}_D$.

There are two situations,

If

$$\begin{aligned} \frac{k^2 + q^2 - k_D^2}{2kq} &> -1\,, \\ q &> k_D - k\,, \\ z &> \tilde{k}_D - 1\,, \\ k &> k_D - q, \end{aligned} \tag{A.3}$$

integral over γ is from x_0 to 1.

If

$$\begin{aligned} \frac{k^2+q^2-k_D^2}{2kq} &< -1\,, \\ q &< k_D - k\,, \\ z &< \tilde{k}_D - 1\,, \\ k &< k_D - q, \end{aligned} \tag{A.4}$$

integral over γ is from -1 to 1.

Considering these conditions and expressions like $|\mathbf{k}-\mathbf{q}|^n$ in Equations in Sections (4.1.4, 4.1.5,4.1.6), the double integral (over γ and over q) is split into three parts depending on the the relationship bewteen k and k_D. Particular care must be used in the radial integrals. In particular, the presence of the term $|\mathbf{k}-\mathbf{q}|^n$ in both integrands, needs a further splitting of the integral domain for odd n:

A sketch of the integration is thus the following:

For odd n:

$$\begin{aligned} &1) \quad 0 < k < \frac{k_D}{2}, \quad 2 < \tilde{k}_D, \\ &\qquad \int_{\tilde{k}_D-1}^{\tilde{k}_D} dz \int_{x_0}^{1} dx \cdots + \left(\int_{1}^{\tilde{k}_D-1} dz + \int_{0}^{1} dz\right) \int_{-1}^{1} dx \ldots \\ &\qquad \equiv \int_{\tilde{k}_D-1}^{\tilde{k}_D} dz I_a(p,k) + \left(\int_{1}^{\tilde{k}_D-1} dz + \int_{0}^{1} dz\right) I_b(p,k), \\ &2) \quad \frac{k_D}{2} < k < k_D, \quad 1 < \tilde{k}_D < 2, \\ &\qquad \left(\int_{1}^{\tilde{k}_D} dz + \int_{\tilde{k}_D-1}^{1} dz\right) \int_{x_0}^{1} dx \cdots + \int_{0}^{\tilde{k}_D-1} dz \int_{-1}^{1} dx \ldots \\ &\qquad \equiv \left(\int_{1}^{\tilde{k}_D} dz + \int_{\tilde{k}_D-1}^{1} dz\right) I_a(p,k) + \int_{0}^{\tilde{k}_D-1} dz I_b(p,k), \\ &3) \quad k_D < k < 2k_D, \quad \frac{1}{2} < \tilde{k}_D < 1, \\ &\qquad \int_{1-\tilde{k}_D}^{\tilde{k}_D} dz \int_{x_0}^{1} dx \cdots \equiv \int_{1-\tilde{k}_D}^{\tilde{k}_D} dz I_a(p,k). \end{aligned} \tag{A.5}$$

For even n:

$$\begin{aligned} &1) \quad 0 < k < k_D, \quad 1 < \tilde{k}_D, \\ &\qquad \int_{\tilde{k}_D-1}^{\tilde{k}_D} dz \int_{x_0}^{1} dx \cdots + \int_{0}^{\tilde{k}_D-1} dz \int_{-1}^{1} dx \cdots \equiv \int_{\tilde{k}_D-1}^{\tilde{k}_D} dz I_a(p,k) + \int_{0}^{\tilde{k}_D-1} dz I_b(p,k), \\ &2) \quad k_D < k < 2k_D, \quad \frac{1}{2} < \tilde{k}_D < 1, \\ &\qquad \int_{1-\tilde{k}_D}^{\tilde{k}_D} dz \int_{x_0}^{1} dx \cdots \equiv \int_{1-\tilde{k}_D}^{\tilde{k}_D} dz I_a(p,k). \end{aligned} \tag{A.6}$$

A.1 Results for integration over γ

$$
\begin{aligned}
\int_{-1}^{1} dx(1+z^2-2zx)^n &= \frac{(1+z)^{2n+2}-|1-z|^{2n+2}}{(2n+2)z}\,,\\
\int_{-1}^{1} dx(1+z^2-2zx)^n x &= -\frac{(1+z)^{2n+2}+|1-z|^{2n+2}}{(2n+2)z}+\frac{(1+z)^{2n+4}+|1-z|^{2n+4}}{(2n+2)(2n+4)z^2}\,,\\
\int_{-1}^{1} dx(1+z^2-2zx)^n x^2 &= \frac{(1+z)^{2n+2}-|1-z|^{2n+2}}{(2n+2)z}-\frac{2\Big[(1+z)^{2n+4}+|1-z|^{2n+4}\Big]}{(2n+2)(2n+4)z^2}\\
&\quad+\frac{2\Big[(1+z)^{2n+6}-|1-z|^{2n+6}\Big]}{(2n+2)(2n+4)(2n+6)z^3}\,,\\
\int_{-1}^{1} dx(1+z^2-2zx)^n x^3 &= -\frac{(1+z)^{2n+2}+|1-z|^{2n+2}}{(2n+2)z}+\frac{3\Big[(1+z)^{2n+4}-|1-z|^{2n+4}\Big]}{(2n+2)(2n+4)z^2}\\
&\quad-\frac{6\Big[(1+z)^{2n+6}+|1-z|^{2n+6}\Big]}{(2n+2)(2n+4)(2n+6)z^3}\\
&\quad+\frac{6\Big[(1+z)^{2n+8}-|1-z|^{2n+8}\Big]}{(2n+2)(2n+4)(2n+6)(2n+8)z^4}\,,\\
\int_{-1}^{1} dx(1+z^2-2zx)^n x^4 &= \frac{(1+z)^{2n+2}-|1-z|^{2n+2}}{(2n+2)z}-\frac{4\Big[(1+z)^{2n+4}+|1-z|^{2n+4}\Big]}{(2n+2)(2n+4)z^2}\\
&\quad+\frac{12\Big[(1+z)^{2n+6}-|1-z|^{2n+6}\Big]}{(2n+2)(2n+4)(2n+6)z^3}\\
&\quad-\frac{24\Big[(1+z)^{2n+8}+|1-z|^{2n+8}\Big]}{(2n+2)(2n+4)(2n+6)(2n+8)z^4}\\
&\quad+\frac{24\Big[(1+z)^{2n+10}-|1-z|^{2n+10}\Big]}{(2n+2)(2n+4)(2n+6)(2n+8)(2n+10)z^5}\,, \qquad \text{(A.7)}
\end{aligned}
$$

$$
\begin{aligned}
\int_{x_0}^{1} dx(1+z^2-2zx)^n &= \frac{(\tilde{k}_D)^{2n+2}-|1-z|^{2n+2}}{(2n+2)z}\,,\\
\int_{x_0}^{1} dx(1+z^2-2zx)^n x &= \frac{x_0(\tilde{k}_D)^{2n+2}-|1-z|^{2n+2}}{(2n+2)z}+\frac{(\tilde{k}_D)^{2n+4}-|1-z|^{2n+4}}{(2n+2)(2n+4)z^2}\,,\\
\int_{x_0}^{1} dx(1+z^2-2zx)^n x^2 &= \frac{x_0^2(\tilde{k}_D)^{2n+2}-|1-z|^{2n+2}}{(2n+2)z}+\frac{2\Big[x_0(\tilde{k}_D)^{2n+4}-|1-z|^{2n+4}\Big]}{(2n+2)(2n+4)z^2}\\
&\quad+\frac{2\Big[(\tilde{k}_D)^{2n+6}-|1-z|^{2n+6}\Big]}{(2n+2)(2n+4)(2n+6)z^3}\,,\\
\int_{x_0}^{1} dx(1+z^2-2zx)^n x^3 &= -\frac{x_0^3(\tilde{k}_D)^{2n+2}-|1-z|^{2n+2}}{(2n+2)z}+\frac{3\Big[x_0^2(\tilde{k}_D)^{2n+4}-|1-z|^{2n+4}\Big]}{(2n+2)(2n+4)z^2}\\
&\quad+\frac{6\Big[\gamma_0(\tilde{k}_D)^{2n+6}-|1-z|^{2n+6}\Big]}{(2n+2)(2n+4)(2n+6)z^3}\\
&\quad+\frac{6\Big[(\tilde{k}_D)^{2n+8}-|1-z|^{2n+8}\Big]}{(2n+2)(2n+4)(2n+6)(2n+8)z^4}\,,\\
\int_{x_0}^{1} dx(1+z^2-2zx)^n x^4 &= \frac{\gamma_0^4(\tilde{k}_D)^{2n+2}-|1-z|^{2n+2}}{(2n+2)z}+\frac{4\Big[x_0^3(\tilde{k}_D)^{2n+4}-|1-z|^{2n+4}\Big]}{(2n+2)(2n+4)z^2}\\
&\quad+\frac{12\Big[x_0^2(\tilde{k}_D)^{2n+6}-|1-z|^{2n+6}\Big]}{(2n+2)(2n+4)(2n+6)z^3}\\
&\quad+\frac{24\Big[x_0(\tilde{k}_D)^{2n+8}-|1-z|^{2n+8}\Big]}{(2n+2)(2n+4)(2n+6)(2n+8)z^4}\\
&\quad+\frac{24\Big[(\tilde{k}_D)^{2n+10}-|1-z|^{2n+10}\Big]}{(2n+2)(2n+4)(2n+6)(2n+8)(2n+10)z^5}\,,
\end{aligned}
\tag{A.8}
$$

A.2 Results for integration over z

Following the scheme (A.1) we can now perform the integration over z, since $k \ll k_D$, we will use the first split equation in (A.5) to calculate integrals. We define the following

functions to calculate the integrals over z.

1) $0 < z < 1$,

$$W_1(n,m,1,0) = \int_0^1 dz(1-z)^m z^n \equiv \frac{{}_2F_1(-m,n+1;n+2,1)}{n+1}\,,$$

2) $1 < z$,

$$W_2(n,m,\tilde{k}_D,1) \equiv \int_1^{\tilde{k}_D} dz(z-1)^m z^n = \frac{(\tilde{k}_D-1)^{m+1}{}_2F_1(-n,m+1;m+2,1-\tilde{k}_D)}{m+1}\,,$$

3) for any z,

$$W_3(n,m,\tilde{k}_D-1,0) \equiv \int_0^{\tilde{k}_D-1} dz(z+1)^m z^n = \frac{(\tilde{k}_D-1)^{n+1}{}_2F_1(-m,n+1;n+2,1-\tilde{k}_D)}{n+1}\,,$$

4) for any z,

$$W_0(n,A,B) \equiv \int_B^A dz z^n\,,$$

5) $-3 < n_S$,

$$p_S(n_S,i) \equiv (n_S)(n_S+2)\dots(n_S+2i)\,,$$

6) $-4 < n_A$,

$$p_A(n_A,i) \equiv (n_A+1)(n_A+3)\dots(n_A+2i+1)\,,$$

(A.9)

where ${}_pF_q(a_1,\dots a_p;b_1,\dots b_q;z)$ are generalized hypergeometric functions.

The Pochhammer symbol for $n \geq 0$

$$\begin{aligned}(x)_n &\equiv \frac{\Gamma(x+n)}{\Gamma(n)} \\ &= x(x+1)(x+2)...(x+n)\end{aligned} \tag{A.10}$$

The Pochhammer symbol satisfies

$$(-x)_n = (-)^n(x-n+1)_n \tag{A.11}$$

A.3 Correlators Exact Solutions

Our exact results are given for particular values of n_S and n_A. The amplitudes:

$$\begin{aligned}S_0^2 &= \frac{1}{4}\left[\frac{(2\pi)^2\lambda^{n_S+3}B_\lambda^2}{\Gamma\left(\frac{n_S+3}{2}\right)}\right]^2 = \frac{1}{4}\left[\frac{(2\pi)^{n_S+5}B_\lambda^2}{\Gamma\left(\frac{n_S+3}{2}\right)k_\lambda^{n_S+3}}\right]^2 = \frac{1}{4}\left[\frac{(2\pi)^{n_S+2}B_\lambda^2}{\Gamma\left(\frac{n_S+3}{2}\right)}\right]^2\frac{2\pi^6}{k_\lambda^{2n_S+6}}\,, \\ |A_0|^2 &= \frac{1}{4}\left[\frac{(2\pi)^2\lambda^{n_A+3}\mathcal{B}_\lambda^2}{\Gamma\left(\frac{n_A+4}{2}\right)}\right]^2 = \frac{1}{4}\left[\frac{(2\pi)^{n_A+5}\mathcal{B}_\lambda^2}{\Gamma\left(\frac{n_S+4}{2}\right)k_\lambda^{n_A+3}}\right]^2 = \frac{1}{4}\left[\frac{(2\pi)^{n_A+2}\mathcal{B}_\lambda^2}{\Gamma\left(\frac{n_A+4}{2}\right)}\right]^2\frac{2\pi^6}{k_\lambda^{2n_A+6}}\,.\end{aligned} \tag{A.12}$$

$$
\begin{aligned}
\frac{S_0^2 k^{2n_S+6}}{(2\pi)^6(\rho_{\gamma,0})^2} &= \frac{S_0^2}{(2\pi)^6(\rho_{\gamma,0})^2} k_D^{2n_S+6} \tilde{k}_D^{-(2n_S+6)} \\
&= \frac{1}{4(\rho_{\gamma,0})^2}\left[\frac{(2\pi)^{n_S+2}B_\lambda^2}{\Gamma\left(\frac{n_S+3}{2}\right)}\right]^2 (\frac{k_D}{k_\lambda})^{2n_S+6}\tilde{k}_D^{-(2n_S+6)} \\
\frac{A_0^2 k^{2n_A+6}}{(2\pi)^6(\rho_{\gamma,0})^2} &= \frac{A_0^2}{(2\pi)^6(\rho_{\gamma,0})^2} k_D^{2n_A+6} \tilde{k}_D^{-(2n_A+6)} \\
&= \frac{1}{4(\rho_{\gamma,0})^2}\left[\frac{(2\pi)^{n_A+2}\mathcal{B}_\lambda^2}{\Gamma\left(\frac{n_A+4}{2}\right)}\right]^2 (\frac{k_D}{k_\lambda})^{2n_A+6}\tilde{k}_D^{-(2n_A+6)} \\
\frac{A_0 S_0 k^{n_A+n_S+6}}{(2\pi)^6(\rho_{\gamma,0})^2} &= \frac{A_0 S_0}{(2\pi)^6(\rho_{\gamma,0})^2} k_D^{n_A+n_S+6} \tilde{k}_D^{-(n_A+n_S+6)} \\
&= \frac{1}{4(\rho_{\gamma,0})^2}\frac{(2\pi)^{n_A+n_S+4}\mathcal{B}_\lambda^2 B_\lambda^2}{\Gamma\left(\frac{n_A+4}{2}\right)\Gamma\left(\frac{n_S+3}{2}\right)} (\frac{k_D}{k_\lambda})^{n_A+n_S+6}\tilde{k}_D^{-(n_A+n_S+6)},
\end{aligned}
\tag{A.13}
$$

where $\frac{1}{4(\rho_{\gamma,0})^2} = 1.432 \times 10^{-12}$. The full exact solutions for all the correlators derived in Sections (4.1.4, 4.1.5,4.1.6) are put online[1].

[1]The solutions written by Maple and Matlab notebook is publicly available at `https://github.com/scalby/MagIntegral`